UNIVERSITY OF PAVIA
FACULTY OF ENGINEERING

CYCLE XXXII
2016-2019

Digital Signal Processing Algorithms for Multiple-Input Multiple-Output (MIMO) Based Systems

A Dissertation Presented to
The Academic Faculty

By

Farzana Kulsoom

Supervisor: Pietro Savazzi

In Partial Fulfillment
of the Requirements for the Degree
Doctor of Philosophy in the

DEPARTMENT OF ELECTRONICS, COMPUTER SCIENCE AND ELECTRICAL ENGINEERING

October 2019

Thesis Title: Digital Signal Processing Algorithms for Multiple-Input Multiple-Output (MIMO) Based Systems

Approved by:

Prof. Pietro Savazzi, Advisor

Department of Electronic and Computer Science and Electrical Engineering
University of Pavia, Italy

Prof. Magarini Maurizio

Department of Electronics, Informatics and BioEngineering
Politecnico di Milano, Italy

Prof. Laura Galluccio

Department of Electrical, Electronic and Computer Engineering
University of Catania, Italy

I would like to dedicate this thesis to my loving parents, my supportive husband and my wonderful daughters.

ACKNOWLEDGEMENTS

First and foremost, I am grateful to God for blessing me with good health, vitality, and strength to accomplish this goal which I ever dreamed of.

I extend my sincerest gratitude to my supervisor, Prof. Pietro Savazzi for his guidance and encouragement during the entire period of Ph.D. I am especially thankful to him for his thought-provoking assistance to solve the research problem. His guidance, knowledge, and expertise have improved my research skills, ability to think critically and deal with challenging situations. I am privileged and consider myself lucky to be his research student. I am also very thankful to Anna Vizziello for assisting me in my research work. The guidance and assistance which she has provided, including suggestions, reviewing my papers, making modifications, keeping my morale high, all her nice and warm words are ineffable, it improved my technical and research skills. Particularly, many thanks to Prof. Fabio Dell'Acqua for his support and help during the time of my Ph.D. I have learned many things from him including methodologies of scientific research as well as analytical and critical thinking. All these will surely benefit me throughout my career. I am grateful to Prof. Lorenzo Favalli and Paolo Gamba for reviewing my work during lab meetings and providing valuable suggestions and feedback.

Finally, my family support without which I would never be able to achieve this goal. My parents who prayed for me and encouraged me for doing this work. My caring and supportive husband who cheered me during a tough time, restored me and kept me moving when it seemed difficult. My lovely daughters Fatimah, Hanniyah, and Malaikah, my inlaws who always boosted me when I was feeling low.

ABSTRACT

Multiple Input Multiple Output (MIMO) systems are an emerging wireless communication technology that gained popularity due to its capability to enhance spectral efficiency and reliability. Although MIMO enhances system capacity and performance, it could be challenging due to the high number of antennas at both the transmitter and receiver. It has been therefore one of the popular research areas during the last decade, meeting ever-increasing demands of data rates. Nevertheless, serving multiple terminals simultaneously is challenging due to interference among them. The main goal of this research is to mitigate interference among users, gain better energy and spectral efficiency by employing different digital signal processing (DSP) based algorithms in the multi-user MIMO communication paradigm.

Moreover, we have investigated novel algorithms in order to mitigate inter-terminal interference by employing directional beams. In order to do so, it is imperative to perform channel estimation, which can be obtained by using time or frequency duplexing, although, with an increased number of antennas in large scale MIMO (massive MIMO), the problem becomes very complicated in both types of duplexing schemes. The research problem of reducing training and feedback overhead can be addressed properly if high dimensional signals are reduced to low dimensional, by taking the compressive sensing (CS) paradigm into account. A framework is proposed to reduce training and feedback overhead by considering the MIMO channel as sparse in mobile communication. Another important issue in modern MIMO communication systems is related to phase recovery. For this purpose, a reduced complexity Kalman filtering based solution is proposed to address phase recovery problem in cross-polar interference cancellation (XPIC) system, which can be viewed as MIMO 2×2 channels. Another interesting application of MIMO based systems is presented for multiple implants in the intra-body network, which utilize beamforming techniques to commu-

nicate in an energy-efficient manner. The comparison with state of the art methods is also exhibited. The research work conducted in this thesis addresses theoretical, methodological and empirical contributions to MIMO based system research problem and attempted to achieve better performance by employing different DSP based algorithms.

PREFACE

In this thesis, I have concluded my research work as a PhD student. The main focus of this work was about investigating MIMO based research problems in different fields of interest. The thesis is divided into two parts; in the first one a brief overview and background of the considered research areas are presented, including the outline of my contribution in the given domain. The second part includes my conference and journal papers related to my thesis, listed in the following:

[1] **F. Kulsoom**, A. Vizziello, H. N. Chaudhry and P. Savazzi, *"Pilot reduction techniques for sparse channel estimation in massive MIMO systems" ,* 14th Annual Conference on Wireless On-demand Network Systems and Services (WONS), Isola, 2018, pp. 111-116.

[2] **F. Kulsoom**, A. Vizziello, H. N. Chaudhry and P. Savazzi, *"Joint Sparse Channel Recovery with Quantized feedback for Multi-User Massive MIMO Systems",* Jan. 2020, IEEE Access.

[3] **F. Kulsoom**, A. Vizziello, R.Borra and P. Savazzi, *"Reduced complexity Kalman filtering for phase recovery in XPIC systems",* Physical Communication Journal, Volume 29, 2018 ,Pages 112-119.

[4] S.Banou , M.Swaminathan , G.R. Muns , D.Duong, **F.Kulsoom**, P.Savazzi , A.Vizziello and K.R.Chowdhury, *"Beamforming Galvanic Coupling Signals for IoMT Implant-to-Relay Communication",* IEEE Sensors Journal, vol. 19 2019, no. 19, pp. 8487-8501.

[5] A. Vizziello, P. Savazzi, **F. Kulsoom**, G. Magenes and P. Gamba *" A novel galvanic coupling testbed based on PC sound card for intra-body communication*

links" , BODYNETS 2019 - 14th EAI International Conference on Body Area Networks: Smart IoT and big data for intelligent health management

During my PhD, I have also contributed to the snow-wave project, devoted to determining the thickness of snow by using multi-receiver radar architecture. In the following my publications related to that work are listed, however, these publications are not included as a part of this thesis.

[1] **F. Kulsoom**, F. Dell'Acqua and M. Pasian, *"Preliminary Assessment of Factors Affecting Accuracy of Snow Layer Thickness Estimation Using BI-Static, Up-Looking Radars in an Avalanche Risk Assessment Context",* IGARSS-2018 IEEE International Geoscience and Remote Sensing Symposium, Valencia,Spain. pp. 6828-6831.

[2] **F. Kulsoom**, F. Dell'Acqua and M. Pasian, P.F. Espin-Lopez, *"Snow Layer Detection By Pattern Matching in Multipath Interference Scenario",* undergoing review IEEE Transactions on Geoscience and Remote Sensing

TABLE OF CONTENTS

LIST OF TABLES

LIST OF FIGURES

Part-1

Overview of Research Field

1

Introduction and Background of MIMO Systems

Over the last few decades wireless networks have been established as one of the promising technologies to provide communication with the ease of mobility and data reliability. The ever increasing demand for data rate and connectivity anywhere, anytime are the main motivations for an intensive use of multi-antenna communication systems. By deploying Multiple-Input Multiple-Output (MIMO) system, where multiple antennas are installed at both transmitter and receiver, it is possible to increase the capacity and efficiency of wireless networks with respect to more conventional Single-Input Single-output (SISO) based systems. MIMO systems are one of the keystones in the development and extension of data-intensive applications like and social media and video streaming on hand held devices [1], surveillance and navigation systems for target detection and tracking [2], also health based applications using

intra-body communications (IBC) [3].

However, this improvement in throughput and reliability also increases processing and hardware costs and creates new challenges. Therefore, the requirement to develop efficient digital signal processing (DSP) based algorithms and multiple access techniques is indispensable to tackle this challenge.

1.1 Background

The main challenges to enhance system performance in communication system derive from *fading*, which is due to changes in transmission medium or paths. This variation in received signal power, and *interference,* is mainly caused by the fact that many user share the same radio resources This variation in received signal power, and interference, are mainly caused by the fact that more than one user share the same radio resources simultaneously. In more details, transmitted signals can reach the receiver by more than one paths because of scatters and obstacles in the medium, this phenomenon is called multipath interference. MIMO systems may be designed to counteract this multipath radio arrangement, resulting in better performance and reliability. To increase system reliability and data rate in MIMO system, two types of data transmission arrangement are generally used. In *transmit/receive diversity* identical data is transmitted/received by multiple antennas, improving signal reliability, while keeping the same system throughput. Different types of MIMO architectures are shown in Figure 1.1. On the other hand, if independent data streams are transmitted from each antenna, MIMO systems could effectively increase the system throughput. In this case, the scheme is called space division multiple access (SDMA).

Since spectrum is a limited and expensive resource it must be utilized efficiently. *Spectral efficiency* determine the rate of information transmitted per unit bandwidth. Another important metric to keep in mind other than spectral efficiency while mea-

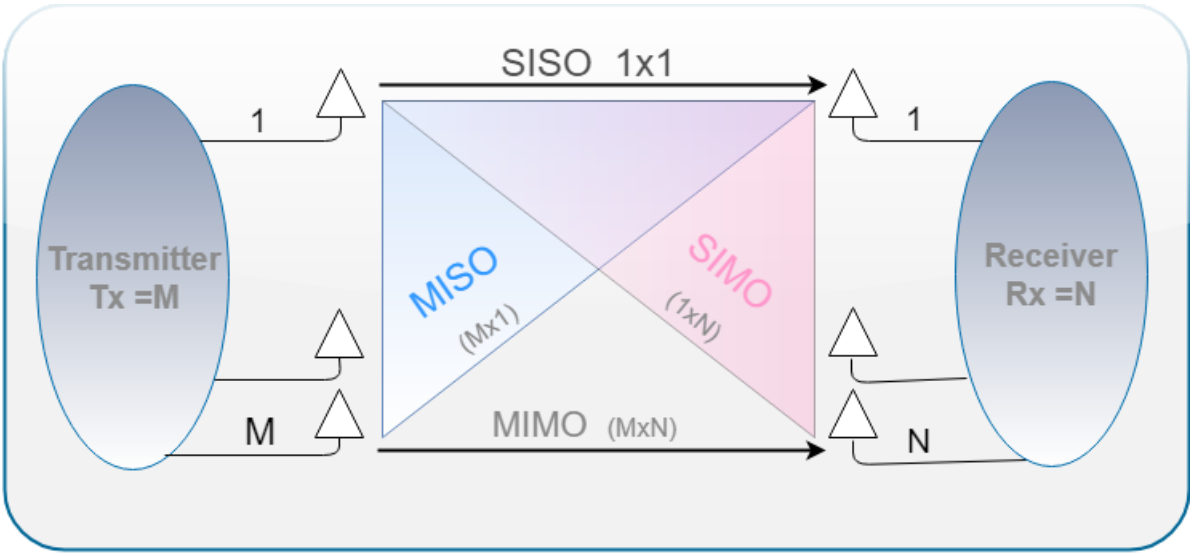

Figure 1.1: Diversities in Multi-terminal system

suring performance in wireless system is *energy efficiency (EE)*. Energy efficiency can be achieved by optimizing the transmit power. To mitigate interference across multiple users in MU-MIMO different types of *beamforming or precoding* techniques can used at transmitter:

- **Analog Beamforming:** In analog beamforming, analog phase shifters are used to steer the beam in the direction of the user [4]. Multiple beams can be formed to serve different users, but it depends on number of antennas and size of array used [5]. To serve different users simultaneously, the possible beams that can be formed must be orthogonal to each other, a limiting factor to analogue beamforming.

- **Digital beamforming/Precoding:** The digital beamforming, or linear precoding, is performed in baseband where the different user signals are superimposed with varying power and phase. Digital beamforming is more flexible and simple than analog beamforming, and its complexity does not grow with the number of antennas.

1.2 Compressed Sensing

Due to multiple nodes, MIMO systems are computationally expensive and their energy requirement is also high. The main reason is the high level of signal processing techniques needed to mitigate interference among nodes as they are sharing channel resources. Moreover, the transmitter and receiver design become complicated to manage multi-antenna transmission. These issues can be handled, if we will be able to reduce the signal measurements with the help of some signal processing techniques. Compressive sensing (CS) techniques allow to recover a signal with a much lower number of linear measurements than in the conventional case. Thus, the system can be made energy-efficient by exploring the underlying signal. Numerous examples can be given for signals which are sparse in some particular domain like time domain, frequency domain and wavelet domains. In the following, two real-world sparse signal cases are explained in order to solve some MIMO based problems discussed in this thesis.

- In massive MIMO systems most of the channel energy lies only on few dominant taps [6], therefore its channel impulse response (CIR) will be sparse. This is due to the large number of antennas at the base station (BS) with only few scatters at the BS side (compared to the number of antennas), hence only few active transmission directions per user, therefore the channel matrix tends to be sparse [7, 8].

- For humans in intra-body communications (IBC) system efficiency is directly related to the energy consumption and security related issues. In practical applications, implants may not transmit data continuously. Hence, we can easily assume that the sensed data is sparse, and with the help of the CS framework sufficient energy efficiency can be achieved, without degrading the performance.

1.3 MIMO Applications

In this thesis three MIMO applications have been considered and their related research problems have been solved with the help of signal processing techniques.

1.3.1 Massive MIMO

Massive MIMO or large scale MIMO, is a natural extension of conventional MIMO, and it groups large number of antennas at the BS to improve spectral efficiency and throughput in mobile communication. By employing large number of antennas at BS, the system capacity is increased tremendously, because of spatial multiplexing techniques and higher data rates can be achieved. Beamforming techniques help massive MIMO systems in getting better area coverage by optimizing the received signal power. Moreover, MIMO systems reduce the latency by using parallel detection [9] and by combating fading dips with the help of optimal beamforming [10]. Due to immense benefits of MIMO systems, they have become essential part of many latest standards such as WLAN (802.11n, 802.11ac etc.), WiMAX (IEEE 802.16e), LTE, LTE-Advanced, etc.

1.3.2 MIMO in Intra-Body Communication

Intra-body communication (IBC, is a data communication technique in which human body is used as a transmission medium or channel. Multiple implants are embedded into the human body in order to sense and forward their data to a skin node, called relay. These implants are interconnected and work in a MIMO fashion that allows internal physiological data to be gathered in real time and analyzed offline, thereby, transforming personalized medicine. The theoretical background can be developed for beamforming using an array of implants acting as distributed MIMO antennas. Significant performance gain can be achieved with the help of beamforming techniques

in IBC. However, there are several challenges associated with IBC , like, energy efficiency, interference among implants, synchronization issues, etc.

1.3.3 Cross-polarization interference canceller (XPIC)

In the evolution of fifth-generation (5G) mobile communication technologies, there is always an increasing demand for user traffic, resulting in higher bandwidth requirement. Cross polarization interference cancellation (XPIC) technology represents the enabler for dual-polarized transmissions over the same radio frequency (RF) channel, so that the link capacity is doubled by using two orthogonal polarization channels over the same link. In cross-polar transmission the same carrier frequency is utilised for simultaneous transmission/reception of two different data streams. Basically, one antenna is sending information on the same carrier, by exploiting different horizontal and vertical polarizations. The considered XPIC transmission is based on two independent and unsynchronized transceiver paths for backhaul links, with completely independent transmitter and receiver local oscillators (LOs).

1.4 Problem Description and Main Contribution

This research is devoted to the analysis of MIMO based system challenges and to the development of robust algorithms and techniques to handle them. We have considered different types of issues related to MIMO systems which are listed in the following.

1. **Channel Estimation:** Massive multiple input multiple output (MIMO) is one of the emerging technology in wireless communication. It employs large number of transmit antennas at the base station (BS), which makes the system more reliable and enhances the throughput compared to traditional MIMO. It also helps to mitigate inter-user interference [11]. Although, massive MIMO solves many traditional MIMO problems, it opens completely new research avenues.

The massive MIMO system can serve various users simultaneously in the same time-frequency block, due to the large deployment of antennas at the BS. Nevertheless, serving many users concurrently is challenging due to the interference among them. This interference among user can be mitigated if each user has its aligned beam. Which can be attained with proper beamforming/precoding[1]. Uplink (UL) combining or downlink (DL) transmit beamforming require good channel state information (CSI) that can be attained using time division duplex (TDD) or frequency division duplex (FDD). In TDD, both uplink (UL) and downlink (DL) operate at the same frequency bands, but in separate time slots. A channel estimate in one band can be utilized in the other, thanks to channel reciprocity. Consequently, in TDD if the channel estimate is obtained in UL, by employing the channel reciprocity, this estimate is also applicable to DL. The primary constraint of TDD is that acquisition and utilization of CSI should be performed within the coherence time [12].// Therefore, the users have to transmit their pilots simultaneously within this coherence time. Since the pilots should be orthogonal to evade interference among them, the limited number of available orthogonal sequences may result in pilot contamination [12].

Unlike TDD, in FDD the channel reciprocity is no longer applicable since UL and DL are in separate bands. Despite the advantage of channel reciprocity in TDD, FDD is important in two ways; firstly, it is considered more robust to delay-sensitive applications [13], secondly, most of the existing systems are already deployed in FDD. Therefore, it is of great significance to improve and enhance the approaches to obtain CSI in FDD systems. Since channel reciprocity can not be exploited in FDD, DL and UL channels are separately estimated. Typically, the training is done in DL by estimating CSI at the users, this CSI is sent to the BS in the uplink using a dedicated signaling link. In general,

[1]by beamforming we are always referring digital beamforming

the number of pilots required for training grows linearly with the number of transmit antennas at the BS. Since massive MIMO have a large number of BS antennas, the pilot training and feedback overhead have become the bottle-neck in FDD [14].

One of the potential solutions to resolve the training overhead problem is to explore an appropriate technique for reducing the feedback overhead.

2. **Synchronization:** We have considered the issues related to synchronization in MIMO based systems developing such techniques for XPIC system. Reduced complexity Kalman based algorithms are proposed to recover the phase of XPIC receiver in microwave radio relay links.

3. **Beamforming Galvanic Coupling Signals:**

   The state of the art for Intra-Body Communication (IBC) relies on high frequency radio (RF) signals. RF based systems are not energy efficient from the point of view of IBC. Additionally, emitted RF signals may extend to several feet around the body, creating privacy risks. We employed an alternative wireless architecture for IBNs using galvanic coupling (GC), in which low or medium frequency (100 kHz-1 MHz) and weak ($\leq$ 1 mW) electrical currents are modulated with data and directly coupled to the tissue. The privacy risks related to RF are eliminated by using GC in IBNs since the signals do not propagate outside the skin layer [15]. In GC based system currents are used in place of classical radio frequency (RF) links.

   As the first step in [16], we devise a method that allows multiple implants to communicate individual sensed data to each other through code division multiple access (CDMA) combined with compressive sensing (CS) method to lower the transmission time and save energy, as well as delegates the computational burden of despreading and decoding only to the on-body surface relays. Then,

we devise a distributed beamforming approach that allows coordinated transmissions from the implants to the relays by considering the specific tissue path chosen and tissue heating-related safety constraints. We then proceed to implement distributed beamforming on a phantom of human tissue and prove an increase in received signal strength and decrease in BER due to constructive interference of the signals of each implant.

1.5 Thesis Organization

Chapter 2 presents a general MIMO system and the theoretical underpinnings of MU-MIMO. Also, the assumptions and challenges while dealing with channel estimation in MIMO are discussed.

Chapter 3 presents a brief introduction to the essentials of compressive sensing theory in context of sparse channel estimation and most widely used sparse signal recovery algorithms.

The pilot reduction techniques for sparse channel estimation [17] in massive MIMO systems are covered in Chapter 4. We exploit compressive sensing (CS) techniques to accurately estimate the channel, while assuring overhead reduction which is proportional to the sparsity level of the channel.

Chapter 5 discusses joint Sparse Channel Recovery with Quantized feedback for Multi-User Massive MIMO Systems. In this chapter, a novel distributed CS based algorithm, named 2-step quantized partially joint orthogonal matching pursuit (Q-PJOMP), is proposed which not only reduce training overhead but also recover the channel from limited feedback for FDD based multi-user massive MIMO.

In chapter 6, a novel method to lower the transmission time and save energy is devised in [3] that allows multiple implants in intra-body network to communicate individual sensed data to each other through code division multiple access (CDMA)

combined with CS method which helps to lower computational burden and avoid interference among sensor nodes.

Chapter 7 focuses on the research work presented in [18] about galvanic coupling (GC) technology. A sound card based GC testbed is designed and implemented to achieve high flexibility and real time physiological data sets transmissions.

Chapter 8, discusses a reduced complexity Kalman filtering approach for phase recovery in XPIC systems. In this work [19], two completely independent radio frequency (RF) transceiver chains are considered for the two different polarization's, in order to have the maximum flexibility to connect different single carrier transceivers to dual-polarized antennas.

2

MIMO Wireless communication model

Wireless channels may be classified according to different characteristics of propagation environments, i.e., the media in which the radio signal can propagate in the form of electromagnetic waves. Different types of propagation channels are indoor, outdoor (urban, suburban), underwater, orbital propagation environments or any other medium in which signals propagate like, for example, the human body in intra-body communication (IBC). In order to model the channels, the propagation of waves depend on medium characteristics. For example, if the propagation medium is homogeneous, it will spread out uniformly in all directions and the signal power decreases with distance. However, if the medium includes some sort of obstacle such as buildings, trees, mountains, etc, it can undergo several attenuating effects such as reflection, refraction and scattering;

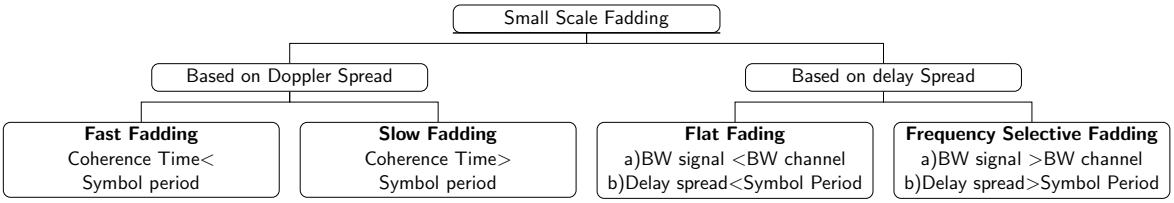

Figure 2.1: Small scale fading

- reflection, when a wave collides with any object and get reflected either completely back or at a tilted angle, the signal phase and magnitude change;
- refraction, this effect is experienced when the wave travels from one medium to another. Which affects the wave frequency and phase;
- scattering, when the wave collides with the edges of very large objects the wave amplitude and phase may change, the single wave can result in multiple waves.

The aforesaid channel effects produce multiple propagation paths, each having its own amplitude and phase. These multiple copies of the signal may interfere with each other at the receiver causing the so-called multipath fading. There are two main categories of fading, large and small scale.

- in large scale fading the averaged signal-power, or path loss, is attenuated over the long distance between the transceivers where the terrain configurations may cause shadowing zones.

- in small scale fading there are rapid fluctuations in signal amplitude or phase, because of the superposition of multipath components. Small scale fading can be further characterized by delay spread(channel response to a short pulse on multipath) and Doppler spread(frequency range over which the received doppler spectrum is non-zero). Different types of small scale fading are shown in figure 2.1.

As discussed earlier, the small scale fading is influenced by different factors including multipath components, doppler shift and the transmission bandwidth of the

signal. Based on this, the small scale fading is characterized by its doppler or delay spread as shown in figure 2.1.

2.1 Delay spread effects

Channel may be classified into frequency-selective or non-frequency selective, known also as flat, by comparing the *coherencebandwidth* B_c with the modulation one. The *Coherencebandwidth* B_c is the range of frequencies over which the channel is assumed to be approximately flat. The wireless channel can be considered as non-frequency selective or flat, if the bandwidth of the signal is less than B_c. In this case, all the received multipath components of a symbol arrive within the symbol time duration [20], so that no inter-symbol interference (ISI) occurs.

The channel will experience frequency selective fading if the signal bandwidth is greater than B_c. This type of situation occurs when the multipath components extend beyond the symbol period, causing ISI. If the received signal exhibits rapid fluctuations, its envelope can be statistically described by the Rayleigh distribution.

2.2 Doppler spread effects

The received signal power varied with the receiver or scatter motion with respect to transmitter, resulting in fast or slow fading. Channel coherence time T_c is the duration at which the channel impulse response (CIR) is assumed to be approximately constant. It is inversely proportional to the velocity and can be written as

$$T_c = \frac{c}{4vf_c} \tag{2.1}$$

where c is the light speed and f_c the carrier frequency. Usually, if the transmission packet length is less than Tc, the channel fading may be considered as flat.

2.3 MIMO Communication Models

The MIMO channel can be described by using physical (i.e., deterministic, geometry-based stochastic, and non-geometric stochastic) or analytical/mathematical models, by representing the impulse response of channel without taking into account the wave propagation model. Analytical models can be categorized as propagation-motivated and correlation-based. In the aforementioned category, the channel matrix is modeled with propagation parameters while in the latter case MIMO channel matrix is built statistically by giving the correlation between matrix entries. Examples of propagation-motived models are the maximum entropy [21], finite scatterer [22] and the virtual channel representation [23]. Analytical models need some sets of representative parameters for the targeted scenarios. Some examples of such standardized models are 3GGP [24], COST 259 [12], [11], COST 273 [25], IEEE 802.16a [26], and IEEE 802.11n [27].

For modeling the mobile communication systems considered in this thesis, we have considered spatial channel models (SCM) developed by third generation partnership project (3GPP) and international telecommunication union (ITU) for different propagation scenarios, including urban and rural ones. We consider a time-synchronized cell with K user terminals. At the BS there are M transmit antennas and N receive antennas. The analytical analysis is independent of the antenna array geometry at BS.

2.4 Detection and precoding

In MIMO systems precoding and detection schemes are applied to distinguish each node data streams with a high level of reliability. In the downlink direction, the purpose of the receiver is to recover the transmitted signal $\mathbf{x}_k \in C^{N_t \times 1}$ from kth terminal

$$\mathbf{y_k} = \mathbf{H_k x_k} + \mathbf{n_k} \tag{2.2}$$

where $\mathbf{H} \in C^{N_t \times N_r}$ is channel matrix and $\mathbf{n} \in C^{N_r \times 1}$ AWGN noise with variance σ. The BS broadcasts the signal to all users in a shared channel, producing intra-cell interference if proper multiplexing schemes are not used. To reduce the inter-user interference, the BS constructs a noisy estimate of the channel matrix which is used to compute the precoding matrix W. The forward link transmitted data from the BS can be written as

$$\mathbf{y}_k = \sqrt{\frac{\rho_{BS}}{N_t}} \mathbf{w}_k^T \mathbf{a}_k \tag{2.3}$$

where $\mathbf{w}_k$ is the precoding weight of kth terminal, $\mathbf{a}_k$ is data symbol for each terminal and ρ_{BS} is the total transmitted power of the BS. After passing through the channel, the signal $\mathbf{x}$ transmitted by BS is received at each user terminal:

$$\mathbf{x}_k = \mathbf{H}_k \mathbf{y}_k + \mathbf{n}_k \tag{2.4}$$

In equation (2.4) $\mathbf{x}_k$ is the desired signal with channel effects and noise. To maximize the SNR for each link or to remove the interference between links precoding or post-processing techniques are required. Commonly used linear beamforming techniques are following.

2.4.1 Conjugate Beamforming

Conjugate beamforming or maximum ratio can be used to maximize signal to noise ratio (SNR) for each user while ignoring the impact of interference among terminals. Furthermore, the power assigned to each user is normalized on each link so that the total transmission power BS remains the same. However, the users near to BS will have higher fraction of total power and they will build a stronger link. The drawback of conjugate beamforming is as stated earlier it ignores the effect of multi user interference.

2.4.2 Zero-Forcing beamforming

Unlike conjugate beamforming, zero-forcing (ZF), precoder takes the interuser interference into account but overlooks the impact of noise. With ZF, the multiuser interference is completely cancelled by projecting each stream on the orthogonal complement of interference between users. In the ZF precoder, the weight vector steers the null values to the position of each terminal to reduce interference, transmitting everywhere else. The drawback of ZF is that it works poorly in noise-limited scenarios because it neglects the effect of noise. Moreover, the computational complexity of ZF is higher than conjugate beamforming.

2.4.3 Minimum Mean Square Error beamforming

The minimum mean square error (MMSE) or regularized zero-forcing (RZF) attempts to maintain the strong signal gain while limiting interference among users. MMSE based precoding is better than ZF, which gives noise amplification when user channel is highly correlated. Moreover, MMSE precoder is not only robust for MU-MIMO systems where users are close enough, but it also gives good performance at high SNR value [28]. Indeed, it is considered as the best choice for linear precoding in MIMO based wireless systems [28, 29].

3

Compressive Sensing Theory

Data acquisition is one of the most significant steps in any data processing pipeline. Real-world signals are continuous-time, while processing on them is done on digital platforms. To process continuous time on digital platforms, the signals are quantized and sampled. The process of sampling should be reversible, thus implying that the signal should be reconstructable after being sampled. To enable accurate reconstruction from samples, according to the Shannon theorem, the signal should be sampled at least twice the maximum frequency of the signal. However, when the maximum frequency in real-world signal is very high, this demands a higher sampling rate to meet the Nyquist criterion, and, once sampled, the signal is simply digitally stored. Therefore, at higher sampling rates, data must be compressed to enable efficient storage. The major disadvantage in data acquisition and storage compression is discarding a lot of data which was sensed. That means that data was over-sampled while sensing it at first place after that point a large amount of sensed data is discarded to enabled

efficient storage. Another intuitive way to achieve more efficiency would be to sense the data in a compressive way and then try to recover the signal from this compressed data. Such a technique is known as *Compressed sensing* or *Compressive sensing* (CS).

3.1 Review of Sparsity and Compressibility

CS techniques are related to sensing signal in a compressed form, known as observation vector $\mathbf{y}$, in order to estimate the original signal $\mathbf{x}$. To ensure correct estimation of the signal from the observations, the data are compressed using special noise like waveform extracted from the matrix $\mathbf{A}$, known as $sensingmatrix$ or $measurementmatrix$. The relation between the sensing matrix $\mathbf{A}$ and the signals $\mathbf{x}, \mathbf{y}$ is

$$\mathbf{y} = \mathbf{A}^T\mathbf{x} \tag{3.1}$$

where $\mathbf{y}$ is a $M \times 1$ vector, $\mathbf{x}$ is a $N \times 1$ one, and $\mathbf{A}$ is a matrix with M rows and N columns, with $M \ll N$. Equation (3.1) is an undetermined system[1] which may have infinite or no exact solutions. One way out of solving such an ill-posed system is by considering the compressed sensing paradigm as explained in [30], for which the signal $\mathbf{x}$ can be correctly recovered, or with some loss, if it is sparse in some domain.

3.2 Measurement or Sensing Matrix

The design of the measurement matrix is a very important step in order to have efficient and precise sparse signal reconstruction. It is usually a combination of a random matrix $\mathbf{\Phi}$, usually defined as i.i.d. Gaussian or Bernoulli, and a transform matrix $\mathbf{\Psi}$ like the Fourier, discrete cosine or wavelet transform, so that the sensing

[1] In mathematics, linear equation system states that a system is under determined if the number of equations is less than number of unknowns

matrix can be written as $\mathbf{A} = \mathbf{\Phi\Psi}$. In the field of signal processing, transformations provide powerful tools for handling signals with distinct properties.

The choice of these matrices depends on the application under consideration, for example, in wireless communication usually Fourier transform is considered while in image processing and audio signal processing wavelet transform is applied. Usually, such sparse transformations are redundant and are also called redundant dictionaries. It is called over-complete dictionary if a number of columns are greater than the number of rows. This over-complete dictionary provides more redundant basis for more accurate and guarantees signal recovery, condition provided that it follows restricted isometric property (RIP) and mutual coherence as explained in the next subsection.

3.3 Conditions for Perfect Recovery

3.3.1 Restricted Isometric Property (RIP)

In order to guarantee sparse signal recovery, the sensing matrix must satisfies the RIP, which can be expressed as follows [31, 30],

$$(1 - \delta_{Smax})\|\mathbf{x}\|_2^2 \leq \|\mathbf{Ax}\|_2^2 \leq (1 + \delta_{Smax})\|\mathbf{x}\|_2^2 \tag{3.2}$$

In the above equation $\delta_{Smax} \in \{0, 1\}$ is the constrained parameter and $\|.\|$ represent norm. One possible solution for satisfying the RIP condition is to select the CS matrix as a random one. It is proved in [32] that if the CS matrix is chosen i.i.d Gaussian, Bernoulli or partial random Fourier matrix, the RIP condition is satisfied. Therefore, the CS-based signal recovery could be more reliable if the sensing matrix is defined as a combination of random matrix and a suitable transform [6, 30].

3.3.2 Mutual Coherence

Another important condition for getting accurate sparse signal recovery is that the random basis $\mathbf{\Phi}$ and the transform basis $\mathbf{\Psi}$ must be incoherent with respect to each other, as defined by the following relationship:

$$\mu(\mathbf{\Psi}, \mathbf{\Phi}) = \sqrt{n} \max_{1 \leq i,j \leq n} |\langle \Psi_i, \Phi_j \rangle|, \tag{3.3}$$

which defines the maximum correlation between the elements of the two matrices $\mu(\mathbf{\Psi}, \mathbf{\Phi}) \in (1, \sqrt{n})$ [30]

3.4 Reconstruction Algorithms

In this section, we focus on the reconstruction algorithms that find a sparse solution for an underdetermined system by means of l_p norm minimization, with $p = 0, 1, 2$.

$$\|(\mathbf{x}_i)_{i \in N}\|_p = \sqrt[P]{\sum_{i \in N} |\mathbf{x}_i|^p} \tag{3.4}$$

- l_0 **norm minimization:** if the signal is sparse, then the l_o norm is a natural choice to find the sparsest solution, by counting the non-zero entries of the sparse vector, under the error bound less than ϵ. This can be written as:

$$\min \|\mathbf{x}\|_o \quad \text{subject to} \quad \|\mathbf{Ax} - \mathbf{y}\|_2 \leq \epsilon \tag{3.5}$$

  Although l_o norm provides the exact solution, it is a NP hard (non-deterministic polynomial-time) problem. Therefore, it is computationally very expensive due to exhaustive search, a better option is to relax it by using the l_1 norm.

- l_1 **norm minimization:** in order to overcome the NP hard problem of l_0 norm,

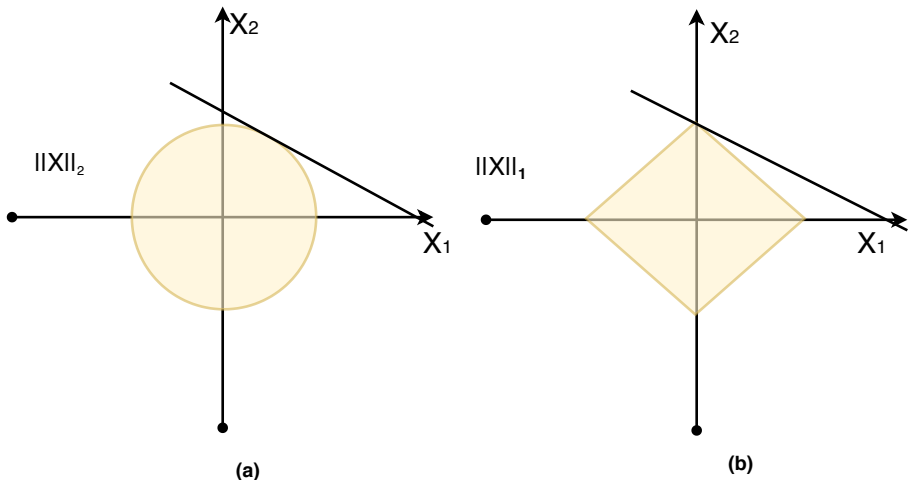

Figure 3.1: a) L_2 norm minimization b) L_1 norm minimization

the research focus is more toward relaxing l_o and look for solution using l_1 norm minimization.

$$\min\|\mathbf{x}\|_1 \quad \text{subject to} \quad \|\mathbf{Ax}-\mathbf{y}\|_2 \leq \epsilon \tag{3.6}$$

In Figure 3.1, a graphical representation of l_1 norm minimization is shown. The objective of l_1 minimization is to find a sparse vector $\mathbf{x}$ by minimizing $\|\mathbf{x}\|_1$. The l_1 minimization is a convex program and can be solved using advanced optimization techniques like basic pursuit (BP), least absolute shrinkage and selection operator (LASSO).

- l_2 **norm minimization:** in figure 3.1 a graphical view of l_2 minimization is shown. The l_2 minimization attempts to find out the sparsest solution by minimizing $\|\mathbf{x}\|_2$, which can be achieved in general by least square methods as.

$$min\|\mathbf{x}\|_2 \quad \text{subject to} \quad \|\mathbf{Ax}-\mathbf{y}\|_2 \leq \epsilon \tag{3.7}$$

In general, it is difficult to get the exact sparse vector by l_2 norm minimization even in the absence of noise. However, the algorithms based on l_2 minimization are very popular because of their less computationally complexity, and they are

called greedy algorithms, like the orthogonal matching pursuit (OMP).

The choice of the algorithm is dependent on the application under consideration. For applications requiring a high level of accuracy, as in medical ones, l_1 norm-based algorithms could be a better choice but if the focus is on getting less computational complexity, then greedy algorithms could be preferred. Besides this, there are other popular and simpler algorithms based on thresholding, for example iterative hard thresholding (IHT) and hard thresholding pursuit (HTP). In the following, we will discuss the algorithms based on convex optimization (BP), greedy (OMP) and thresholding based algorithms (IHT and HTP).

3.4.1 Convex Optimization based algorithm: Basic Pursuit (BP)

In this subsection, we will discuss the convex optimization based very popular basic pursuit (BP) algorithm. This algorithm looks for global minima among several potential solutions to $\mathbf{y} = \mathbf{Ax}$, by selecting the one whose coefficients have a minimum l_1 norm[33]. The simple form of the basic pursuit using l_1 norm does not work in presence of noise, therefore to suppress measurement noise, we have to relax the inequality given in equation (3.6) and the modified formulation will be called basic pursuit denoising (BPDN), as given below;

$$min\|\mathbf{x}\|_2 \quad \text{subject to} \quad \frac{1}{2}\|\mathbf{Ax} - \mathbf{y}\|_2 \leq \epsilon \tag{3.8}$$

Different types of solvers have been used in the literature to find a solution of such convex optimization based problem, for example, BP-simplex, interior-point algorithm also known as BP-interior, fixed-point continuation (FPC), gradient projection for sparse representation (GPSR).

3.4.2 Greedy algorithms (Orthogonal Matching Pursuit (OMP))

Orthogonal Matching Pursuit (OMP) is the most popular greedy algorithm. OMP projects the signal onto the subspace by the selecting atoms, limiting the same selection of atoms more than once. In the first step a correlation is computed with all columns of $\mathbf{A}$ by looking for the highest correlations, with $c_0 = 0$ and $\mathbf{Res}_o = \mathbf{y}$

$$C_{t+1} = C_t \cup Arg \quad \max|\mathbf{A}^T\mathbf{Res}_t| \tag{3.9}$$

where C_t subset index for prominent indices, in each step $\mathbf{x}_{t+1}$, C_{t+1} is updated. Then the orthogonal projection of $\mathbf{A}^o$ onto the span of the atoms indexed in C_{t+1}, $\mathbf{A}^o = (\mathbf{A}_c)(\mathbf{A}_c)^\dagger$ is determine. where † is pseudo inverse. Using the matrix $\mathbf{A}^o$, the difference is minimized with $\mathbf{y}$ in the least square sense.

$$\mathbf{x}_{t+1} = Arg \quad min\|\mathbf{y} - \mathbf{A^o y}\|^2 \tag{3.10}$$

Then the new residual is calculated using this $\mathbf{x}_{t+1}$

$$\mathbf{Res}_{t+1} = \mathbf{y} - \mathbf{A^o x}_{t+1} \tag{3.11}$$

The algorithm run until a stopping criteria is reached, for example until S iterations or until $\|\mathbf{Res}_t\| \geq \eta$

3.4.3 Thresholding based algorithm

Iterative Hard Thresholding (IHT) is a very effective and simple CS approach which can be realized by iterations ($y^{[0]} = 0$)

$$\mathbf{y}^{n+1} = H_{Smax}(\mathbf{y}^n + \mu\mathbf{A}^T(\mathbf{x} - \mathbf{A}\mathbf{y}^n)), \tag{3.12}$$

where $H_{Smax}(.)$ is a non-linear operator which sets all the values to zero but the S elements which have largest amplitudes. The set can be chosen based on some predefined order (i.e., ascending or descending). In the above equation μ is step size, $\mathbf{A}$ is the measurement matrix and $\mathbf{y}^{[n]}$ is the observation vector. The algorithm converges if the operator norm $\|\mathbf{A}\|_2$ is smaller than one as discussed in [34] and also if $\mathbf{A}$ meet RIP condition. Moreover, as the IHT is gradient descent based algorithm, its step size μ must be chosen optimally for better convergence [35].

Another important thresholding based algorithm is hard thresholding pursuit (HTP). This algorithm is a combination of IHT and a variant of OMP, combining advantages from both the algorithms. The HTP utilized the basic idea of choosing a good candidate for support as in the matching pursuit algorithm, then finding the vector with the support which best fits to measurements, however, it is inspired by intuition from the IHT algorithm, it seems natural to select the largest components of $(\mathbf{x}^n + \mu\mathbf{A}^*\mathbf{A}(\mathbf{x} - \mathbf{x}^n) \approx \mathbf{x}$ as described in [36].

3.5 Structured Sparsity

It has been often observed that there is some structure present in the sparsity of measured data.

- **Block sparsity**, In a particular measurement, the sparse coefficients may form a group or block of zero and non zero entries and this type of sparsity structure is named group/block sparsity, [37, 3, 38]. For example, in WSN to save energy sensors record data in on-off fashion (i.e., 'on' for 5ms then 'off' next 10 ms), resulting in a block of zero and non-zero entries.

- **Joint sparsity**, It is also possible that the sparsity structure is built across multiple measurements jointly, known as joint sparsity [7, 39, 40]. In joint sparsity, each row of N vectors tends to be zero or non-zero jointly/simultaneously.

Part-II
Included Research Paper

4

Pilot reduction techniques for MIMO systems

The downlink beamforming requires a channel estimation that usually needs long training and feedback overhead, scaling with the number of antennas at the BS. We exploit CS techniques to accurately estimate the channel, while assuring overhead reduction which is proportional to the sparsity level of the channel. The sparse virtual channel representation is obtained through a dictionary design, which is more flexible, robust and able to estimate the cell characteristics. We specifically focus on massive MIMO-Orthogonal Frequency-Division Multiplexing (OFDM) systems that show more robustness to multipath fading, and analyze several CS algorithms to select among them the best technique with the proposed dictionary design. Numerical results demonstrate that greedy solutions approach the basic pursuit bound with lower complexity and consequent shorter training period. The normalized hard threshold-

ing pursuit (NHTP) technique is the greedy algorithm with the best performance complexity trade-off. Next-generation MIMO systems allow fine beamforming with narrow beams, thanks to the large number of antennas at the BS [41] [42]. This turns out in interference avoidance among users and higher throughput compared to current architectures. On this purpose, the CS framework can be exploited to reduce the downlink training period, by sparsely representing the channel response with some dictionary or basis.

The discrete Fourier transform (DFT) matrix has been already employed to represent the channel in a sparse manner [43] [44]. However, such representation is not valid for all the antenna geometries, but only for uniform linear array (ULA) with a sufficient number of antennas and limited scattering, which reduces its real feasibility.

New dictionary based virtual channel models have been proposed to sparsely represent the channel, which are able to adjust to the cell characteristics, with no restriction to the array geometry. We exploit dictionary for sparse channel model and, once sparse channel representation is obtained, we apply compressive sensing techniques for channel estimation with a reduced dowlink training period.

We specifically focus on MIMO- OFDM systems. In order to mitigate the frequency selective fading, OFDM is used along with MIMO effectively converting it into flat fading channel. Each subcarrier is transmitted over a narrow band hence simplifying equalizer design at the receiver. We compare different compressive sensing techniques, i.e., convex optimization based approaches basic pursuit (BP) and greedy methods matching pursuit (MP). Among the greedy algorithms, we employ the well known orthogonal matching pursuit (OMP), as well as the iterative hard thresholding (IHT) and the normalized hard thresholding pursuit (NHTP) methods.

The main contributions of the work presented in this chapter are:

1. proposal of compressive sensing based framework for channel estimation in massive MIMO-OFDM FDD systems with reduced downlink training overhead;

2. implementation of different CS algorithms and selection of the optimal ones with the proposed dictionary. While [45] only demonstrates the usefulness and potential of dictionary learning based channel modeling applied to an OMP CS solution, without analyzing the problem of optimal CS algorithm selection for massive-MIMO using learned dictionary;

3. comparison of DFT basis and proposal dictionary that present varying the pilot spacing, which shows that proposed dictionary based compressed sensing is more robust and reliable even when increasing pilot spacing.

4. simulation results show that the basic pursuit gives the best performance at the cost of high complexity. Greedy solutions approach the basic pursuit bound with a lower complexity and consequent shorter training period. Specifically, the NHTP approach is the greedy algorithm with the best performance complexity trade-off.

4.1 System Model

Wireless channel involves multiple paths of varing delays and gains. The transmission at high data rates generally implies a small symbol duration, so that the received signal is affected by intersymbol interference (ISI) of successive modulation symbols, due to several paths in the propagation environment. A channel with L_t paths can therefore be represented as

$$h(t) = \sum_{k=0}^{L_t-1} \alpha_k \delta(t - \tau_k) \tag{4.1}$$

Where τ_k and α_k denote the kth channel path delay and complex gain respectively. In order to combat multipath fading, the well known multicarrier scheme OFDM may be used, by employing narrow spaced subcarriers at the transmit side. An OFDM

signal consists of N_o subcarriers, equally frequency spaced at $\Delta f = \frac{1}{T_s}$, with T_s the sampling time. An OFDM discrete time baseband signal can be expressed as

$$S_i(n) = \frac{1}{\sqrt{N_o}} \sum_{k=0}^{N_o-1} x_i(k) e^{j\frac{2\pi kn}{N_o}} \tag{4.2}$$

where $S_i(n)$ represents the nth sample of the ith OFDM symbol, and $x_i(k)$ represents the data transmitted over the kth subcarrier in the ith symbol interval, while $\frac{1}{\sqrt{N_o}}$ is a normalization factor. The kth subcarrier in the equivalent lowpass domain is described by the signal $g_k(t)$ as

$$g_k(t) = e^{j2\pi\Delta fkt} \cdot rect(\frac{t}{T_s}) \tag{4.3}$$

Despite the fact that these subcarriers overlap each other, they do not interfere since they are orthogonal. The maximum channel delay $\tau_{max} = \tau_{L_t-1}$ may cause intercarrier interference (ICI) which is usually mitigated by appending a cyclic extension of each OFDM symbol at its end, for a number of samples $G_i \geq \tau_{max}$, i.e. the guard interval. Therefore, the OFDM total symbol duration is $T_{sym} = (N_o + G_i) \cdot T_s$.

A perfect channel knowledge is a fundamental requirement for channel equalization and beamforming. The channel may be usually estimated by blind or pilot based techniques. In OFDM pilot based channel estimation, pilots are arranged in a time frequency grid over time (block based) or frequency (combo based). The receiver can directly estimate channel behavior at the frequencies where pilots are transmitted using conventional least square based technique

$$H_{i,k} = \frac{R_{i,k}}{S_{i,k}} \tag{4.4}$$

where $S_{i,k}$ is kth position of ith OFDM symbol transmitted and $R_{i,k}$ is kth position of ith OFDM symbol received. Recently, research has been focused on exploiting

communication channel sparsity, considering the fact that channel exhibit only few dominant propagation paths which may be approximated as a linear combination over a known basis or dictionary, resulting in a sparse channel impulse response (CIR). Traditionally DFT basis are used for sparse channel representation.

$$\phi = \begin{bmatrix} e^{-j2\pi k_{0,1}} & \dots & e^{-j2\pi k_{0,N_o-1}} \\ e^{-j2\pi k_{1,1}} & \dots & e^{-j2\pi k_{1,N_o-1}} \\ \vdots & \ddots & \\ e^{-j2\pi k_{N_o-1,1}} & \dots & e^{-j2\pi k_{N_o-1,N_o-1}} \end{bmatrix}$$

The use of the DFT base is compliant with the theoretical results of signals estimation in CS [30], and it has been used to represent sparse channel models. However, DFT basis may represent the channel only in a few, although orthogonal, directions. In order to better estimate the channel, more robust and refined basis may be defined.

4.1.1 Sparse Channel Estimation

In this work, we will focus on a downlink massive MIMO-OFDM system, with a number of transmit antennas equal to N, and a single antenna at the receiver. Multicarrier OFDM modulation is used in order to mitigate frequency selective fading and aid channel estimation by means of pilot subcarriers. Data frames are represented by $\mathbf{d}_j$, with $j = 1, ..., N - L$, while the number of training pilots is L.

$$\mathbf{x} = \{\mathbf{P}_1, \mathbf{d}_1, \mathbf{P}_2, \mathbf{d}_2, ..., \mathbf{P}_L, ..., \mathbf{d}_{N-L}\} \tag{4.5}$$

Pilots P are built according to a Rademacher distribution (RD)[1], comprising equally likely symbols belonging to [+1,-1] and multiplied by a phase rotation as in the

[1] in Rademacher distribution the random variate has a 50 % chance of being +1 and a 50% chance of being -1

following equation.

$$\mathbf{P} = [\mathbf{p}_1 e^{-j\pi l_1}, \mathbf{p}_2 e^{-j\pi l_2}, ..., \mathbf{p}_L e^{-j\pi l_L}] \tag{4.6}$$

where l_j are uniformly distributed random numbers belonging to the interval $[0, 1]$, while the channel delay profile can be formulated using OFDM sample time and guard interval for each dictionary point as follows

$$\boldsymbol{\tau}_h = [0, \alpha, 2\alpha, \cdots\cdots (M-1)\alpha] \tag{4.7}$$

where M is the dictionary length and $\alpha = G_i \cdot T_s - G_i \cdot T_s/M$ is the minimum channel spacing which is calculated by considering the constraint that τ_{max} must not exceed G_i. The downlink channel vector $\mathbf{h} \in \mathbb{C}^{N\times 1}$ is estimated at the mobile receiver by using pilot symbols, and this channel state information is sent back to the base station [45].

In more details, the transmitted pilot symbols may be represented by the matrix $\mathbf{A} \in \mathbb{C}^{L\times N_o}$, for DFT based sensing matrix and $\mathbf{A} \in \mathbb{C}^{L\times M}$ for dictionary based sensing matrix. Block based pilot arrangement is used as it is most suitable for multipath fading channel. For example, for N_o equals to 2048, 32 pilots are transmitted per OFDM symbol with pilot interval (PI) equal to 64, while the remaining 2016 sub carriers are used for data. After the OFDM DFT matrix multiplication, the received signal at each single user can be expressed as in the following:

$$\mathbf{y} = \mathbf{A}\mathbf{h} + \mathbf{n} \tag{4.8}$$

where the elements of $\mathbf{n} \in \mathbb{C}^{L\times 1}$ are additive white Gaussian Noise (AWGN) samples with variance $\sigma_n^2 = N_0/2$. Least square (LS) channel estimation requires a number of pilot symbols $L \geq N$, needed to compute the pseudoinverse of the pilot matrix $\mathbf{A}$. For massive MIMO the large number of Antennas N can make this unfeasible,

considering also that the estimated channel information shall be sent back to the base station.

4.1.2 Sparse Channel Representation

If $L < N$ the CS paradigm may be taken under consideration, since channel estimation may be viewed as measuring a high dimensional signal with a very limited number of measurements, assuming that the original signal, i.e. the channel estimate $\mathbf{h}$, may be sparse in a some suitable basis.

In order to construct the dictionary $\mathbf{D}$ basis, we are only considering the useful OFDM symbol duration, without G_i, and taking the channel delay profile into account

$$\mathbf{D} = \begin{bmatrix} e^{-j2\pi\cdot 1\tau_1} & e^{-j2\pi\cdot 1\tau_2} & \dots & e^{-j2\pi\cdot 1\tau_M} \\ e^{-j2\pi\cdot 2\tau_1} & e^{-j2\pi\cdot 2\tau_2} & \dots & e^{-j2\pi\cdot 2\tau_M} \\ \vdots & \dots & & \\ e^{-j2\pi\cdot N_o\tau_1} & e^{-j2\pi\cdot N_o\tau_2} & \dots & e^{-j2\pi\cdot N_o\tau_M} \end{bmatrix}$$

where $\tau(m) = 1/T_{sym} \cdot \tau_h(m)$ where $m = \{0, 1, \cdots, M-1\}$ Following this reasoning, to effectively represent channel sparsity, if the basis $\mathbf{D} \in \mathbb{C}^{M\times N_o}$ may be redefined such that $\mathcal{D} = \mathbf{D}_{L\times M}$ is a sub-matrix of $\mathbf{D}$, we can then write

$$\mathbf{y} = \mathbf{A}\mathbf{h} + \mathbf{n} = \mathcal{D} \cdot P\beta + \mathbf{n} \tag{4.9}$$

where $\beta \in \mathbb{C}^{L\times 1}$ is a representation compressed vector, and $\mathbf{y} \in \mathbb{C}^{M\times 1}$ the estimated one. The design of dictionary $\mathbf{D}$ and sensing matrix $\mathbf{A}$ is always critical when using compressed sensing. It can be seen that $\mathbf{D} \in \mathbb{C}^{N_o\times M}$, and $\mathbf{A} \in \mathbb{C}^{L\times M}$ is basically

consisting of some specific rows of $\mathbf{D}$ related to pilot locations as in [46]:

$$\mathbf{A} = \begin{bmatrix} p_1 e^{-j\pi l_1} \\ p_2 e^{-j\pi l_2} \\ \vdots \\ p_L e^{-j\pi l_L} \end{bmatrix} \otimes \begin{bmatrix} e^{-j2\pi l_1 \tau_1} & \dots & e^{-j2\pi \cdot l_1 \tau_M} \\ e^{-j2\pi l_2 \tau_1} & \dots & e^{-j2\pi \cdot l_2 \tau_M} \\ \vdots & \ddots & \\ e^{-j2\pi l_L \tau_1} & \dots & e^{-j2\pi \cdot l_L \tau_M} \end{bmatrix} \tag{4.10}$$

For comparison purposes, the sensing matrix $\mathbf{A}$ with DFT basis ϕ is computed in a similar manner from $\mathbf{D}$, i.e. only some specific rows of the basis function related to the training subcarriers are considered:

$$A_\phi = \begin{bmatrix} p_1 e^{-j\pi l_1} \\ p_2 e^{-j\pi l_2} \\ \vdots \\ p_L e^{-j\pi l_L} \end{bmatrix} \otimes \begin{bmatrix} e^{-j2\pi k_{l_1,1}} & \dots & e^{-j2\pi k_{l_1,N_o}} \\ e^{-j2\pi k_{l_2,1}} & \dots & e^{-j2\pi k_{l_2,N_o}} \\ \vdots & \ddots & \\ e^{-j2\pi k_{l_L,1}} & \dots & e^{-j2\pi k_{l_L,N_o}} \end{bmatrix} \tag{4.11}$$

The equivalent channel representation in (4.9) is sparse if $||\beta||_0 = s \ll N$. Further, if we are able to solve for compressed vector β, then the channel estimate can be obtained. Additionally, sparse signal reconstruction is based on the assumption that $\mathbf{h}$ is a s-sparse CIR, i.e. its channel energy is uniformly distributed among few dominant taps. The exact position of these dominant taps is not a priori known, and it must be estimated for effective channel sensing [46].

Sensing matrix $\mathbf{A}$ can be represented in the form of a DFT basis $\phi \in \mathbf{C}^{N_o \times N_o}$ or in the form of an over-complete dictionary $\mathbf{D} \in \mathbf{C}^{N_o \times M}$, to solve a channel estimation problem with $M > N_o$.

The main objective of any dictionary is to sparsely represent data in terms of some basic elements, called atoms, that are not required to be orthogonal and they may be seen as an over-complete spanning set. The basic philosophy of these algorithms is that a dictionary may be inferred from input data, inspired by the fact that we need

to represent each data set by using as few samples as possible.

To solve the sparse channel estimation problem, each iteration alternatively minimizes the CS error. The algorithm convergence depends on the specific sparse recovery and dictionary in the algorithms. Our work aims to obtain optimal estimate starting from an overcomplete dictionary representation. Finally, a channel estimate is built at all location merely from dictionary $\hat{\mathbf{x}} = \mathbf{D}\mathbf{y}$.

4.2 Compressive Sensing Methods

We apply different CS algorithms to the proposed dictionary based sparse channel representation, in order to select the best CS solution able to reconstruct the estimated channel from few measurements. CS methods can be categorized broadly into convex relaxation iterative algorithms [33], [30], and greedy ones [47], [48]. Other methods have been proposed as a combination of these techniques [49], [50], [51].

4.2.1 Convex relaxation iterative algorithms

The convex relaxation type exploits linear programming to solve undetermined systems. Some CS techniques are formulated as $\mathcal{L}_0$, $\mathcal{L}_1$, and $\mathcal{L}_2$ norm minimizations. In the following, we denote with $\mathbf{x}$ the estimated channel response $\hat{\mathbf{h}}$. Considering the basic pursuit algorithm, the solution of an $\mathcal{L}_1$ norm minimization can be formulated as a cost function minimization problem. BP is an iterative algorithm that initializes the first guest ($\mathbf{x} = \mathbf{x}_0 = \mathbf{A}^T\mathbf{y}$), which represents the minimal signal energy, and then computes the cost function by minimizing $\|\mathbf{y} - \mathbf{A}\mathbf{x}_0\|_2$. For the next i iterations, the measurement matrix is calculated selecting the s required measurements, and the signal coefficients are adjusted according to the minimized form. The iterations stop when enough signal coefficients are obtained, less than its sparsity level [52].

Convex relaxation methods needs only a small number of measurements to recon-

struct the signal; anyway, they exhibit a greater complexity in terms of computation and time consuming [52].

4.2.2 Greedy algorithms

Differently from the convex optimization algorithms, greedy techniques are easy to implement and able to quickly recover a sparse signal, although their solution is not optimal [52]. Such methods are in line with our objective to reduce the downlink training overhead for channel estimation. However we should also strictly take into account their performance.

Let us call $\mathbf{x}$ the large dimensional signal, that is the channel to be estimated in our case, with a high number M of samples, which is sparse in some domain. Greedy algorithms pick one position of a non-zero element of $\mathbf{x}$, which corresponds to select one column from the measurement matrix.

Some techniques have been proposed under this category: orthogonal matching pursuit (OMP) [53], compressive sampling matching pursuit (CoSaMP) [50], iterative hard thresholding (IHT) [34], and normalized hard thresholding pursuit (NHTP) [54]. Matching pursuit selects a column from the measurement matrix that maximizes the inner product of the current residuals. As a first step, the algorithm selects from the dictionary the vector corresponding to the longest projection of $\mathbf{x}$. In the second step, the signal $\mathbf{x}$ is orthogonalized by removing any element of the selected vector from $\mathbf{x}$ in order to obtain its residual with the lowest energy. Finally, such two steps are iteratively processed for the remaining part of the dictionary until the residual norm is lower than a certain threshold [52]. Orthogonal matching pursuit method is a variant of the matching pursuit algorithm by discharging both the elements of the selected vector from x, and from the basis, before doing again the process. Orthogonal matching pursuit shows better results than matching pursuit, at the cost of a higher computational complexity.

Given the high-dimensional signal $\mathbf{x}$, observed via low-dimensional measurements $\mathbf{y}$, the aim is to reconstruct the signal from the measurements. Iterative Hard Thresholding (IHT) is a simple algorithm based on thresholding [36]:

- solving the rectangular system $\mathbf{Ax} = \mathbf{y}$ is equivalent to solve the square system $\mathbf{A} \cdot \mathbf{Ax} = \mathbf{A} \cdot \mathbf{y}$;
- a sequence $\mathbf{x}^i$ can be defined as a recursion $\mathbf{x}^{i+1} = (\mathbf{I} - \mathbf{A} \cdot \mathbf{A})\mathbf{x}^i$;
- given the objective of sparse vectors, each step includes the hard thresholding operator that keeps s nonzero largest components of a vector and fixes the other ones to zero.

Compressive Sampling Matching Pursuit algorithm pursues first a suitable candidate for the support, and then finds the vector, with this support, that fits well the measurements [36].

The Hard Threshold Pursuit (HTP) algorithm is a combination of the IHT and the CoSaMP or Subspace Pursuit algorithms [36], so that it selects the s largest component of $\mathbf{x}^i + \mathbf{A} \cdot \mathbf{A}(\mathbf{x} - \mathbf{x}^i) \approx \mathbf{x}$. The HTP main feature is its high speed.

Finally, Normalized Hard Thresholding Pursuit is a variant of the HTP method.

4.3 Performance Evaluation

In this section, the performance of the proposed scheme is evaluated for different CS techniques.

4.3.1 Simulation Setup

We consider a MIMO-OFDM system, with 100 transmit antennas and one receive one. The base station uses 256 OFDM subcarriers for downlink transmission. Some subcarriers are employed for pilot sequences and others for data. The multipath

Table 4.1: Simulation parameters

Parameter	Symbol	Value
Transmit antennas	N	100
Receive antennas	R	1
OFDM subcarriers	N_o	256
OFDM guard interval	G_i	16
QAM Modulations	QAM	32
Multipath channel length	L_t	6

channel length L_{taps} is equal to 6, whose consequent interference is directly solved by the OFDM guard interval, whose length is set equal to 16. Table 5.1 summarizes the system parameters.

4.3.2 Performance Analysis

Wireless channel in the angular domain can be represented by sparse DFT basis as reported in [46],[55]. Although DFT basis are orthonormal, only a few angles or directions may be defined in it. In practical systems, signals may arrive from any arbitrary directions, so predefined patterns of dft bins do not represent a good choice [45]. On the contrary, in the proposed solution, a dictionary with more refined bins is used in order to estimate the sparse channel model. In Fig. 4.1 and 4.2, the angular representation of DFT and Dictionary basis are shown, for a $N_o \times N_o$ DFT matrix and a $N_o \times M$ dictionary one. If $N_o = M$ the dictionary is defined as complete, while when $M > N_o$ the dictionary is said over-complete, providing more redundant basis which is more flexible to estimate the channel.

The effects of different pilot spacing and sparsity levels on on system performance are analyzed. In massive MIMO, pilot training overhead is one of the main concern, since it is proportional to the number of transmit antennas, in order to acquire good CSI at the base station.

In Fig. 4.3, we analyze the effects of the OMP algorithm on BER for the following different values of the sparsity level $s = 15, 30, 45, 60, 65$. We also observe the system

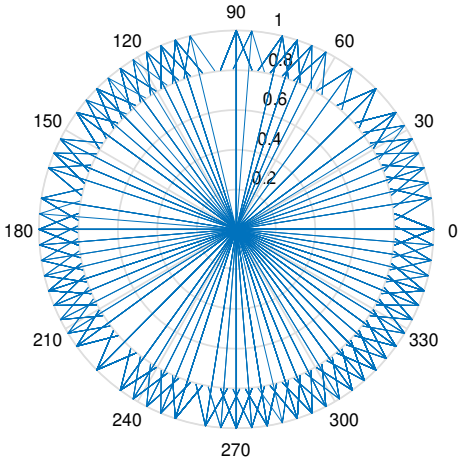

Figure 4.1: Analysis of angles of dictionary basis 16x20

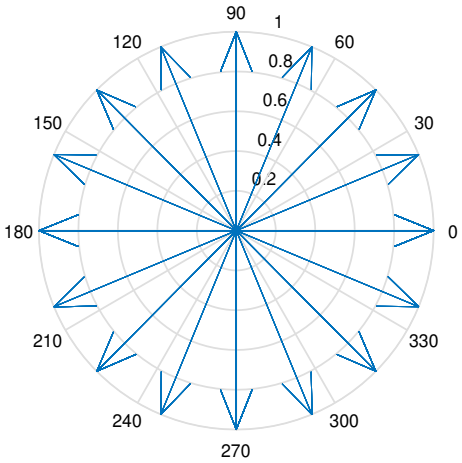

Figure 4.2: Analysis of angles of DFT basis 16x16

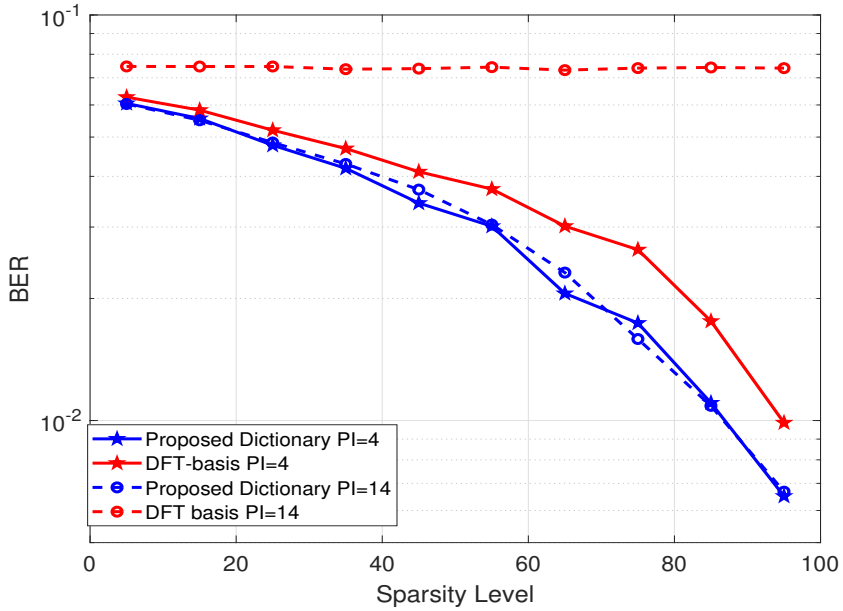

Figure 4.3: Analysis of DFT basis and proposed dictionary with different sparsity levels s and pilot spacing for OMP algorithm

performance for pilot interval (PI) values equal to 4, 14. Similar analysis can be also conducted for the other CS techniques. Fig. 4.3 shows that the proposed dictionary performs better than the DFT based one, and it is more robust to pilot spacing changes. Indeed, when $PI = 14$, the DFT basis performance behaves worse than $PI = 4$, while the dictionary based algorithm almost maintains the same performance. Further, when the sparsity level s is increasing, all the channel measurements are more accurately represented, indeed the bit error rate is decreasing.

Although there is a huge list of compressed sensing algorithms, having different benefits and drawbacks that are suitable for different systems/models, and with distinct convergence and complexity constraints, in the following figures we focus on some prominent greedy CS techniques, i. e., OMP, CoSaMP, IHT, NHTP with dictionary, compared to convex optimization based basic pursuit algorithms.

Fig. 4.4 illustrates the performance of CS algorithms with the proposed dictionary, showing that the basic pursuit method outperforms all the considered greedy algorithms in terms of BER, while the least square estimation (LSE) approach gives

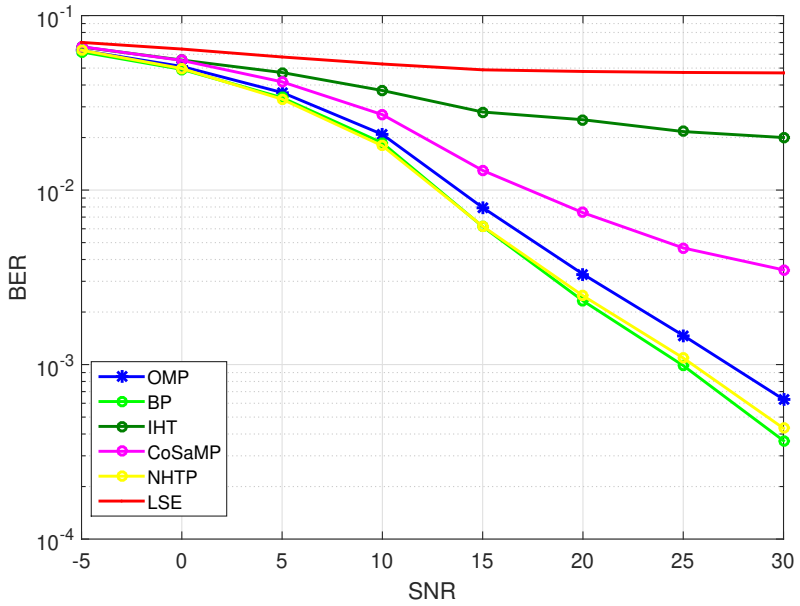

Figure 4.4: Performance of CS techniques with dictionary basis: BER vs SNR (dB) for transmit antennas $N = 100$, receive antenna $R = 1$, number of channel taps $L_t = 6$

the worst performance. However, the curve of the greedy NHTP is really close the BP one, with the advantage of high computational complexity reduction. Indeed, there is a trade-off between performance and computational complexity that we need to take into account, as shown in Sec. 4.3.3.

In Fig. 4.5 we have analyzed the effect of multipath channel for the NHTP with the proposed dictionary by varying the number of channel taps. We focus only on this algorithm since it is the best choice in terms of performance complexity trade off, as detailed in the following.

Pilot overhead reduction has been compared among different compressed sensing based algorithms including convex optimization based BP and other greedy algorithms. It has been observed that the performance curve rapidly move down with decreasing pilot interval. The previous work [55] investigated pilot overhead reduction using CS based algorithm by random pilot allocation at different subcarriers for each antenna. They have used random sending matrix with DFT basis for sparse

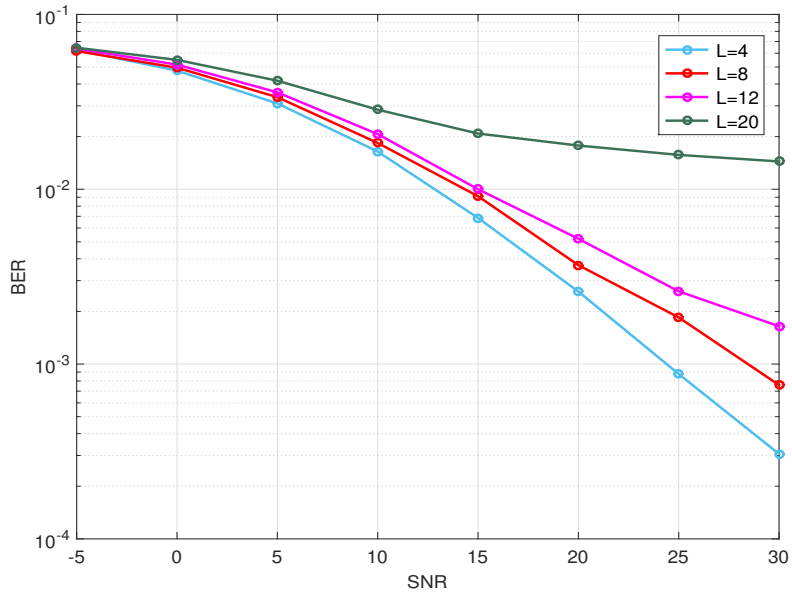

Figure 4.5: BER vs SNR (dB) for NHTP algorithm with dictionary changing the number of channel taps

Table 4.2: Computational complexity

BP	**OMP**	**CoSaMP**	**IHT**	**NHTP**
$O(n^3)$	$O(s\ m\ n)$	$O(m\ n)$	$O(m\ n)$	$O(m\ n)$

channel representation. In this section, we have assumed the same parameter setting for comparison purposes: transmit antennas = 128, number of subcarriers = 2048, SNR equal to 20 dB, 10 percent pilots overhead, and MSE equal to -25 db. As shown in figure 4.6, the proposed dictionary based algorithm exhibits better performance with pilot overhead less than 5 percent at -30 db MSE.

4.3.3 Complexity Analysis

Tables 4.2 and Fig. 4.7 refer to the computational complexity and the required simulation time, respectively.

Considering Fig. 4.4, 4.7 and Table 4.2, the greedy orthogonal matching pursuit and normalized hard thresholding pursuit show the best performance trade off in

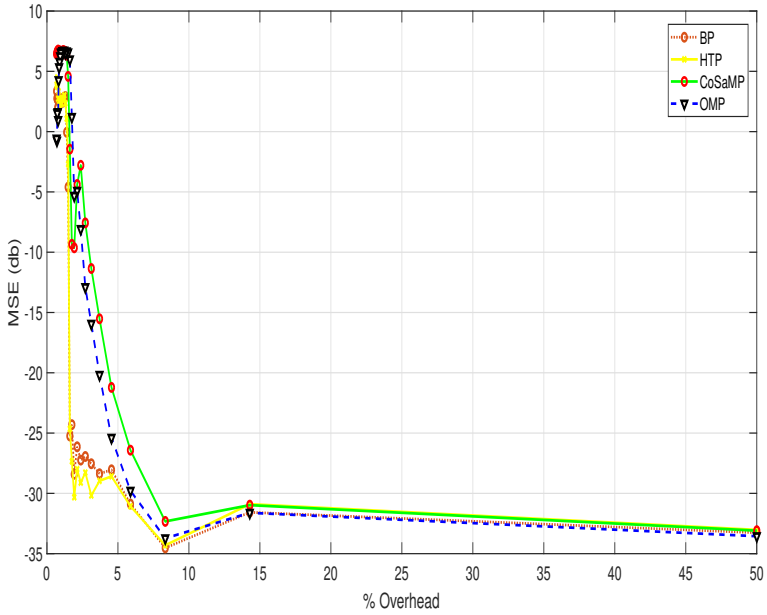

Figure 4.6: Percentage pilot overhead

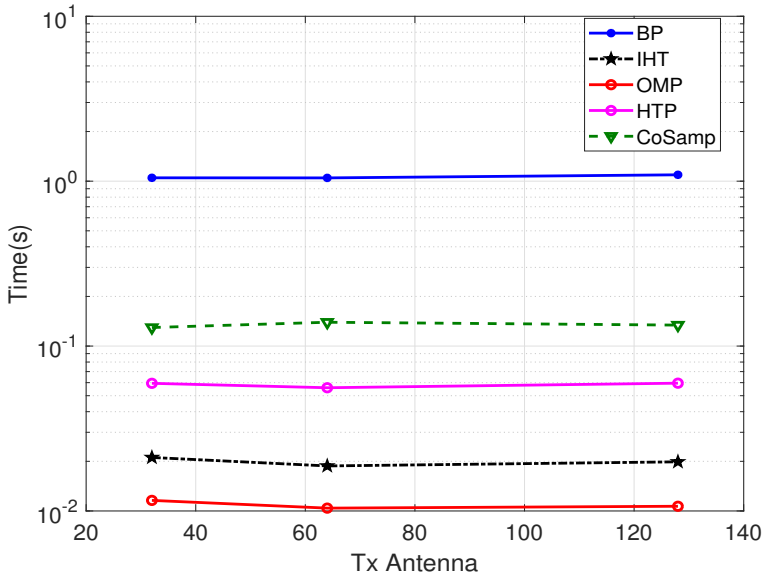

Figure 4.7: Simulation time in seconds for CS techniques with dictionary

terms of BER and computational complexity/simulation time. Note that, although OMP shows the lowest simulation time in Fig. 4.7, the NHTP BER performance in Fig. 4.4 greatly outperforms the OMP one, with a 2.5 dB gain at $10^{-}3$ BER. All the simulations are performed on an intel core i5 (7th Generation) architecture.

4.4 Conclusion

We have proposed a CS based channel estimation with a suitable dictionary for downlink beamforming in massive MIMO-OFDM FDD systems. We have exploited CS techniques to reduce training overhead, that is proportional to the sparsity level of the channel. The sparse channel representation is obtained through a proposed dictionary able to self-adapt to the cell characteristics. We have analyzed several CS algorithms in order to select among them the best technique with respect to the proposed dictionary. Numerical results demonstrate that basic pursuit shows the best performance at the cost of a higher complexity, while greedy solutions give good results with a lower complexity and hence shorter training period. Among them, the NHTP approach is the greedy algorithm with the best performance complexity trade-off.

5

Joint Channel Recovery from Quantized feedback

Accurate CSI at the transmitter is an essential prerequisite for transmit beamforming in massive MIMO systems. However, due to a large number of antennas in massive MIMO systems, the pilot training and feedback overhead become a bottleneck. To resolve this issue, the research work presents a novel framework for FDD based multi-user massive MIMO system. A 2-step quantization technique is employed at the user equipment (UE) and the CSI is recovered at the BS by applying the proposed CS based algorithms. The received compressed pilots are quantized by preserving 1 bit per dimension direction information as well as the partial amplitude information. Subsequently, this information is fed back to the BS, which employs the proposed quantized partially joint orthogonal matching pursuit (Q-PJOMP) or quantized partially joint iterative hard thresholding (Q-PJIHT) CS algorithms to recover the CSI

from a limited and quantized feedback. Indeed, an appropriate dictionary and the hidden joint channel sparsity structure among users is exploited by the CS methods, resulting in the reduction of the feedback information required for channel estimation. Simulations are performed using singular value decomposition (SVD) and minimum mean square error (MMSE) beamforming utilizing the estimated channel. The results confirm that the proposed 2-step quantization approaches the system with channel knowledge without quantization, thus overcoming the training and feedback overhead problem. Moreover, the proposed 2-step quantization outperforms 1-bit quantization, at the cost of slightly higher complexity.

5.1 Introduction

Massive MIMO is one of the emerging technology in wireless communication. It employs a large number of transmit antennas at the BS, which makes the system more reliable and enhances the throughput compared to traditional MIMO [11]. The high throughput is achieved by improving spectral efficiency, mitigating inter-user interference and employing more directional beams [11]. The massive MIMO system can serve various users simultaneously in the same time-frequency block, due to the large deployment of antennas at the BS. Nevertheless, serving many users concurrently is challenging due to the interference among them, which can be mitigated if each user has its aligned beam. This is obtained with appropriate precoding/beamforming techniques at BS. However, the accurate beamforming requires proper CSI at the transmitter. Traditionally, CSI can be obtained by using TDD or FDD schemes.

In TDD, both UL and DL operate at the same frequency bands, but in separate time slots. A channel estimate in one band can be utilized in the other, thanks to channel reciprocity. Consequently, in TDD if the channel estimate is obtained in UL, by employing the channel reciprocity, this estimate is also applicable to DL. The primary

constraint of TDD is that acquisition and utilization of CSI should be performed within the coherence time [12]. Therefore, the users have to transmit their pilots simultaneously within this coherence time. Since the pilots should be orthogonal to evade interference among them, the limited number of available orthogonal sequences may result in pilot contamination [12].

Unlike TDD, in FDD the channel reciprocity is no longer applicable since UL and DL are in separate bands. Despite the advantage of channel reciprocity in TDD, FDD is important in two ways; firstly, it is considered more robust to delay-sensitive applications [13], secondly, most of the existing systems are already deployed in FDD. Therefore, it is of great significance to improve and enhance the approaches to obtain CSI in FDD systems. Since channel reciprocity can not be exploited in FDD, DL and UL channels are separately estimated. Typically, the training is done in DL by estimating CSI at the users, this CSI is sent to the BS in the uplink using a dedicated signaling link. In general, the number of pilots required for training grows linearly with the number of transmit antennas at the BS. Since massive MIMO have a large number of BS antennas, the pilot training and feedback overhead have become the bottle-neck in FDD [14].

One of the potential solutions to resolve the training overhead problem is to explore an appropriate technique for reducing the feedback overhead. The research work in [6] and the experimental studies in [8] reveal that the increase in the number of BS antennas results in limited prominent transmission directions per user. Since there are few scatterers at the BS side as compared to the number of antennas, the channel matrix will tend to be sparse [7, 8]. In this scenario, to estimate the channel, CS paradigm can be utilized to represent a high dimensional channel vector into low dimension [17, 14, 6]. The main objective of the aforementioned research works is to reduce the number of pilot training overhead by taking advantage of the channel sparsity in general, without exploiting any structure in the measurements. Besides the

channel sparsity, it has been observed that the users are mostly located in the vicinity sharing common scatterers, for example, in offices, playgrounds, streets, apartments. Due to these scatterers, the channel is strongly correlated between the multi-antennas of each user, known as "intra-user joint channel sparsity", and among closely located distinct users, termed as "inter-user joint channel sparsity" [56].

The research works in [57, 37], exploit grouping among users to estimate the channel. The central idea is based on grouping users with common channel statistics, which will decrease the pilot overhead [57]. Subsequently, the inter-user joint sparsity can be applied within each of these groups. The research work [37] utilizes the beam-block sparsity model to reduce the pilots in DL, which are then fed back to UL in a quantized form and applied at BS to obtain CSI through CS. However, [57] does not consider intra-user or partial joint user sparsity. Other notable research works [58, 59] laid the theoretical foundations for modeling intra and inter-user joint sparsity, known as joint sparsity model (JSM). Utilizing the ideas of JSM, a class of algorithms under the paradigm of distributed compressed sensing (DCS) exploits Intra and the inter-channel correlation between users to unveil joint sparsity structure in massive MIMO systems [60, 7, 39, 61]. Although the research work in [7] [17] substantially reduced the training overhead problem, the feedback pilot bits are still considerably high. Thus, besides reducing the number of measurements, some work has also been done to lower the number of feedback bits using direct quantization [62, 63]. However, this type of direct quantization is complex and requires several bits per symbol for decoding to achieve better performance. Another extreme case of feedback reduction is 1-bit per dimension using CS algorithms as discussed in [39]. But, it hardly provides directional information and power information is lost in this manner. The power control information is very critical for CSI since it captures the effect of scatterers, multipath fading and signal strength deterioration with distance. To improve the performance, [37] presents a scheme to quantize both the amplitude and phase of

the received pilots, thus preserving both directional and power information, although in a different research problem. In [64] spatial channel estimation is performed for FDD MIMO interference alignment (IA)[1] system, and a zero-feedback bit solution is proposed. However, [64] assumes some predefined channel directions and also that UL and DL spatial channel clusters bounce on similar sub-paths.

The presented work is inspired by [37] in terms of considering both amplitude and phase information. However, we have observed that it is more efficient to quantize the complex pilot phase information with 1-bit per dimension as in [39] and acquire partial amplitude information by averaging the amplitude of compressed received pilots. Therefore, the phase information, in 1-bit compressed form as [39] along with the amplitude information, is sent back to the BS using a more simplified technique than [37]. While [37] uses eigenbeam model (EBM), our work is based on virtual channel model (VCM) that uses Fourier basis instead of eigenbasis [8]. Although VCM and EBM models are comparable in terms of system capacity and performance, VCM is inherently less complex, is more suitable for uniform linear arrays (ULAs) and can be readily extendable to frequency-selective channel [8].

In more details, this research work presents quantized feedback-based algorithms for partially joint channel estimation in massive MIMO systems, preserving both power and directional information. The pilots are transmitted from BS to each user equipment (UE), which are then quantized using a two-step quantization method and fed back to BS. The BS uses the proposed CS-based recovery algorithms to recover the channel from the quantized feedback: quantized partially joint orthogonal matching pursuit (Q-PJOMP) or quantized partially joint iterative hard thresholding (Q-PJIHT). This recovered channel information is utilized by the transmit beamforming to reduce inter-user interference. Two types of transmit beamforming, namely (i) minimum mean square error (MMSE) or regularized zero-forcing (RZF) and (ii) sin-

[1]The IA transforms the signal on the transmitters to be aligned in the signal subspace, for maximum multiplexing gain.

gular value decomposition (SVD), are employed with realistic estimated imperfect channel information, as opposed to [7, 39] that assume perfect channel knowledge to perform beamforming.

Effectively, we have focused on multiple aspects of communication and presented a complete system for CSI acquisition spanning all three main stages: (i) channel estimation, (ii) beamforming procedure, (iii) data detection.

The main contributions of the work presented in this chapter are as follows:

- this research work presents two novel distributed CS-based algorithms, Q-PJOMP and Q-PJIHT, to estimate a partially joint channel by utilizing quantized feedback in massive MIMO systems. The feedback bits are reduced without compromising significant performance gain while preserving power and directional information, as compared to [39] that considers only directional information.

- an efficient dictionary-based sparsifying matrix has been adopted, which is more effective as compared to the square DFT based sparsifying matrix especially for the frequency selective channel.

- besides improved channel estimation algorithms, two beamforming techniques, namely MMSE and SVD, are applied to reduced inter-user interference. Indeed we consider a scenario where the BS communicates simultaneously with multiple UEs through multiple beams.

- a realistic CSI estimate is acquired and utilized in the transmit beamforming procedure, as compared to the common perfect channel knowledge assumption as in [7, 39]. Furthermore, we have investigated a more realistic frequency selective channel, instead of a flat fading as in [7, 39].

Simulation results reflect that Q-PJOMP is the most suitable algorithm to estimate the partially joint channel from quantized feedback. Moreover, by applying

MMSE based transmit beamforming, the system performance is significantly improved.

5.2 System Model

5.2.1 Massive MIMO OFDM System

Consider a single-cell multi-user massive MIMO OFDM transmission over a quasi-static frequency selective fading channel. The system is composed of a BS and K users in FDD mode. The number of antennas at the BS is equal to N_t, with N_t very large, and each user is equipped with N_r antennas. The overall system model can be represented as follows:

$$\mathbf{Y}_i = \mathbf{H}_i \mathbf{X}_i + \mathbf{N}_i \tag{5.1}$$

Where $\mathbf{X}_i \in \mathbb{C}^{N_t \times T}$ is the transmitted signal in T time slots, $\mathbf{H}_i \in \mathbb{C}^{N_r \times N_t}$ is the channel matrix from the BS to the i^{th} user, $\mathbf{N}_i \in \mathbb{C}^{N_r \times T}$ is the Gaussian noise, and $\mathbf{Y}_i \in \mathbb{C}^{N_r \times T}$ is the received signal on each i^{th} user. The fading channel between each transmit antenna and i^{th} user is considered as frequency-selective and has L uncorrelated channel taps. For $N_r \times N_t$ MIMO channel, the frequency response can be written as:

$$\mathbf{H}_i(f) = \sum_{l=1}^{L} \beta_l \mathbf{a}_r(\theta_{r,l}) \mathbf{a}_t(\theta_{t,l}) e^{-j2\pi f \tau_l} \tag{5.2}$$

Where β_l is the complex amplitude for l^{th} path, τ_l is the l^{th} path delay, $\theta_{r,l}$ and $\theta_{t,l}$ are the transmitted and received path angles and $\mathbf{a}_r$, $\mathbf{a}_t$ represents array steering and response vectors of transmitted/received signal in the direction of θ_t/θ_r. To mitigate frequency selective fading the OFDM scheme is used [65, 66, 67]. An OFDM symbol duration $T_{sym} = (N_o + G) \cdot T_s$ is considered, where N_o is the number of subcarriers equally spaced in frequency at $\Delta f = \dfrac{1}{T_s}$, with the sampling time T_s and G is the guard interval in number of samples, which is set larger than the expected channel

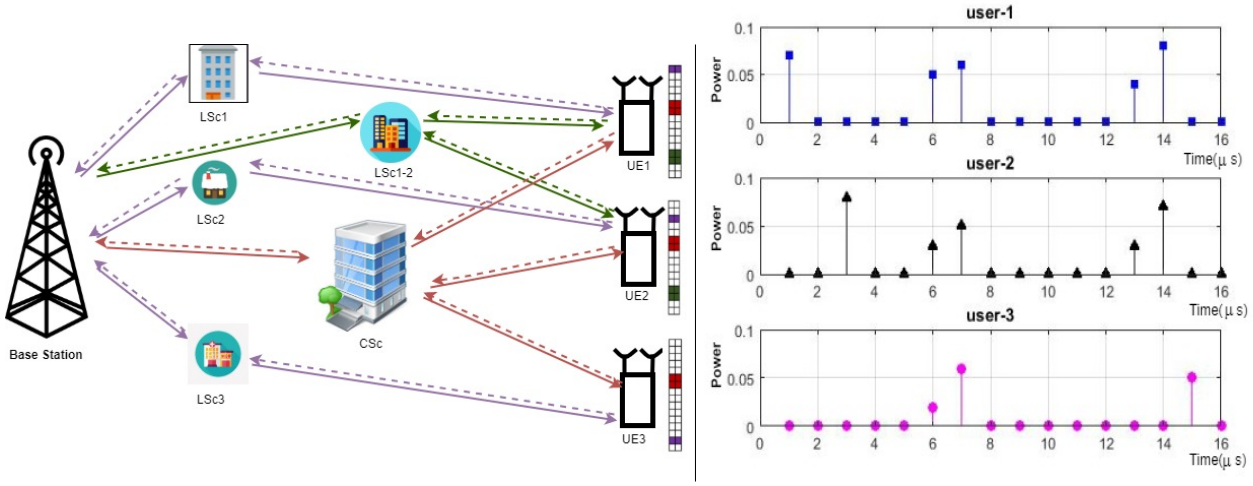

(a) Downlink (solid line) and feedback link (dotted line) for joint channel sparsity with local scatterers (LSc) and common scatterers (CSc)

(b) Hypothetically generated channel delay profile of three users to show the joint sparsity

Figure 5.1: Illustration of joint sparsity structure in MIMO channel

delay spread to further reduce the inter-symbol interference (ISI) [65].

5.2.2 Distributed Joint Channel Sparsity Model

In a cell there are some dominant scattering clusters whose position is determined from the specific attributes of the cell itself, like the presence of buildings or other propagation obstacles. These scatterers can be shared by users regardless of their position [14]. Massive MIMO experiments [8] prove that channel matrices at the user side is sparse due to the limited local scatterers at the BS [60], and maybe jointly correlated due to the shared common local scattering clusters [68]. Thus, both per-link and joint channel sparsity can be exploited through CS-based solutions to reduce training and feedback overheads. The inter-user channel sparsity can be further explained based on how scatterers are shared among users:

- The scatterers shared among all users are known as common scatterers (CSc), such as, the CSc shared among all UE in Fig. 5.1. These common scatterers will produce *joint sparsity*.

- The scatterers for a single user or shared among the subgroup of users is known as local scatterers (LSc), and will exhibit *partial joint sparsity*. For example, in Fig. 5.1 LSc1, LSc2, and LSc3 are local scatterers for UE1, UE2, and UE3 respectively, while, LSc1-2 is shared among UE1 and UE2.

The presented research work considers a ULA model for both BS and user side antennas. To represent spatio correlation channel for ULA in angular domain, the virtual channel representation can be considered. The experimental studies in [8] confirm that spatial channel can be transformed into angular domain as follows:

$$\mathbf{H}_i^a = \mathbf{F}_{R_i}^H \mathbf{H}_i \mathbf{F}_{T_i}, \qquad \mathbf{H}_i = \mathbf{F}_{R_i} \mathbf{H}_i^a \mathbf{F}_{T_i}^H \tag{5.3}$$

Where $\mathbf{F}_{R_i} \in \mathbb{C}^{N_r \times N_r}$ and $\mathbf{F}_{T_i} \in \mathbb{C}^{N_t \times N_t}$ represent the unitary matrices with Fourier basis. This transforms the channel at the BS and the user side from a spatial domain to the virtual angle domain. $\mathbf{H}_i^a \in \mathbb{C}^{N_r \times N_t}$ is the virtual channel representation and can be considered equivalent to the actual spatial channel $\mathbf{H}_i$ in Fourier domain [8]. The non-zero (c, d)-th entry of $\mathbf{H}_i^a$ indicates the spatial path from the c-th BS transmit direction to the d-th receive direction of the i^{th} user. Equation (5.3) has been used to represent the spatial channel in the angular domain with the sparsifying matrix $\mathbf{F}$ [7, 14]. Although with angular domain representation channel sparsity is guaranteed, to obtain it explicitly for each link and joint channel sparsity, the design of sparsifying matrix $\mathbf{F}$ is very critical. In [7] and [39] a sparsifying matrix $\mathbf{F}$ is considered as square DFT matrix, but in [14] and [17] it has been shown that, by introducing more redundancy in sparsifying matrix $\mathbf{F}$, an improved channel representation can be achieved, as will be detailed in Sec. 5.3.

Fig. 5.1 shows the system description with local and common scatterers in a multi-user MIMO system. Fig.5.1a explains the joint sparsity structure by displaying varying support indexes (non-zeros entries) in different colors in the channel matrix.

For example, the scatterers shared among all users are represented by the common support Θ_c indicated in red, the support of the scatterers shared only by some users is shown in green, and of the local scatterers is represented in blue. The individual support Θ_i represents the non-zeros entries of each user. Fig.5.1a shows the position of the support in this joint sparsity structure, while Fig.5.1b shows that the power values at these supports could be varying. Besides, Fig.5.1b also gives a snapshot of the channel delay profile for different users in this hypothetically generated propagation environment.

The sparsity of the massive MIMO channel may be explained as follows [7, 39, 56]:

1. **Intra-User Joint Sparsity (Individual joint Sparsity):**

   Since there are more than one receiver antennas N_r per user, the channel will exhibit intra-user joint sparsity. This effectively means that there will be channel dependency among different antennas of each user at the same time. This dependency is produced by local scatterers. Consequently, the receiver channel matrix elements will be extremely correlated and its row vectors will usually have the same sparsity support. Specifically, the matrix $\mathbf{H}_i^a$ is a row sparse and for each user i, the j^{th} row vector $\mathbf{H}_i^a(j)$ will have same support Θ_i such that $0 < |\Theta_i| \ll N_t$, i.e.,

   $$\Theta_{i1} = \Theta_{i2} = \ldots = \Theta_{iN_r} \simeq \Theta_i \tag{5.4}$$

2. **Inter-User Sparsity (Distributed Joint Sparsity):** Inter-user sparsity exploits the channel dependency among different users at the same time [56]. It refers to the scenario of a massive MIMO system where different users are close enough to share some common scatterers. Therefore, the channel matrices of different users will be highly correlated and will have common sparsity support

Θ_c:

$$\Theta_c = \bigcap_{i=1}^{K} \Theta_i \tag{5.5}$$

This common sparse support will be a subset of individual sparse support if users are sharing some common scatterers, such that $\Theta_c \subseteq \Theta_i$. However, if there are only common scatterers among users, then the individual sparsity support will be equal to the common sparsity support. There is possibility that none of the users are sharing any common scatterers, in that case, $\Theta_c = \emptyset$ [7].

5.2.3 Limited feedback based channel recovery and beamforming

The current subsection discusses the overall procedure for channel recovery from the quantized feedback pilots and utilization of that estimate for transmit beamforming as shown in Fig. 5.2.

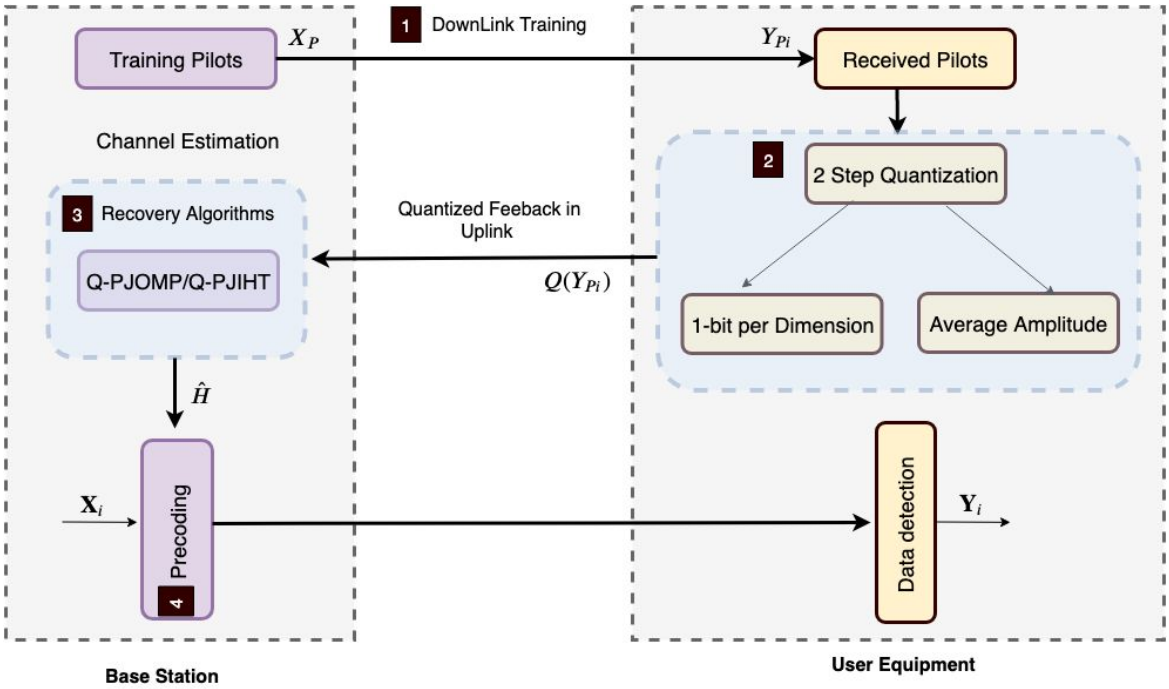

Figure 5.2: Flow chart of the overall framework of CSI acquisition and utilization.

The BS sends pilots in the DL, which are quantized at each UE and are fed back to the BS via a dedicated uplink signaling channel. The BS utilizes these quan-

tized pilots to exploit channel's hidden joint sparsity for channel estimation using distributed CS algorithms. Eventually, the recovered channel is employed for beamforming at the transmitter for more reliable data detection at the receiver. The overall system description of the quantized feedback and channel estimation is summarized in Framework and further given in Fig. 5.2. Each step of Fig. 5.2 is explained in detail as follows:

★ **Step-1 Downlink training:** To obtain CSI of the DL at the transmitter in FDD, the pilots are sent in DL. For this purpose, the BS broadcasts T common training symbols to the K users over the downlink. Therefore, the received pilots for the i^{th} user can be written as:

$$\mathbf{Y}_{pi} = \mathbf{H}_i \mathbf{X}_p + \mathbf{N}_i \tag{5.6}$$

Where $\mathbf{X}_p \in \mathbb{C}^{N_t \times T}$ is the concatenated transmitted pilots, and $\mathbf{Y}_{pi} \in \mathbb{C}^{N_r \times T}$ is the received pilots on each i^{th} user as shown in step-1 of Fig. 5.2.

★ **Step-2 Quantization:** The received pilots $\mathbf{Y}_{pi}$ are quantized at each UE to reduce the number of feedback bits, as shown in step-2 of Fig. 5.2. It is represented as $Q(\mathbf{Y}_{pi})$, however, the quantization process may also induces some error as follows:

$$\mathbf{Y}_{pi} = Q(\mathbf{Y}_{pi}) + \mathbf{\Gamma}_i = Q(\mathbf{H}_i \mathbf{X}_p + \mathbf{N}_i) + \mathbf{\Gamma}_i \tag{5.7}$$

Where Q(.) is the uniform quantization function that maps the complex pilots to bits [+1, -1] and $\mathbf{\Gamma}_i$ is the quantization error. In the presented work, pilots are quantized by preserving both direction and amplitude, as opposed to [39], where pilots are quantized to the extreme 1-bit case. The 1-bit scheme lacks power information, having only directional information, this results in poor channel estimate. Therefore, we have

considered averaged quantized amplitudes of the received pilot for each user. The averaged amplitude $\mu_i = \frac{1}{P_t}\sum_i^{P_t} |\mathbf{Y}_{pi}|$ of the received complex pilot $\mathbf{Y}_{pi}$ is determined for each user. Subsequently, these averaged amplitudes are quantized to 2 bits per user. Furthermore, the direction information is computed using 1 bit per dimension from the received pilots, given as:

$$\mathbf{Y}_{pi} = \text{sign}(\text{Re}(\mathbf{Y}_{pi})) + j\text{sign}(\text{Im}(\mathbf{Y}_{pi})) \tag{5.8}$$

The amplitude information μ is fed back along with the direction information to the BS.

★ **Step-3 Channel recovery using CS:** The quantized pilots determined in step 2 are fed back to BS in UL. At the BS, CS-based algorithms are applied to recover the channel. The BS employs the 2-bit partial amplitude information per users along with 1 bit per dimension direction information of each user to recover the channel jointly for all users. It is important to mention that, since the users are sharing the channel, partial amplitude along with direction information is sufficient to jointly estimate the partially correlated channel. For this purpose, the CS-based JOMP [7] and BIHT algorithms [39] are modified. This facilitates channel recovery using quantized feedback information. We have proposed two novel distributed CS-based algorithms for better analysis in terms of complexity and performance. The Q-PJOMP given in Algorithm 2 and Q-PJIHT is given in Algorithm 3, respectively, with further details in Sec. 5.3.

★ **Step-4 Beamforming:** During step 3 the estimate of the channel $\hat{\mathbf{H}}_i$ becomes available at the BS side, and it is employed to achieve transmit beamforming, as shown in step 4 of Fig. 5.2. The precoding matrix is constructed by applying this estimate, it overcomes the inter-user interference and decorrelates users in a highly correlated

environment. Furthermore, the precoding matrix is beneficial for data detection to decorrelate users. In particular, we have focused on MMSE or RZF, as shown in equation (5.9). It attempts to maintain strong signal gain while limiting interference among users. MMSE based precoding is more reliable than ZF, since ZF amplifies the noise in the presence of highly correlated user channel. Moreover, MMSE precoder is not only robust for MU-MIMO systems where users are located in the vicinity, but it also provides stable performance at high SNR values [28]. MMSE precoder is considered as the more suitable choice for linear precoding in MIMO based wireless systems [28, 29]. For MMSE based precoding, the received signal model in equation (5.1) is revisited by including the beamforming matrix $\mathbf{W}$ as follows:

$$\text{MMSE} \begin{cases} \mathbf{G} = \hat{\mathbf{H}}^H(\hat{\mathbf{H}}\hat{\mathbf{H}}^H + \lambda\mathbf{I})^{-1} \\ \eta = \sqrt{\frac{N_t}{Tr(\mathbf{G}\mathbf{G}^H)}} \\ \mathbf{W} = \eta\mathbf{G} \\ \mathbf{Y}_i = \mathbf{X}_i\mathbf{W}_i\mathbf{H}_i + \mathbf{N}_i \end{cases} \tag{5.9}$$

In the above equation, $\lambda = N_t\sigma^2/K$ is the regularization factor, if $\lambda = 0$, the MMSE precoder becomes equal to a ZF. The MMSE optimal precoder $\mathbf{G}$ is obtained from the estimated channel $\hat{\mathbf{H}}$ of all users. In the next step, $\mathbf{G}$ is scaled with the power scaling factor η to minimize the mean square error (MSE) under the BS transmit power constraints [69]. Primarily, η is used for power allocation at the BS to minimize the total power consumption under some given noise and interference related constraints. While λ attempts to maintain the strong signal gain with limited interference among users. Besides the MMSE precoder in equation (5.9), for comparison purpose, an SVD based beamforming is also applied, as shown in equation (5.11). It can be noted that we do not assume perfect channel knowledge. Accordingly, the estimate of realistic

channel can be decomposed using SVD, and is given as follows:

$$\hat{\mathbf{H}}_i = \hat{\mathbf{U}}_i \hat{\mathbf{\Lambda}}_i \hat{\mathbf{V}}_i^H \tag{5.10}$$

Where $\hat{\mathbf{U}}_i \in \mathbb{C}^{N_r \times N_r}$ and $\hat{\mathbf{V}}_i \in \mathbb{C}^{N_t \times N_t}$ represent the unitary matrices, such that $\hat{\mathbf{V}}_i^H \hat{\mathbf{V}}_i = \hat{\mathbf{U}}_i \hat{\mathbf{U}}_i^H = \mathbf{I}$ and $\hat{\mathbf{\Lambda}}_i \in \mathbb{C}^{N_r \times N_t}$ is a diagonal matrix. Since we have considered realistic channel $\hat{\mathbf{H}}_i$, the estimated channel characteristics will not exactly match with that of the ideal channel. Consequently, the unitary property $\mathbf{V}_i^H \hat{\mathbf{V}}_i = \mathbf{I}$ does not hold any more and this may induce interference. Nevertheless, these ramifications can be combated provided the channel estimate is robust. Based on SVD decomposition, the equation (5.1) is revised and beamforming equations can be given as:

$$\text{SVD} \begin{cases} \hat{\mathbf{X}}_i = \hat{\mathbf{V}}_i^H \mathbf{X}_i \\ \mathbf{Y}_i = \mathbf{H}_i \mathbf{X}_i + \mathbf{N}_i = (\mathbf{U}_i \mathbf{\Lambda}_i \mathbf{V}_i^H) \mathbf{X}_i + \mathbf{N}_i, \qquad \forall_i \in K \\ \hat{\mathbf{U}}_i^H \mathbf{Y}_i = \hat{\mathbf{U}}_i^H (\mathbf{U}_i \mathbf{\Lambda}_i \mathbf{V}_i^H) \hat{\mathbf{V}}_i \hat{\mathbf{X}}_i + \hat{\mathbf{U}}_i^H \mathbf{N}_i, \qquad \forall_i \in K \\ \hat{\mathbf{Y}}_i = \mathbf{\Lambda}_i \hat{\mathbf{X}}_i + \hat{\mathbf{N}}_i \end{cases} \tag{5.11}$$

Where $\hat{\mathbf{X}}_i$ is the precoded signal at the transmitter, $\hat{\mathbf{N}}_i = \hat{\mathbf{U}}_i^H \mathbf{N}_i$ is the noise term, and $\hat{\mathbf{Y}}_i = \hat{\mathbf{U}}_i^H \mathbf{Y}_i$ is the decoder for the transmit beamformer at the receiver side.

5.3 Compressive Channel estimation with limited feedback

The current section focuses on channel estimation at BS using CS algorithms. It is performed by employing the quantized pilots received on BS from UE, as indicated in step-3 of Fig. 5.2. We here discuss compressed sensing algorithms and dictionary design in more detail.

Algorithm 1 Joint channel recovery framework from quantized feedback

Step-1: A common training pilot vector $\mathbf{X}_p$ is transmitted from BS to all the users.
Step-2: Each user's received pilots are quantized using two steps:

(a) The averaged amplitude μ_i of the received pilot vector $\mathbf{Y}_{pi}$ is calculated for each user. Then these averaged amplitudes are quantized to 2 bits per user;

(b) The sign information is achieved with 1 bit per dimension from the received pilots:
$S(\mathbf{Y}_{pi}) = S(\mathbf{H}_i\mathbf{X}_p)$ such that
$S(\mathbf{Y}_{pi}) = \text{sign}(\text{Re}(\mathbf{Y}_{pi})) + j\text{sign}(\text{Im}(\mathbf{Y}_{pi}))$.

Step-3: Each user feedbacks the obtained quantized and reduced $\mathbf{Y_{pi}}$ to BS.
Step-4: The channel is jointly recovered for all users from the quantized feedback pilots $\mathbf{Y}_{pi}$ using distributed CS at BS.

5.3.1 Comparison of dictionary and DFT basis for measurement matrix design

A channel that exhibits only a few dominant propagation paths may be considered sparse and is approximated as a linear combination over a known basis or dictionary, resulting in a sparse channel response [65]. Conventionally, DFT basis ϕ have been utilized for sparse channel representation [65, 37, 70, 7, 39] as shown below.

$$\phi = \frac{\mathbf{1}}{\sqrt{\mathbf{N_t}}} \begin{bmatrix} e^{-j2\pi k_{1,1}} & \dots & e^{-j2\pi k_{1,N_t}} \\ e^{-j2\pi k_{2,1}} & \dots & e^{-j2\pi k_{2,N_t}} \\ \vdots & \ddots & \\ e^{-j2\pi k_{N_t,1}} & \dots & e^{-j2\pi k_{N_t,N_t}} \end{bmatrix}$$

The usage of the DFT basis is compliant with the theoretical results of signal estimation in CS [30], therefore, the DFT basis are employed in sparse channel representation. Considering normalized DFT basis ϕ as a sparsifying matrix, the sparse channel response can be written as, $\hat{\mathbf{H}}_i = \phi\mathbf{B}_{si}$, where $\mathbf{B}_{si} \in \mathbb{C}^{N_t \times N_r}$ is the sparse matrix. As described earlier in equation (5.3), such modeling is applied to represent

spatial channel response into the angular domain, also known as the virtual channel model. Though, the DFT basis represents the channel only in a few directions. In a real-world scenario, the actual signal can emanate from arbitrary directions, which may differ from the one represented in the DFT matrix. This results in leakage effect and poor channel estimate. In case the channel is highly correlated or exhibits multipath, the leakage effect worsens even further [14].

To estimate the channel accurately, a robust and effective basis is an essential prerequisite. To construct an improved and substantial basis or dictionary, we extended the squared DFT matrix by proposing added redundancy and considering the channel delay profile as in [17]. The objective is to build a more flexible and enhanced representation of the channel. In the dictionary formulation, the channel delay profile τ_{ch} can be represented using OFDM sample time T_s and guard interval G, for each dictionary point as follows:

$$\tau_{ch} = [0, \alpha, 2\alpha, \cdots\cdots (M-1)\alpha] \tag{5.12}$$

Where M is the length of dictionary column, α is step size in the range of 0 to M and is given as $\alpha = [G \cdot T_s - (G \cdot T_s/M)]$. To avoid inter-symbol interference (ISI), the step size α is constrained with $\tau_{\max}$ not exceeding G, i.e., $(\tau_{\max} < G)$[65]. To formulate the dictionary basis $\mathbf{D}$ for the channel response, the OFDM symbol duration T_{sym} and the delay profile can be utilized as follows:

$$\mathbf{D} = \begin{bmatrix} e^{-j2\pi k_1 \tau_1} & e^{-j2\pi k_1 \tau_2} & \cdots & e^{-j2\pi k_1 \tau_M} \\ e^{-j2\pi k_2 \tau_1} & e^{-j2\pi k_2 \tau_2} & \cdots & e^{-j2\pi k_2 \tau_M} \\ \vdots & \cdots & & \\ e^{-j2\pi k_{N_t} \tau_1} & e^{-j2\pi k_{N_t} \tau_2} & \cdots & e^{-j2\pi k_{N_t} \tau_M} \end{bmatrix}$$

Where $\tau(m) = \tau_{\text{ch}}(m)/T_{\text{sym}}$ is the channel delay normalized by OFDM symbol duration T_{sym}, having $m = \{1, 2, \cdots M\}$. To effectively estimate a channel with multiple

paths, the guard interval and channel delay profiles must be taken into account. Comparable to DFT basis, the channel response can be sparsely represented in dictionary $\mathbf{D}$ based sparsifying matrix, $\hat{\mathbf{H}}_i = \mathbf{D}\mathbf{B}_{si}$. The $\mathbf{B}_{si} \in \mathbb{C}^{M \times N_r}$ is the sparse matrix such that ($\|\mathbf{B}_{si}\|_0 \ll N_t$). Equation (5.1) can be rewritten as:

$$\mathbf{Y}_{pi} = \mathbf{A}\hat{\mathbf{H}}_i + \mathbf{N}_i = \mathbf{A}\mathbf{D}\mathbf{B}_{si} + \mathbf{N}_i \tag{5.13}$$

Where $\mathbf{A}$ is the measurement matrix, it can be constructed by utilizing the transmitted pilots $\mathbf{X}_p$ and sub DFT basis or sub-dictionary. In further detail, a sub-dictionary $\mathcal{D} \in \mathbb{C}^{P_t \times N_t}$ can be derived from dictionary $\mathbf{D} \in \mathbb{C}^{N_t \times M}$, subsequently, the measurement matrix $\mathbf{A}$ can be expressed as:

$$\mathbf{A}_{\mathcal{D}} = \mathbf{X}_p^H \otimes \mathcal{D} \tag{5.14}$$

The basis $\mathcal{D}$ comprises of specially selected rows of $\mathbf{D}$ associated with the pilot locations [65], as shown in equation (5.15). The transmitted pilots $\mathbf{X}_p$ are built according to Rademacher distribution (RD) consisting of equally likely symbols taken from $[+1, -1]$. Subsequently, they are multiplied by a phase rotation and can be formulated as $\mathbf{X}_{P_n} = [P_1 e^{-j\pi l_1} P_2 e^{-j\pi l_2} \dots P_t e^{-j\pi l_{P_t}}]$, where P_t represents the total number of transmitted pilots for the n^{th} transmit antenna.

$$\mathbf{A}_{\mathcal{D}} = \mathbf{X}_p^H \otimes \begin{bmatrix} e^{-j2\pi k_1 \tau_1} \dots e^{-j2\pi \cdot k_1 \tau_{N_t}} \\ e^{-j2\pi k_2 \tau_1} \dots e^{-j2\pi \cdot k_2 \tau_{N_t}} \\ \vdots \\ e^{-j2\pi k_{P_t} \tau_1} \dots e^{-j2\pi \cdot k_{P_t} \tau_{N_t}} \end{bmatrix} \tag{5.15}$$

Where $\mathbf{A}_{\mathcal{D}} \in \mathbb{C}^{P_t \times N_t}$ represents the measurement matrix constructed from known pilots and dictionary. For comparison, the measurement matrix $\mathbf{A}$ is computed using two equivalent approaches; firstly, starting from $\mathbf{D}$ as already discussed in equation

(5.15), and secondly, through DFT basis ϕ, that is shown in equation (5.16).

$$\mathbf{A}_{\phi} = \mathbf{X}_{p}^{H} \otimes \begin{bmatrix} e^{-j2\pi k_{1,1}} & \dots & e^{-j2\pi k_{1,N_t}} \\ e^{-j2\pi k_{2,1}} & \dots & e^{-j2\pi k_{2,N_t}} \\ \vdots & \ddots & \\ e^{-j2\pi k_{P_t,1}} & \dots & e^{-j2\pi k_{P_t,N_t}} \end{bmatrix} \tag{5.16}$$

$\mathbf{A}_{\phi} \in \mathbb{C}^{P_t \times N_t}$ is calculated from DFT sub matrix. It is noteworthy that the construction of the measurement matrix $\mathbf{A}_{\mathcal{D}}$ is different from $\mathbf{A}_{\phi}$ used by [7, 39].

In the case $\mathbf{D}$, $\mathbf{A}$ and $\mathbf{Y}_{pi}$ are known in equation (5.13), the solution of $\|\mathbf{B}_{si}\|_0$ will yield the channel estimate. Solving $\|\mathbf{B}_{si}\|_0$ will provide an exact solution, however, it is NP-hard problem. The severity of predicament can be reduced if we relax l_0 norm to some higher norm such that l_2 norm i.e., min $\|\mathbf{B}_{si}\|_{1,2}$. Where, the $\|\mathbf{B}_{si}\|_{1,2}$ is the summation of l_2 norm of each row in $\mathbf{B}_{si}$ [14]. The aforementioned optimization problem can be formulated for joint channel estimation at BS [71], as shown in equation (5.17)

$$\min_{\{\mathbf{B}_{si} \forall_i\}} \sum_{i=1}^{K} \|\mathbf{Y}_{pi} - \mathbf{ADB}_{si}\|_2 \leq \epsilon \tag{5.17}$$

The above mentioned minimization problem is very challenging, due to both individual and joint sparsity among different users. By solving the above optimization problem, instead of obtaining a channel estimate with training overhead proportional to N_t, it is possible to obtain a good channel estimate which is proportional to the sparsity level s of the sparse channel with $s \ll N_t$.

5.3.2 Constraints for Stable Recovery

Several constraints and properties have been discussed in the literature for the stable sparse signal reconstruction of the measurement matrix $\mathbf{A}$. For example, the accuracy of recovery parameters can be determined in case $\mathbf{A}$ satisfies the null space property

(NSP), restricted isometry property (RIP) or mutual coherence, however, NSP or RIP is difficult to measure. For guaranteed sparse signal recovery, it is adequate to only satisfy the mutual coherence property for the measurement matrix $\mathbf{A}$ [72][65].

Theorem 1 : In mutual coherence, the maximum absolute and normalized inner product between the columns of measurement matrix $\mathbf{A}$ is analyzed. It determines the correlation among the columns of the measurement matrix and can be formulated as in [65]:

$$\begin{aligned}\mu\{\mathbf{A}\} &= \max_{1\leq i\leq j\leq N_t, i\neq j} \frac{|\mathbf{A}_i, \mathbf{A}_j|}{\|\mathbf{A}_i\|_2 \|\mathbf{A}_j\|_2} \\ &= \max_{1\leq i\leq j\leq N_t, i\neq j} \frac{|\mathbf{A}_i^H \mathbf{A}_j|}{\|\mathbf{A}_i\|_2 \|\mathbf{A}_j\|_2}\end{aligned} \tag{5.18}$$

The mutual coherence of $\mathbf{A}$ at the pilot locations can be written as:

$$\mu\{A\} = \max_{1\leq i\leq j\leq N_t, i\neq j} \frac{\sum_{l=1}^{P_t} (\mathbf{X}_p(k_l) e^{-j2\pi k_l \tau_i/N_t})(\mathbf{X}_p(k_l) e^{j2\pi k_l \tau_j/N_t})}{\sum_{l=1}^{P_t} |\mathbf{X}_{pl}|^2} \tag{5.19}$$

$$= \max_{1\leq i\leq j\leq N_t, i\neq j} \frac{\sum_{l=1}^{P_t} |\mathbf{X}_p(k_l)|^2 e^{j2\pi k_l \tau (j-i)/N_t})}{\sum_{l=1}^{P_t} |\mathbf{X}_p(k_l)|^2} \tag{5.20}$$

Since our complex pilots are equi-power, we can conveniently assume that: $(|(\mathbf{X}_p(k_1)| = |(\mathbf{X}_p(k_2)| ..... = |(\mathbf{X}_p(k_{P_t})| = 1)$. Consequently, the normalized equation (5.20) can be re-written as:

$$\mu\{\mathbf{A}\} = \max_{1.\leq i\leq j\leq N_t, i\neq j} \sum_{l=1}^{P_t} \frac{1}{P_t} 1 e^{j2\pi k_l \tau (j-i)/N_t}) \tag{5.21}$$

From equation (5.21) it is evident that the value of $\mu\{\mathbf{A}\}$ will not rely on the pilot symbols, instead it only depends on the selected columns of dictionary $\mathbf{D}$. The dictionary $\mathbf{D}$ is a sparsifying matrix and is employed to realize the channel, it is mostly designed before channel estimation. Consequently, if $\mathbf{D}$ is constructed tactfully, dur-

ing the channel estimation $\mu\{\mathbf{A}\}$ will remain small and fixed. In short, from theorem 1 it is obvious that, for efficient channel estimation, a minimum coherence value is desired, therefore, the objective is to minimize $\mu\{\mathbf{A}\}$. The value of μ is generally in the range of [0-1], and the smaller value is desired to achieve better recovery [72].
The sparse channel reconstruction is based on the assumption that the channel response is sparse. In other words, the channel energy is uniformly distributed among the few dominant taps. However, the exact positions of these dominant taps are not known a priori and must be estimated for the effective channel measurement [73]. To estimate the exact positions, a redundant basis $\mathbf{D}$ is required. In conclusion, from the reduced and quantized pilots $\mathbf{Y}_{pi}$ and the dictionary $\mathbf{D}$, the channel estimate $\hat{\mathbf{H}}_i$ is obtained at the BS by utilizing the CS algorithms (i. e., Q-PJOMP, and Q-PJIHT), discussed in detail in the following subsection.

5.3.3 Algorithms for Sparse Channel Estimation

In some cases, it has been observed that the sparse data exhibit special structure in its measurement, for example, in a certain measurement, the sparse coefficients may form a group or block of zero and non zero entries. Such sparsity structure is known as group/block sparsity [37, 3]. This sparsity structure can be formulated by employing multiple measurements, known as joint sparsity [7, 39, 40]. In joint sparsity, each row of N vectors tends to be zero or non-zero simultaneously. The research work [74] demonstrates that the performance gain can be achieved if such structures are exploited in sparse measurements of the observed data. Consequently, the hidden joint sparsity structure of the correlated multi-users MIMO channel is exploited in the proposed DCS algorithms Q-PJOMP and Q-PJIHT. In both methods, it has been assumed that the sparsity information is known at the BS, which can be determined using slow-timescale stochastic learning [75, 76]. The proposed Q-PJOMP and Q-PJIHT are presented in Algorithm 2 and 3, respectively, where 2-step

quantization methods are labeled as A, 1-bit binary algorithm is indicated with B, and the common lines to both algorithms are marked with AB. If the algorithm 2 and 3 are viewed without label A, they transform into 1-bit Q-PJOMP/Q-PJIHT. Similarly, inspecting the algorithms without label B will convert them into the 2-step Q-PJOMP/Q-PJIHT. Both of the algorithms are presented subsequently in the following subsections.

Channel Recovery with Q-PJOMP (Algorithm 2):

The current subsection describes Q-PJOMP for partially joint channel estimation. Although several research works present the solution with joint sparsity through OMP based approaches [77, 78], the system with individual and partially joint sparsity still requires additional investigation. In [78] simultaneous joint OMP (SOMP) for multiple measurements sharing joint support is investigated. In the current work, the system with individual and partially joint support is considered. To handle this kind of structured sparsity, in the literature some works are already present. For example, in [79] a generalized joint sparsity model (GJSM) is developed.

Another research work [7] applies GJSM to exploit the hidden joint sparsity in massive MIMO channels for efficient resource utilization. Their main objective is to reduce the training overhead, which turns out in lowering the feedback overhead, although the number of feedback bits is still very high. Therefore, our focus is not only to reduce the number of measurements by taking advantage of joint sparsity structure among users channel but also to limit the number of feedback bits through a 2-step quantization process, while ensuring efficient reconstruction. To reduce the training overhead, our approach is inspired by [7] and [17]. In [7] the training overhead is lowered by considering the partially joint support structure among the user's channel.

Algorithm 2 Quantized Partially Joint-OMP

1 (AB): **Input:**$\mathbf{Y}_{pi} : i \in K$, $\mathbf{D}$

2 (AB): Measurement matrix $\leftarrow \mathbf{A}$,
support $= s_c, s_i$

3 (A) : Averaged quantized amplitude $\leftarrow Q(\mu)$

4 (AB): $\{Thresholds : \eta_1 < 1, \eta_2 > 1\}$

5 (AB): **Output:** Channel estimate $\hat{\mathbf{H}}_i$

Procedure:
Step 1 - Initialization:

6 (AB): support :$\{\Theta_i = 0, \Theta_c = 0\}$

7 (A) : $\mu' \leftarrow Q'(\mu)$

8 (AB): Compute $\mathbf{Y}_{pi}$ from (5.8) and $\mathbf{A}$ from (5.15) or (5.16)

9 (A) : The angle of $\mathbf{Y}_{pi}$ and the de-quantized amplitude are used to rebuilt $\mathbf{Y}_{pi}$
$\mathbf{Y}_{pi} \leftarrow \mu'\Big(cos\theta_{\mathbf{Y}_{pi}} + jsin\theta_{\mathbf{Y}_{pi}}\Big)$ and

10 (AB): Initialize residual $\mathbf{Res}_i = \mathbf{Y}_{pi}$

11 (AB): **Step 2 - Identify the common support:**
while $t \leq s_c$ **or** $\|\mathbf{A}^H\mathbf{Res}_i\|_F^2 \geq \eta_1$ **then**
identify the common support Θ_c that solves optimization problem
$\Theta_t \leftarrow Argmax \sum_i^K |\langle \mathbf{A}_s^H \mathbf{Res}_i \rangle|$
$\Theta_c \leftarrow \Theta_c \overset{s}{\cup} \Theta_t$

12 (AB): Determine the orthogonal projector $\mathbf{P}_o$ onto the span of the atoms indexed in Θ_c
$\mathbf{P}_o \leftarrow (\mathbf{A}_s)(\mathbf{A}_s)^\dagger$
$\mathbf{y}_o \leftarrow \mathbf{P}_o\mathbf{Y}_{pi}$
Residual Update:

13 (B) : $\mathbf{Res}_i \leftarrow \mathbf{Y}_{pi} - \text{sign}(\text{Re}(\mathbf{y}_o)) + j\text{sign}(\text{Im}(\mathbf{y}_o))$

14 (A) : $\mathbf{Res}_i \leftarrow \mathbf{Y}_{pi} - \mu'\Big(\cos\theta_{y_o} + j\sin\theta_{y_o}\Big)$
$t \leftarrow t + 1$

end

15 (AB): **Step 3 - Identify the individual support: initialize** $\Theta_i \leftarrow \Theta_c$
while $t_i \leq |s_i - s_c|$ **or** $\|\mathbf{Res}_i\|_F^2 \leq \eta_2$ **then**
$\Theta_{ti} \leftarrow \text{Arg max}|\langle \mathbf{A}_s^H \mathbf{Res}_i \rangle|$
$\Theta_i \leftarrow \Theta_i \cup \overset{s}{\Theta}_{ti}$
Residual Update:

16 (B) : $\mathbf{Res}_i \leftarrow \mathbf{Y}_{pi} - (\text{sign}(\text{Re}(\mathbf{y}_o)) + j\text{sign}(\text{Im}(\mathbf{y}_o))$

17 (A) : $\mathbf{Res}_i \leftarrow \mathbf{Y}_{pi} - \mu'\Big(\cos\theta_{y_o} + j\sin\theta_{y_o}\Big)$
$t_i \leftarrow t_i + 1$
end

Step 4 - Channel estimate The channel estimate is obtained

18 (AB): $\mathbf{B}_{si} = (\mathbf{A}_{\Theta_i})^\dagger \mathbf{Y}_{pi}$
$\hat{\mathbf{H}}_\mathbf{i} = \mathbf{D}\mathbf{B}_{si}$

While in our previous work [17] it is achieved by utilizing a flexible and robust dictionary-based measurement matrix. Besides reducing the training overhead, this work also lowers the number of feedback bits by introducing a 2-step quantization method. Q-PJOMP is based on a greedy algorithm select-discard OMP (SD-OMP) [79]. It can perform individual as well as partially joint sparse channel approximation by choosing the "best match" projection of multi-user quantized received pilots onto the span of the measurement matrix.

Initially, the received pilots are recomputed applying the de-quantized mean vector μ and the angle of 1-bit quantized vector $\mathbf{Y}_{pi}$ (line 9 in algorithm 2). Subsequently, the algorithm detects the common support for all the users, which consists of jointly selecting one column from the measurement matrix $\mathbf{A}$ in each iteration (line 11 step-2 in algorithm 2). The main intuition behind this selection is to determine an atom (column index) that contributes to the maximum amount of residual energy across all signals [80]. The indices that appear in common support Ω_c are likely to be estimated by most of the users. In each iteration, new support is appended to the existing support set unless a stopping criterion is satisfied. Another important step is to orthogonalize the residual $\mathbf{Res}_i$ with the selected atom (column) of the measurement matrix (line 12 of Algorithm 2) so that each atom is chosen only once as in [81, 78]. In the next step, the individual support of each user is identified as in standard OMP (lines 15 step-3 in algorithm 2) [81]. Indeed, besides the common support, also a few individual supports may be present in each signal. Note that the indices of the measurement matrix which were already been taken by common support, are discarded by the individual support. The rest of the procedure is the same as the common support identification. Afterward, the complex pilot at each support index is recomputed and updated (lines 13 and 14 for common support and lines 16 and 17 for individual support in algorithm 2) in a design similar to [82], although the overall procedure and problem are different from the proposed. Finally, the channel

is estimated using the LS approach (lines 18 step-4 in algorithm 2). To achieve stable recovery, there are different stopping criteria. For example, the algorithm will run for a particular number of iteration or will be executed until the norm of residual remains positive $\|\mathbf{Res}_i\| \geq \eta_2$. In our case, the system will halt if the correlation between the atom of a matrix $\mathbf{A}$ and the residual drops below a threshold η_1;, which we set ($\eta_1 = 0.04$) in our simulation.

Channel Recovery with Q-PJIHT (Algorithm 3):

We here describe the Q-PJIHT algorithm to estimate partially joint sparse channel, whose performance is then compared with the previously detailed Q-PJOMP.

The research work [39] presents the 1-bit solution with joint sparsity through IHT based approaches. However, the system with joint sparsity and quantized feedback still require improvements. In [83] 1-bit quantization is proposed, later to reduce hardware cost and system processing burden, the research work [39] utilizes this 1-bit per dimension to estimate the partially joint channel in a massive MIMO system. The proposed Q-PJIHT algorithm explores both individual and joint sparsity support as in [39], although we apply a different quantization procedure that includes the amplitude as well as the sign information. The proposed work also selects the optimal step size (η) depending on the sparsity level and dictionary length M. Indeed, since IHT is a gradient descent based algorithm, its step size must be chosen optimally for better convergence [35].

Initially, in Algorithm 3, the received pilots are recomputed by applying the de-quantized mean vector and the angle of 1-bit quantized vector $\mathbf{Y}_{pi}$ (step-1 line 10 in Algorithm 3). Subsequently, after initializing the residual and the support, the algorithm detects the common support (step-2 line 13 in Algorithm 3) for all the users. In the next step, the individual support is calculated (step-2 line 14 in Algorithm 3) in the same way performed in Algorithm 2. The algorithm is based on gradient descent

technique that works iteratively to realize a robust estimate. Although standard IHT based algorithms are computationally simple and take less memory than standard OMP based methods, they have several challenges while dealing with the practical problem. As an example, the stable signal recovery highly depends on the selection of step size η, sparsity parameter [35] and number of iterations.

5.4 Performance Evaluation

The performance of the proposed scheme is evaluated using various CS techniques and different metrics. The proposed 2-step Q-PJIHT is compared with 1-bit Q-PJIHT whose algorithmic construction is inspired by 1-bit BIHT [39]. The 2-step Q-PJIHT differs from 1-bit BIHT in terms of considering channel direction and partial amplitude information. Similarly, the Q-PJOMP is proposed and its 1-bit and 2-step versions are taken into account for analysis. Q-PJOMP has considered the equivalent joint channel sparsity model as in JOMP [7]. Moreover, both Q-PJIHT and Q-PJOMP differ from [7], [39] in terms of employing more robust sparsifying basis $\mathbf{D}$. The primary goal of this presented framework is to reduce the number of measurements and feedback bits while preserving high performance.

5.4.1 Simulation Setup

We consider a MIMO-OFDM system, with $N_t = 128$ transmit antennas, $N_r = 2$ receive antenna and $K = 10$ number of users. The BS uses 256 OFDM subcarriers for downlink transmission while some sub-carriers are employed for pilot sequences and others for data. Specifically, during the first phase of training, only training pilots are sent without data, while in the second phase both data and pilots are transmitted in combo fashion. The dictionary length M is set to 300, whose value can be increased to reduce the error rate at the cost of higher processing. After varying M up to 512

we selected 300 as a good compromise between performance and computation. We assume a system without frequency offset among the local oscillators at the transmitter and the receivers. Moreover, the multipath fading channel with iid additive white Gaussian noise with zero mean and unit variance is considered. The multipath channel length L_{taps} is set equal to 6, whose consequent ISI is directly solved by the OFDM guard interval G, moreover, the length of G is set to 16. The joint sparsity s_c and the individual sparsity s_i parameters are chosen to be 6 and 10 respectively, where s_c and s_i are defined in Sec. 5.2.2. Table 5.1 summarizes the system parameters. In the following subsections, the performance analysis is presented evaluating different metrics, i. e., signal to noise ratio (SNR) degradation, normalized mean squared error (NMSE) as in [7] for the channel state information at the transmitter (CSIT), and bit error rate (BER) while detecting the data at each user terminal.

5.4.2 SNR Degradation

Although we developed the full system including channel estimation, beamforming procedure and data detection, our main aim is the channel estimation. Thus, in this subsection we specifically evaluate the effect of both the received pilots quantization and the number of employed pilots on the channel estimate through SNR degradation, as shown in Fig. 5.3. In particular, equation (5.22) gives the averaged SNR loss obtained using the estimated channel with different numbers of pilot symbols as in [39]. For channel $\mathbf{H}_i$ and its estimate $\hat{\mathbf{H}}_i$, the precoder $\mathbf{w}_i$ is the maximizer of $\|\mathbf{w}_i^H \mathbf{H}_i \mathbf{H}_i^H \mathbf{w}_i\|_2^2$ and $\hat{\mathbf{w}}_i$ is the maximizer of $\|\hat{\mathbf{w}}_i^H \hat{\mathbf{H}}_i \hat{\mathbf{H}}_i^H \hat{\mathbf{w}}_i\|_2^2$, respectively. The overall SNR loss in dB can be calculated as follows

$$\mathrm{SNR}_{deg} = 10\log_{10} \frac{\|\mathbf{w}_i^H \mathbf{H}_i \mathbf{H}_i^H \mathbf{w}_i\|_2^2}{\|\hat{\mathbf{w}}_i^H \hat{\mathbf{H}}_i \hat{\mathbf{H}}_i^H \hat{\mathbf{w}}_i\|_2^2} \tag{5.22}$$

Around 200 simulations have been performed to obtain the channel estimate $\hat{\mathbf{H}}_i$ and the precoder $\hat{\mathbf{w}}_i$, which are used in equation (5.22) to calculate the averaged SNR degradation. Fig. 5.3 analyzes the SNR degradation employing Q-PJIHT or Q-PJOMP having 1-bit or 2-step quantization using either DFT or dictionary-based sparsifying matrices. It can be observed that when the feedback overhead approaches 48 pilots, the SNR degradation exceeds 2 dB in 1-bit method [39], which is more than the degradation achieved by the proposed 2 bit Q-PJOMP.Overall, the proposed 2-step Q-PJOMP outperforms the other schemes, which is due to several reasons: firstly, Q-PJOMP is more efficient than the IHT based algorithm (Q-PJIHT). Secondly, since the choice of η is critical in IHT [35], a flexible gradient step size η is employed in the Q-PJIHT algorithm.

The η is used as per sparsity level requirements in each iteration, contrary to a fixed-size of 0.01 used in [39]. Thirdly, the 2-step quantization preserves both amplitude and phase information rather than having only direction information as in the compared 1-bit feedback method [39].

Finally, our system employs a dictionary-based sparsifying matrix, which, as shown in [17], is more robust to estimate the channel as compared to earlier research works [39, 7]. From Fig. 5.3 it can be easily noticed that with 64 pilots in the magnified view, the proposed quantized feedback Q-PJOMP with a dictionary-based approach surpasses the performance of almost all feedback based algorithms. Moreover, by increasing the number of pilots, the SNR loss drops down to almost zero for all the solutions. Finally, focusing on the proposed Q-PJOMP method in Fig. 5.3, the 2-step quantization reflects less degradation as compared to the 1-bit quantization.

Algorithm 3 Quantized Partially Joint-IHT

(AB): **Input:**$\{\mathbf{Y}_{pi} : i \in K\}$, $\mathbf{D}$

(AB): Measurement matrix $\leftarrow \mathbf{A}\}$

(AB): Sparsity level S $\leftarrow s_c, s_i,$

(A) : Averaged quantized amplitude $\leftarrow Q(\mu)$

(AB): Step size: $\eta \leftarrow \frac{1-\sqrt{\frac{S}{M}}}{M}$

(AB): **Output:** Channel estimate $\hat{\mathbf{H}}_i$

Procedure:
Step 1 - Initialization:

(A) : $\mu' \leftarrow Q'(\mu)$

(AB): Compute $\mathbf{Y}_{pi}$ from (5.8) and $\mathbf{A}$ from (5.15) or (5.16)

(AB): The angle of $\mathbf{Y}_{pi}$ and the de-quantized amplitude are used to rebuilt $\mathbf{Y}_{pi}$

(A) : $\mathbf{Y}_{pi} \leftarrow \mu'\Big(\cos\theta_{\mathbf{Y}_{pi}} + j\sin\theta_{\mathbf{Y}_{pi}}\Big)$

(AB): Initialize residual $\mathbf{Res}_i^o = \mathbf{Y}_{pi}$
$\mathbf{B}_{si}^o \leftarrow \mathbf{A}^H\mathbf{Res}_i^o$
$\Theta_i \leftarrow 0$
$\Theta_c \leftarrow 0$

Step 2 while(maximum iteration) do

(AB): $\mathbf{B}_{si}^{n+1} = \mathbf{B}_{si}^n + \eta\mathbf{A}^H\mathbf{Res}_i^n$

(AB): Identify the common support Θ_c that solves the optimization problem
$\Theta_t \leftarrow \underset{s}{\text{Arg max}} \sum_i^K |\langle \mathbf{A}_s^H\mathbf{Res}_i\rangle|$
$\Theta_c \leftarrow \Theta_c \cup \Theta_t$
Repeat the process s_c times

(AB): Identify the individual support:
Initialize $\Theta_i \leftarrow \Theta_c$
$\Theta_{ti} \leftarrow \underset{s}{\text{Arg max}}|\langle \mathbf{A}_s^H\mathbf{Res}_i\rangle|$
$\Theta_i \leftarrow \Theta_i \cup \Theta_{ti}$
Repeat the process $|s_i - s_c|$ times

(AB): Hard threshold all the entries except those indexed in Θ_i
$\mathbf{B}_{si}^{n+1} \leftarrow H_T(\mathbf{B}_{si}^{n+1}, \Theta_i)$
Residual Update :

(AB): $\mathbf{y}_o \leftarrow \mathbf{A}_\Theta\ \mathbf{B}_{si}^{n+1}$

(B) : $\mathbf{Res}^{n+1} \leftarrow \mathbf{Y}_{pi} - \text{sign}(\text{Re}(\mathbf{y}_o) + j\text{sign}(\text{Im}(\mathbf{y}_o)$

(A) : $\mathbf{Res}^{n+1} \leftarrow \mathbf{Y}_{pi} - \mu'\Big(\cos\theta_{y_o} + j\sin\theta_{y_o}\Big)$

end

(AB): **Step 3 - Channel estimate**
The spare channel is estimated by repeating the process until $\mathbf{Y}_{pi}$ is consistent with $\mathbf{B}_{si}$ or the stopping criteria is met. $\hat{\mathbf{H}}_i \leftarrow \mathbf{DB}_{si}$

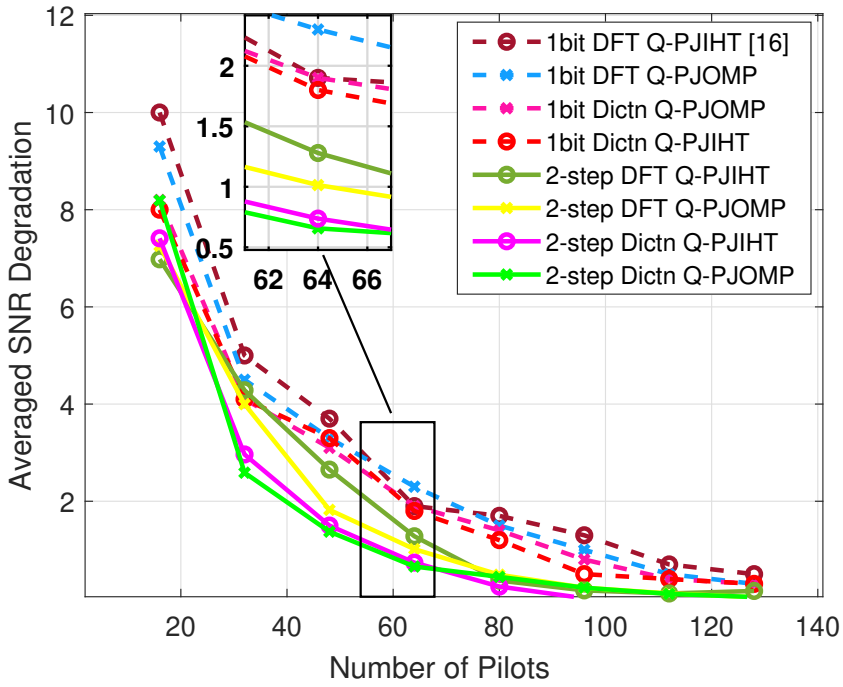

Figure 5.3: Averaged SNR degradation for 1-bit and 2-step quantization using DFT and Dictionary basis.

5.4.3 CSIT NMSE analysis Versus common support

Fig. 5.4 illustrates the NMSE of CSIT while increasing the common support s_c, under the same simulation parameters [7] for the comparison purpose. The simulation parameters are enlisted as followed: number of transmit pilot P = 45, $N_t = 160$, N_r

Table 5.1: Simulation parameters

Parameter	**Symbol**	**Value**
Transmit antennas	N_t	128
Receive antennas	N_r	2
Users	K	10
OFDM subcarriers	N_o	256
OFDM guard interval	G	16
QAM Modulations	QAM	4
Multipath channel length	L	6
Dictionary length	M	300

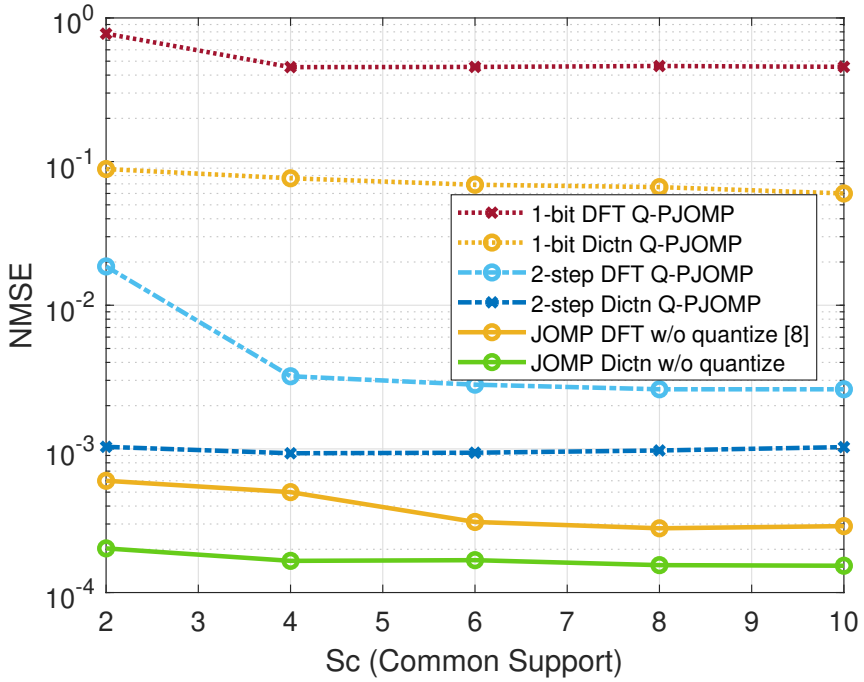

Figure 5.4: NMSE of CSIT vs common support for 1-bit, 2-step quantization using Q-PJOMP and without quantization, under P = 45, N_t = 160, N_r = 2, K = 40, s_i = 17 and transmit SNR = 28 dB.

= 2, K = 40, $s_i = 17$ and $SNR = 28$ dB. NMSE has been calculated as follows:

$$\text{NMSE} = \text{E}\left(\frac{\|\mathbf{H}_i - \hat{\mathbf{H}}_i\|_F}{\|\mathbf{H}_i\|_F}\right) \tag{5.23}$$

The individual and joint sparsity levels are generated using the spatial channel model (SCM)[2] as in [39, 7]. Fig. 5.4 reveals as the common support s_c increases among users, the system performance improves, i. e., when the channel between users is more correlated. The results confirm that the 2-step quantization provides a better estimation than the 1-bit scheme and approaches the techniques without quantization with a much lesser number of bits. The 1-bit quantization method (1-bit DFT Q-PJOMP) in Fig. 5.4 has the worst performance because it uses only direction

[2]3rd generation partnership project(3GPP) and the international telecommunication union(ITU) has developed a spatial channel model(SCM) to model various urban and rural propagation scenarios [24]

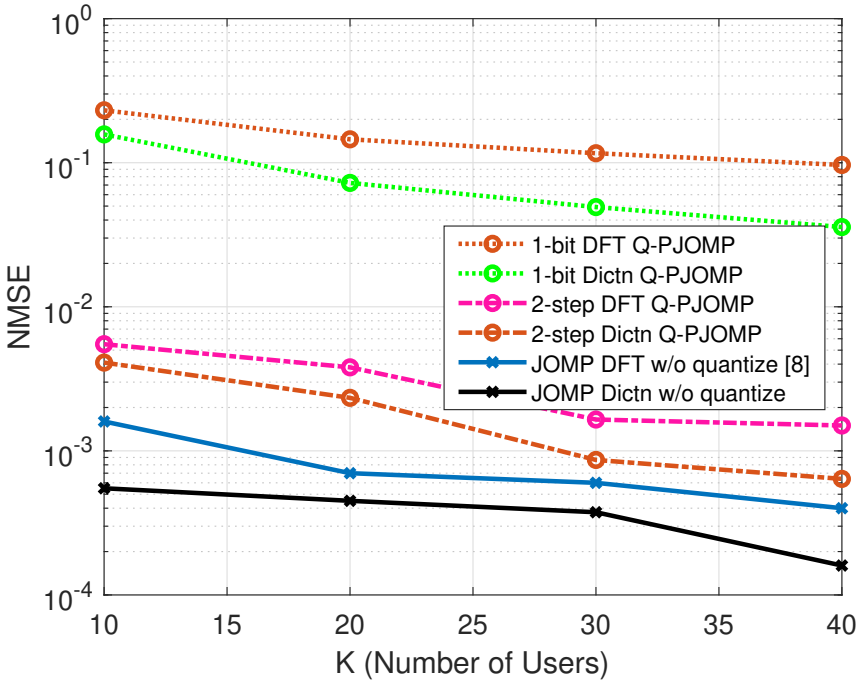

Figure 5.5: NMSE of CSIT vs number of users for 1-bit, 2-step quantization using Q-PJOMP and without quantization, under P = 45, N_t = 160, N_r = 2, s_c = 10, s_i = 17 and transmit SNR = 28 dB.

information and also DFT basis, instead of the more robust dictionary as in 1-bit Dictn Q-PJOMP. Comparing only the methods without quantization, it can also be observed that the proposed JOMP algorithm with a dictionary basis gives better performance than DFT based JOMP [7]. This point validates one of our contributions that joint channel estimation is more reliable with dictionary basis.

5.4.4 CSIT NMSE analysis Versus Number of Users

Fig. 5.5 illustrates the NMSE of CSIT while increasing the numbers of users. The NMSE is calculated by using equation (5.23). The simulation parameters are enlisted as followed: number of transmit pilot P = 45, N_t = 160, N_r = 2, s_c=10, s_i = 17 and SNR = 28 dB and number of users are increased from 10 to 40. From Fig. 5.5 it can be noticed that the performance improves when the number of users increase. The performance gain is due to the fact that the proposed algorithm utilized

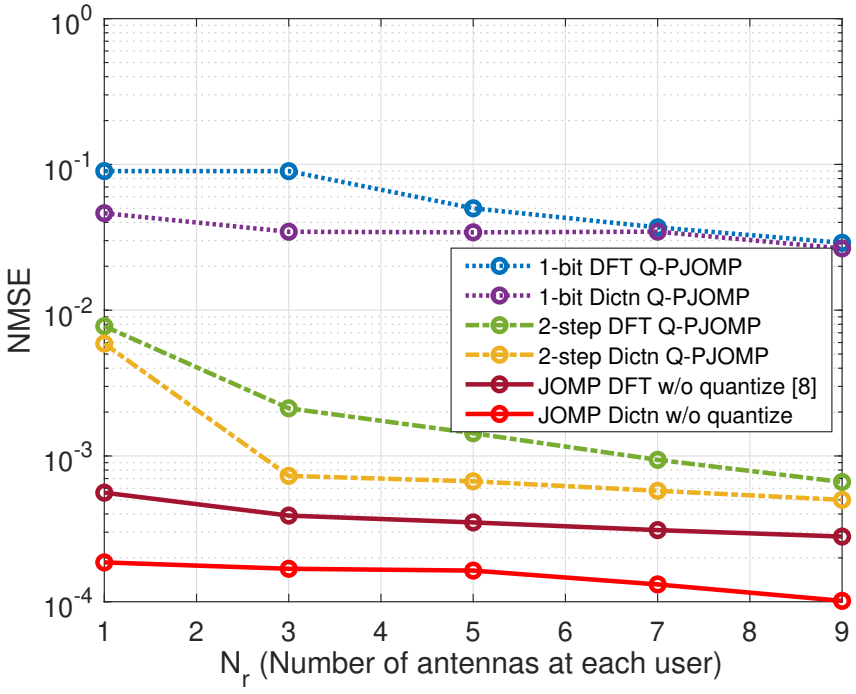

Figure 5.6: NMSE of CSIT vs number of antennas at each user for 1-bit, 2-step quantization using Q-PJOMP and without quantization, under P = 45, N_t = 160, user = 40, s_c = 10, s_i = 17 and transmit SNR = 28 dB.

the distributed joint sparsity between user's channel matrices to jointly detect the common support. With more number of users, the system will have adequate amplitude knowledge and improved common support resulting in a reliable estimate. It can be observed that the performance is improved if both amplitude and directional information is considered, as in 2-step quantization. All the algorithms utilizing the dictionary basis for the estimate of CSIT have superior performance.

5.4.5 CSIT NMSE analysis Versus Number of receive antennas

Fig. 5.6 illustrates the NMSE of CSIT while increasing the number of antennas at each user by using equation (5.23). The simulation parameters are enlisted as followed: number of transmit pilot P = 45, N_t = 160, users = 40, s_c=10, s_i = 17 and SNR = 28 dB and number of antennas at each user are increased from 1 to 9. From Fig. 5.6 it can be seen that with the increase in number of receive antenna

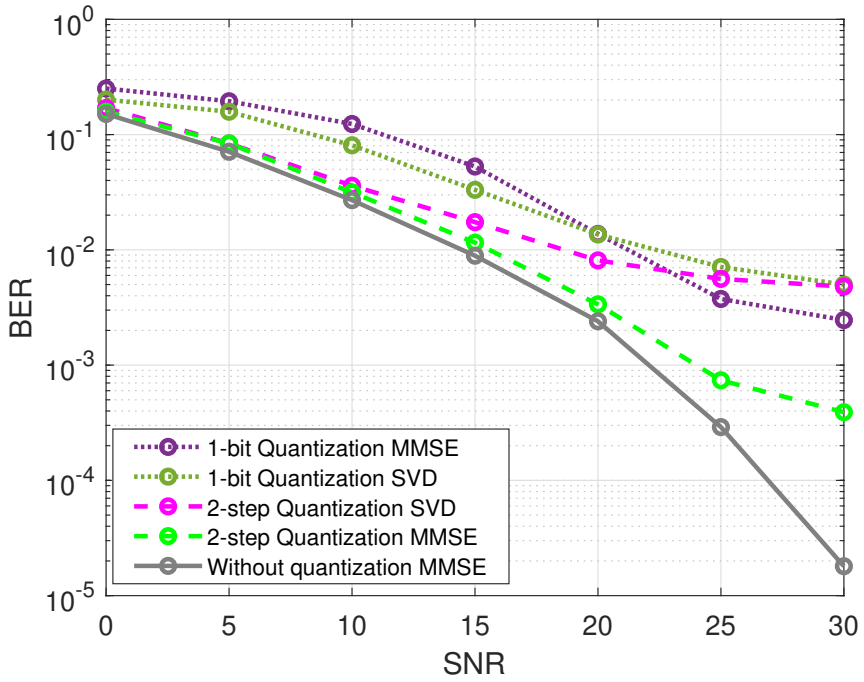

Figure 5.7: Averaged Multi-user detection with quantized CSIT based MMSE beamforming (1-bit, 2-step Q-PJOMP) and without quantization.

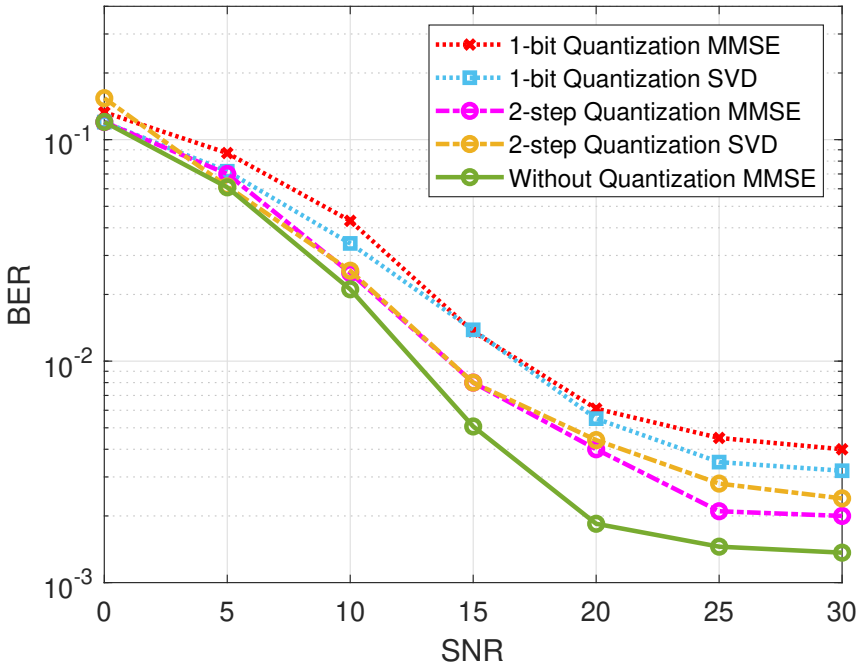

Figure 5.8: Averaged Multi-user data detection with quantized CSIT based beamforming (1-bit, 2-step Q-PJIHT) and without quantization

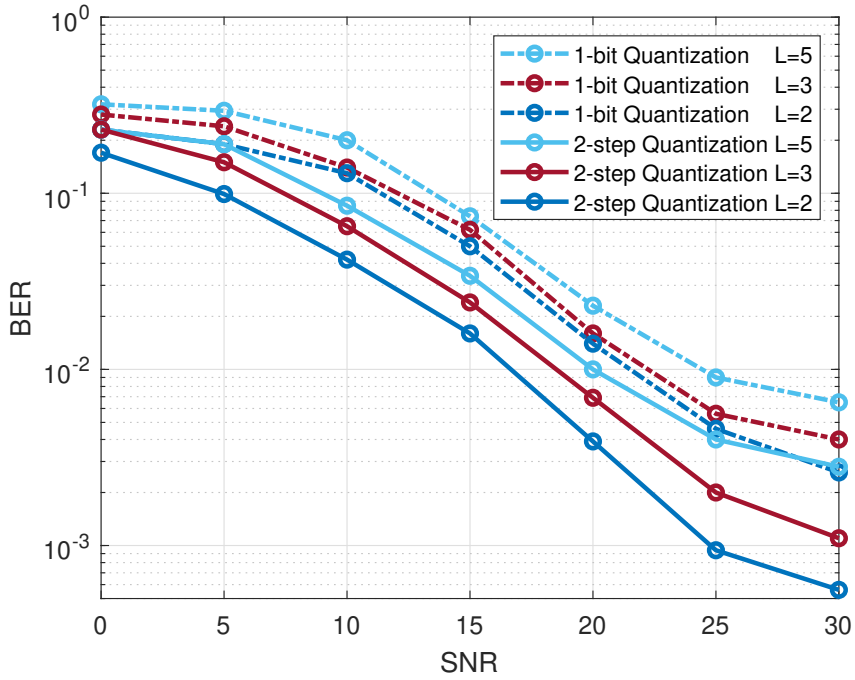

Figure 5.9: Averaged Multi-user detection with quantized CSIT based MMSE beamforming (1-bit, 2-step Q-PJOMP) with varying channel taps L

at each user the performance improves, due to the individual joint sparsity present in the channel matrix. Hence, the CSIT quality will be enhanced by increasing N_r. As expected, similarly to Fig. 5.5 and 5.4, the performance of 2-step quantization is better than 1-bit quantization. Moreover, with the dictionary basis, the CSIT estimate is improved as compared to the DFT basis in all cases. Hence, by increasing the number of antennas at the mobile station more reliable individual joint support is identified, resulting in a robust channel estimate.

5.4.6 BER Analysis

Fig. 5.7 and 5.8 present the comparison of BER versus SNR for data detection techniques utilizing SVD and MMSE based beamforming. The channel estimate required for beamforming is obtained using quantized feedback and applying CS techniques based on JOMP and JIHT. Moreover, the beamforming obtained without quantized

feedback is presented for comparison purposes. It is worth noting in Fig. 5.7 that beamforming based on channel estimate acquired using 1-bit feedback has a wider gap from the algorithms without quantization. Moreover, Q-PJOMP with MMSE based precoding gives better results than its SVD counterpart. As shown in Fig. 5.7 and 5.8 , the proposed 2-step quantization methods show better performance when applying MMSE beamforming than SVD.

Specifically, at high SNR MMSE outperforms SVD since it is more power-efficient. On the contrary, Fig. 5.7 and 5.8 illustrate that both 1-bit versions of the proposed algorithms, i. e., 1-bit Q-PJIHT and Q-PJOMP, show lower performance when employing MMSE than SVD in all the SNR range. The reason may be due to the fact that 1-bit quantization lacks power information while MMSE is a power efficient beamformer, therefore without power information it is not performing well. By comparing Fig. 5.7 and 5.8, it can be observed that Q-PJOMP exhibits better performance as compared to Q-PJIHT for almost all the cases with and without quantization. Fig. 5.9 shows the effect of multipath fading over data detection by employing MMSE beamforming utilizing quantized 1-bit and 2-step feedback using Q-PJOMP based channel estimates. It can be observed that, as expected, by increasing the number of channel taps from 2 to 5 the BER performance in all cases is reduced, though the proposed technique yields the improved results.

5.4.7 Computational Complexity Analysis

In this subsection, the computational complexity comparison between the proposed IHT based algorithm Q-PJIHT and OMP based algorithm Q-PJOMP is given. The overall computational complexity for Q-PJOMP method is $\mathcal{O}(K\ s\ M\ N_r\ T)$ and for Q-PJIHT is $\mathcal{O}(I\,K\,M\,N_r\,T)$, where I is the total number of iterations. The complexity in terms of Big-O notation will be the same for the 1-bit and the 2-step quantization versions of the proposed algorithms, since Big-O notation shows how an algorithm's

complexity scale when the number of parameters are increased. However, while processing the algorithms with real hardware, the lower computational complexity of 1-bit method compared to the 2-bit algorithm will be more noticeable in terms of processing time. Table 5.2 presents the comparison of computational time per user for 2-step and 1-bit Q-PJOMP/Q-PJIHT. Three different transmit antennas setting has been considered: N_t= [50, 100, 150]. As expected, the computational time increases with the number of transmit antennas. Furthermore, the 2-step algorithms (Q-PJOMP/Q-PJIHT) are more expensive than 1-bit methods. This is due to the processing of the channel amplitude information and rebuilding complex pilots from both amplitude and direction information, nevertheless, the analysis reveals that the difference is not very significant. Finally, comparing Q-PJOMP with Q-PJIHT, it has been observed that iterative hard thresholding based techniques (1-bit and 2-step quantization) are generally much slower than the orthogonal matching pursuit based techniques since they require a certain number of iteration to reach an optimal point.

Table 5.2: COMPLEXITY COMPARISON FOR MU-MASSIVE MIMO UNDER PARAMETRIC SETTING P = 45, N = 2, K = 40, $s_c = 9$, $s_i = 17$, P = 28 dB AND N_t= 50,100, 150.

Time (s)	N_t=50	N_t=100	N_t=150
2-step Q-PJOMP	1.20×10^{-3}	1.40×10^{-3}	1.60×10^{-3}
1-bit Q-PJOMP	9.24×10^{-4}	1.20×10^{-3}	1.30×10^{-3}
2-step Q-PJIHT	6.86×10^{-2}	7.19×10^{-2}	7.38×10^{-2}
1-bit Q-PJIHT	5.82×10^{-2}	6.94×10^{-2}	7.02×10^{-2}

5.5 Conclusion

We have presented distributed compressed sensing based channel estimation techniques for the partially joint channel in a massive MIMO system. A novel Q-PJOMP

and Q-PJIHT based channel estimation algorithms are proposed that utilize limited quantized feedback. Our system reduces training and feedback overhead for channel estimation by employing a fewer number of pilots along with a limited number of feedback bits. The channel is jointly recovered for all users by applying DCS at BS from 2-step quantized feedback. Results revealed that SNR degradation with 2-step quantized feedback is less than 1 dB for 64 pilots. Furthermore, as the number of pilots grows, the SNR degradation approaches closer to zero. Additionally, the presented dictionary-based system aids in reducing the training and feedback overhead. This is achieved by exploiting an improved CS algorithm and pilot design. Finally, when the channel among users is highly correlated and exhibits added common support, the jointly estimated channel at BS will reduce the computational resources and time.

6

Beamforming Galvanic Coupling

6.1 Introduction

Assistive technologies allow humans to augment their natural abilities and restore physiological functions lost due to illness or injury. An example of today's closed loop communication with man-machines interfaces involves controller-driven artificial limb stimulation based on muscle exertion levels. Embedded sensors in the tissue detect the muscle stress and communicate their readings back to the controller for precisely computing the needed stimuli for limb movement [84]. This paradigm of interconnected implants results in an Intra-Body Network (IBN) that allows internal physiological data to be gathered in real time and analyzed off site, thereby transforming personalized medicine. However, the state of the art for Intra-Body Communication (IBC) relies on high frequency radio (RF) signals. RF incurs significant energy costs owing to high absorption within the human tissues that are composed

of 40-65% water. Additionally, emitted RF signals may extend to several feet around the body, creating privacy risks. We use an alternative wireless architecture for IBNs using galvanic coupling (GC), in which low or medium frequency (100 kHz-1 MHz) and weak (≤ 1 mW) electrical currents are modulated with data and directly coupled to the tissue. The privacy risks related to RF are eliminated by using GC in IBNs since the signals do not propagate outside the skin layer [15]. GC is a method of IBC also commonly referred to as human body communication (HBC). For consistency we will continue to refer to it as an IBC method. We call this paradigm as GC-IBN, and it consumes two orders of magnitude less energy than RF signals [85].

• **Problem:** The GC-IBN architecture is composed of multiple embedded implants that transmit their sensed data to an on-skin node, called as a *relay*. The muscle to muscle (M-M) path offers lowest path-loss ($\approx$ 19 dB) and hence, is ideally suited for communication across different implants in the same muscle layer [85]. However, implant to the surface relay communication needs to traverse several different tissue boundaries that have higher path loss, for e.g, the muscle to skin (M-S) path has $\approx$ 38 dB of loss. How to send these signals to the relay with the least overhead (even if the baseline GC performance is much more energy efficient than RF) with high SNR remains an open challenge [86, 87]. Further, existing standards like IEEE 802.15.6 designed for implant communication use contention-based medium access with the possibilities of collisions, back-off and packet loss. Such events incur energy costs of re-transmissions and idle-listening, which we wish to avoid in IBNs.

• **Proposed Approach:** We propose a light-weight cross-layer framework that combines compressive sensing code division multiple access (CS-CDMA) with distributed beamforming in narrow band channels, while ensuring that computational costs are delegated to the relay. We define beamforming in the context of this near-field application as the phase tuning of GC signals to achieve constructive interference between multiple implant transmissions and improve the SNR at the relay. The implants

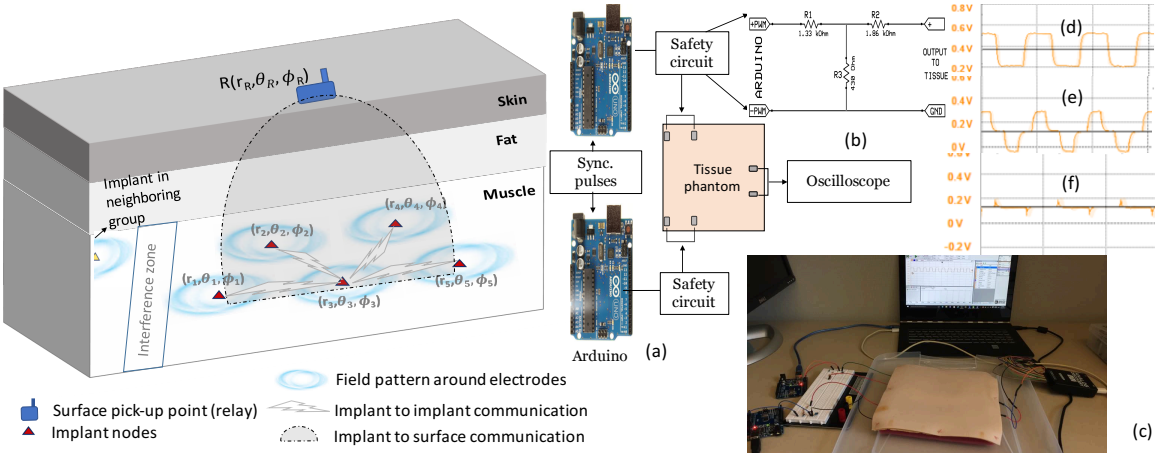

Figure 6.1: (left) Human fore-arm GC-IBN with muscle implants and surface relay; (right) Phantom-based testbed using Arduino

themselves simply record and forward data, with the relay being responsible for both the CDMA decoding (to extract the actual sensed value) and tuning of the beam-steering matrix (for directional communication with high SNR). Existing far-field beamforming techniques cannot be applied for GC-IBN, as the receiver is placed in the near-field of the low frequency transmitter, separated only by a few centimeters.

The end to end procedure is described as follows: The relay assigns unique CDMA codes to the implants. The latter store the sensed values and create modulated codewords using these assigned quasi-orthogonal codes. Using the high-gain M-M channel, the implants inform a designed aggregator, placed in the same muscle tissue, of their individual codewords. Such aggregator records the received CDMA-coded data structure created by the simultaneous transmissions of multiple sensors on the same channel. Note that there is no decoding step at this point to save energy and the aggregator simply broadcasts back this cumulatively received codeword to the implants. By using distributed beamforming, each implant then transmits this codeword to the relay. Through this process, the energy consumed per implant is reduced, greater directional transmission is obtained and the relay receives much higher SNR than what would have been possible via a single transmission. The final CDMA decoding is then performed at the relay, and the individual sensor data is then

extracted. The entire 2-step process of (i) exchanging individual codewords among peer implants, and (ii) beamforming to the relay, is collision-free.

• **Contributions:** The main contributions of the work presented in the current chapter are:

1. We propose a CS-CDMA-based cross-layer approach that allows implants in the muscle to communicate with surface relays using galvanic coupling, which is collision-free and has reduced complexity of decoding.

2. We present the first formulation of near-field distributed beamforming in the body that accounts for specific tissue paths, constraints of tissue safety ($\leq 25\, mA/m^2$) [87] and increases SNR at the surface relays. We present tissue-phantom and Arduino-based proof of concept of how constructive phase addition is possible within the body.

3. We use empirically obtained data sets to model the body channel and evaluate the effectiveness of our approach using an extensive finite element based simulation using MATLAB-generated mathematical models.

4. We demonstrate GC-beamforming through the muscle, fat and skin layers on a testbed using National Instruments Universal Software Radio Peripherals (USRPs) where we transmit data from multiple sensors through a human tissue phantom. Our measurements of received signal strength and BER at the demonstrate the merits of using beamforming within a physical intra-body sensors communication system.

6.2 Background and Related Work

Existing standards for Wireless Body Area Communication (WBAN), including IEEE 802.15.4 based LR-WPAN (Zigbee), IEEE 802.15.6 Human Body Communication (HBC) standard and Bluetooth low energy (BLE), assume that implants are similar to classical over-the-air wireless sensor networks.

This is because in both cases, the nodes are battery powered, have small form fac-

tors, with low on-board resources. Classical CSMA/CA [88, 89] and channel hopping used in these standards impacts definite time of delivery, energy efficiency, and is unable to handle sudden spikes in traffic. The frame-length and inter-frame spacing are designed for high frequency signal propagation in the air medium over long distances ($>>2\,\mathrm{m}$), rather than the low frequency short range communication ($< 50\,\mathrm{cm}$) inside the body. Other overheads such as handshakes, channel sensing, scheduling, transitions from frequent sleep and wake-up states, among others, increase the processing complexity. An alternative form of intra-body links established using ultrasonic signals suffer from high multi-path delay and complex circuitry.

We note that the low rate and sparse traffic generated by implants under normal physiological conditions may become bursty when an abnormal event is observed, limiting utility of both contention-based and reservation-based access techniques. Hence, for contention and reservation-free access, we advocate the use of [90] that enables concurrent transmissions. However, CDMA multiplies the energy costs by using a high rate code, which in turn contributes to the net energy consumed per unit of useful data. Thus, due to the sparse nature of sensed data, we apply a combined CS-CDMA procedure to reduce the transmission time and energy. CS based solutions have been already successfully applied [31] to both recover data and identify the transmitters. In this work, we further combine energy efficient CS-CDMA solution with smart energy-focusing strategies. Seminal contributions for conventional beamforming in far-field, high frequency signals exist [91]. However, the problem of beamforming for near-field and narrow band signals in a heterogeneous tissue-like medium has not been demonstrated so far, particularly for the low frequency signals ($<$1 MHz) used in GC-IBN. Coordinated beamforming using multiple separate antenna elements may be possible in many applications where implants are placed in close proximity of each other, such as neuro-muscular stimulators or orthopedic sensors that merits further investigation on this topic [84, 92].

6.3 Tissue Phantom Experiments

As a motivation for choosing beamforming, we use a tissue phantom-based preliminary testbed (see Fig. 6.1(a) for the block diagram describing the setup and Fig. 6.1(c) for a snapshot) to analyze the constructive and destructive combination of concurrently propagating signals through tissue. We use a dielectrically equivalent human tissue phantom with a skin, fat and muscle layer purchased from SynDaver®. The 20 x 20 x 3.1 cm^3 phantom was constructed from salt, water and fiber and was ordered specifically for GC tests to have the dielectric values presented in Table 6.3. The three layers (skin, fat, muscle) were stitched together by the manufacturer. We use pulse width modulated (PWM) signals at 100 kHz and 0.5 V generated by a pair of Arduino Uno boards, whose phase is controlled by a common synchronization pulse generated by MATLAB. The PWM signals are passed through a safety circuit (Fig. 6.1(b)) in order to limit the signal within the safe bound (=1 mA) we set based on the suggestion by ICNIRP [87] and then coupled to the muscle phantom (mimicking implants) by two pairs of electrodes. The transmitters are separated by 16 cm and the electrode pair in each transmitter is separated by 4 cm. A pair of receiving electrodes is positioned on the surface skin of the phantom at 15 cm from each transmitter, and connected to an oscilloscope to observe the output voltage. For each signal, the corresponding Thevenin-equivalent circuit is built to measure the output power level. When only one Arduino is transmitting a power of 0.25 mW, the maximum average output power (Pr_{max}) we observed is 3 μW. When two transmitters are transmitting concurrently, and in perfect phase alignment (Fig 6.1(d)), Pr_{max} is 6 μW, which is double than the case of a single transmitter. This shows that the constructive signal addition is beneficial. However, when the input signals are out of phase (Fig 6.1(e)), $Pr_{max} \approx 2.6\,\mu$W, which is lower than the case of a single active transmitter, showing the impact of destructive signal combination. When the signals are partially out

of phase (Fig. 6.1(f)), Pr_{max} becomes $\approx 4.3\,\mu$W. The set-up includes the mutual coupling effect from multiple transmitters and thus mimics the real scenario. Our experiments motivate the potential benefits of phase-alignment based beamforming within heterogeneous tissues using GC-coupled links. We extend this testbed further in Section 6.5 where the constructive and destructive combination of galvanic signals is explored further by applying the weights calculated in the following section.

6.4 Beamforming for Implant Communication

In this section we develop the theoretical background for beamforming using an array of implants acting as distributed antennas. We assume that each implant has a common CDMA modulated codeword $\tilde{\mathbf{d}}$ that is created and disseminated by the aggregator back to the implants and focus on the formulation of the beamforming weights. In preparation to that, we first explain the channel between implants and from the implant to the relay in Sec.6.4.1. Following that, Sec.6.4.2 justifies the use of near-field transmissions followed by a description of the electric field of one the GC transmitter in Sec. 6.4.3. We extend the electric field analysis to the array-structure resulting from multiple nearby implants, and then calculate the cumulative received power at the surface relay in Sec.6.4.4. Then, we derive the complex weights to limit the beam-formed signal within the safe power limit, focus the signal strength at the receiver and devise a method to steer the input signals from each node in the desired direction in Sec.6.4.5.

6.4.1 Implant network and 3-D tissue channels

We assume a set of M uniformly distributed co-planar implants $\{m_1, .., m_M\}$ arranged in muscle tissue linearly, at locations (r_m, θ_m, ϕ_m), where $r_m \in [0, r_{max}]$ is the maximum distance of separation in muscle. Let $\theta_m \in [0, 2\pi]$ be the azimuth angle measured

from the X-axis, and $\phi_m \in [0, \pi]$) be the elevation angle measured from the Z-axis, respectively, all in radians, with the origin at $(0, 0, 0)$ as shown in Fig.6.2. The number of implants in a given body part can vary from 1 to M, for e.g., neural stimulation uses more than 50 implanted cuffs in one limb [84, 94]. The external relay node R on the body surface controls the actions of the implant-group by issuing synchronization pulses, aggregating their information, providing receiver feedback for beamforming and decoding the sensed values [95]. It is located at $(r_R, \theta_R, \phi_R) = (T, 0, 0)$, where T is the tissue thickness separating R and the (r, θ) plane at $\phi{=}\pi/2$, in which the implants are embedded. We assume identical path loss for all the implants and the tissue channel has negligible signal reflection, scattering, or shadowing [85].

• **Implant-Implant channel:** The channel between a given muscle implant (m_i) and another peer implant (m_j) that communicates along the M-M path is specified by the gain gx_{ij}^{M-M}, and phase shift ψx_{ij}^{M-M} for a field $x \in [\overrightarrow{E}, \overrightarrow{H}]$. Here, $\overrightarrow{E}$ is the electric field and $\overrightarrow{H}$ is the magnetic field. The channel gain and phase are obtained as $gx_{ij}^{M\text{-}M}{=}f_1^{M-M}(||r_{ij}||, \theta_{ij})$ & $\psi x_{ij}^{M-M}{=}f_2^{M\text{-}M}(||r_{ij}||, \theta_{ij})$ where, θ_{ij} is the relative azimuth angle between m_i and m_j, and $||r_{ij}||$ is the separation between implants (m_i) and (m_j) through the M-M path estimated as $||r_{ij}||{=}\sqrt{r_i^2 + r_j^2 - 2r_i r cos(\theta_i - \theta_j)}$. The relative elevation angle $\phi_{ij}{=}0$ as the implants are assumed to be co-planar. Note the above formulation can be trivially extended for non co-planar muscle implants, though we leave out this case for space limitations.

• **Implant-Relay channel:** The channel between the implant (m_i) to relay R communication through the M-S path is given in terms of gain (gx_{iR}^{M-S}) and phase shift introduced by the tissue path through muscle-fat-skin interfaces (ψx_{iR}^{M-S}) for a field x, written as,

$$gx_{iR}^{M\text{-}S}{=}f_1^{M\text{-}S}(||r_{iR}||, \theta_{iR}, \phi_{iR}) \;\& \tag{6.1}$$

$$\psi x_{iR}^{M-S}{=}f_2^{M\text{-}S}(||r_{iR}||, \theta_{iR}, \phi_{iR}) \tag{6.2}$$

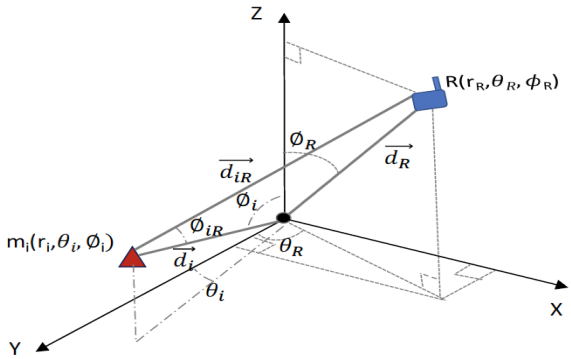

Figure 6.2: Spherical coordinate system with an implant and a relay

where θ_{iR} and ϕ_{iR} are angles defined similarly between m_i and R. $||r_{iR}||$ is the separation between implant (m_i) and relay through the M-S path estimated as $||r_{iR}|| = \sqrt{r_i^2 + r_R^2 - 2r_i r_R[A+B]}$, where A=$sin(\theta_i)sin(\theta_R)cos(\phi_i$-$\phi_R)$ and B=$cos(\theta_i)cos(\theta_R)$, and $P \in \{M-M, M-S, S-M\}$ is the path of the signal. The functions $f_1^{M\text{-}M}$, $f_2^{M\text{-}M}$, $f_1^{M\text{-}S}$ and $f_2^{M\text{-}S}$ are obtained using the channel models for $\overrightarrow{E}$ and $\overrightarrow{H}$ fields in [85].

6.4.2 Near-field signal propagation

Signals impinging on a receive antenna are typically assumed to have planar wavefront. This assumption is not valid in GC-IBN for the following reasons: First, GC-IBN uses the operating frequency of 100 kHz to 1 MHz, with a wavelength (λ) of $2E3$ to $3E3$ m. Second, the size of the electrodes used in implants range from few μm to mm. The far-field range of such small electrodes is given by $r \geq \frac{\lambda}{2\pi}$, i.e., $r \geq 3.1E2$ for 100 kHz and $4.7E2$ m for 1 MHz. However, the possible separation between the transmitter and receiver in GC-IBN can be at most 30 cm based on measurements in [85]. Beyond this range, the received SNR is too low for messages to be reliably decoded. Thus, GC-IBN communication is confined to the near-field range.

Having classified the GC-IBN communication as near-field, we proceed to explain the assumption of a spherical expansion of the electric field. The radiation pattern concept, usually referring to far-field communications, is borrowed to explain the near-field pattern of our electrodes in this case. Consider the electric field ($\overrightarrow{E}_i$) that

is proportional to the voltage (V_{in}) applied to the input electrodes that couple the GC signal to muscle. The magnetic field ($\overrightarrow{H}_i$) is proportional to the applied current (I_{in}) in the same implant m_i. The instantaneous $\overrightarrow{E}_i$ and $\overrightarrow{H}_i$ field strengths in the far field decrease inversely with distance (inverse-square law) and carry a relatively uniform wave-pattern, where the received signal is assumed to have constant frequency and infinite plane of constant phase and constant peak-to-peak amplitude normal to the phase velocity vector. These fields are also orthogonal to each other. As opposed to this, in the near-field, $\overrightarrow{E}_i$ and $\overrightarrow{H}_i$ field strengths falls exponentially with increasing distance from the source, contrary to the inverse-square law. Moreover, they can exist independent of each other with their field distributions depending on the tissue structure complexity without a strictly defined decreasing relationship. The electric and magnetic field components are assumed to expand spherically through the tissue.

6.4.3 Electric field pattern based on tissue orientation

The current coupled to the input electrodes of an implant is assumed to introduce a nearly isotropic radiation pattern in the surrounding tissue. However, higher conductivity along the longitudinal axis of the muscle tissue results from the continuous muscle strands that are oriented similarly. Coupled with the layered structure of such tissues in the transverse direction, the electrical field is $\approx \sqrt{2}$ times stronger in the longitudinal direction of the muscle tissue [86]. To incorporate this tissue anisotrophy, we model the spherical wave-front of electric field ($\overrightarrow{E}_i$) and magnetic field ($\overrightarrow{H}_i$) as follows.

$$\overrightarrow{E}_i = V_{in} \times \begin{cases} sin\left(\frac{\pi}{2} - \frac{\phi}{4}\right), & \forall\, \phi \in [0, \frac{\pi}{2}] \\ sin\left(\frac{\frac{\phi}{4} - \pi}{2}\right), & \forall\, \phi \in [\frac{\pi}{2}, \pi] \end{cases} \tag{6.3}$$

$$\overrightarrow{H}_i = I_{in} \times \begin{cases} 1.7 - sin\left(\frac{\theta}{2} + \frac{\pi}{4}\right), & \forall\, \theta \in [0, \pi] \\ 1.7 - sin\left(\frac{\theta - \pi}{2} + \frac{\pi}{4}\right), & \forall\, \theta \in [\pi, 2\pi] \end{cases} \tag{6.4}$$

For the instantaneous $\overrightarrow{E}_i$ and $\overrightarrow{H}_i$ fields emanating from m_i, the instantaneous energy flux density caused in the surrounding tissue is expressed as Poynting vector: $\overrightarrow{P}_i^T = \overrightarrow{E}_i \times \overrightarrow{H}_i$, where, the real part denotes the power flow and imaginary part represents the reactive near-field of antenna [96]. Equations 6.3 and 6.4 are derived based on the angles where the electric and magnetic field intensity is maximized. They are maximized in the longitudinal direction of the muscles. Equation 6.3, for example, shows the maximization of the energy in the direction of $\phi = 90^o$ from the electric field direction, which corresponds to the direction of the muscle layer (Fig. 6.11(b). Similarly, the energy is maximized in $\theta = 0^o$ and $\theta = 180^o$ directions for the magnetic field which also correspond to the longitudinal axis of the muscle layer (parallel to the skin) (Fig. 6.11(c)). The field pattern for the implant m_i during transmission is shown in Fig. 6.11(a).

6.4.4 Received signal at the relay without beamforming

The received near-field signal at R due to transmissions by source m_i can be determined by modeling the propagation behavior through tissue channel independently for $\overrightarrow{E}$ and $\overrightarrow{H}$ fields as

$$\overrightarrow{Pr}_i^R = \overrightarrow{E_i^R} \times \overrightarrow{H_i^R} \tag{6.5}$$

where $\overrightarrow{E_i^R} = \overrightarrow{E_i}.\ ge_{iR}^{M\text{-}S} e^{j\omega\left(\psi e_{iR}^{M\text{-}S} + \gamma e_{iR}^{M\text{-}S}\right)}$, $\omega/2\pi$ is the operating frequency and can be written as, $\overrightarrow{H_i^R} = \overrightarrow{H_i}.gh_{iR}^{M\text{-}S} e^{j\omega\left(\psi h_{iR}^{M\text{-}S} + \gamma h_{iR}^{M\text{-}S}\right)}$ and $\gamma_{iR}^{M\text{-}S}$ is the effect of drift in frequency and phase offset. We consider M co-planar implants transmitting simultaneously whose positions are uniformly distributed around the reference point with distribution $\frac{r_{max}}{\sqrt{2}}$. The ge and gh values for different tissue path are obtained from the HFSS based finite element simulation model in [85]. We define the term *array factor* as the net received signal pattern at the receiver resulting from multiple concurrent transmissions from the array of implants. For the $\overrightarrow{E}$ and $\overrightarrow{H}$ fields in the uniformly

distributed planar implant array, the respective array factors can be written as,

$$E[AF_E] = \frac{1}{M}\sum_{i=0}^{M-1} \overrightarrow{E_i} g e_{iR}^{M\text{-}S} e^{j\omega\left(\psi_{iR}^{M\text{-}S}+\gamma_{iR}^{M\text{-}S}\right)} \;\&\tag{6.6}$$

$$E[AF_H] = \frac{1}{M}\sum_{i=0}^{M-1} \overrightarrow{H_i} g h_{iR}^{M\text{-}S} e^{j\omega\left(\psi_{iR}^{M\text{-}S}+\gamma_{iR}^{M\text{-}S}\right)}\tag{6.7}$$

where $E(.)$ is the expected value, as the parameters are uniformly distributed values depending on the uniformly distributed position of the implants. Recall that the $\overrightarrow{E}$ and $\overrightarrow{H}$ fields are mutually independent. Hence, the array factor can be written as,

$$E[\overrightarrow{AF}] = E[\overrightarrow{AF}_E \times \overrightarrow{AF}_H]\tag{6.8}$$

The resulting received signal power at the relay, due to the array effect in (6.8), is oriented along the muscle fiber with less energy propagating towards the relay. This pattern is plotted in polar form (azhimuth and elevation planes) in Fig. 6.3(a)-(b) and the power for various number of implants is plotted in Fig. 6.11(a)-(c)) using spherical coordinates.

6.4.5 Increased received signal at relay with beamforming

As seen in the previous section, the collective energy transmitted by numerous implants is oriented along the muscle layer, instead of throught the fat and skin layer as required to reach the relay. For this reason, we propose a beamforming method using three weights to focus the signal energy to the relay. Meanwhile, we must ensure that the maximum received power at any point in tissue surrounding the transmitting implant array should be less than the maximum limit (P_S). Using the motivation from our experimental study in Sec.6.3, we aim to minimize the phase differences among the transmitting implants and lower per-node power requirements. Unlike far-field beamforming, we achieve a steering in the concentration of electric current to the

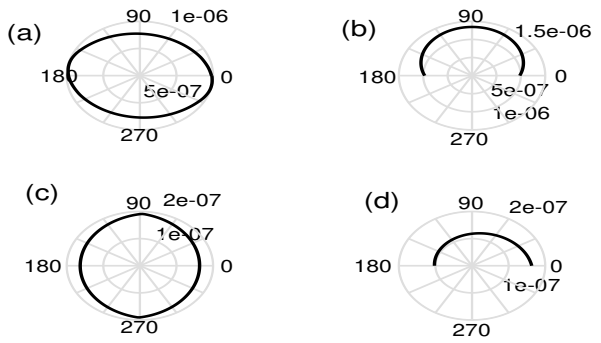

Figure 6.3: Directivity of received signal before (a,b) & after (c,d) beamforming

space needed instead of a clear "beam". We propose a conventional delay and sum beamforming method using three weights as explained below.

• **Safety weight (w^s):** Assuming the minimum required SNR for successful communication in the M-M and M-S paths to be $\delta^{M\text{-}M}$ and $\delta^{M\text{-}S}$, the minimum required transmission power by an implant (m_i) becomes:

$$P_i^{min} = \begin{cases} \dfrac{\delta_j^{M\text{-}M} N_o^j \triangle f_j}{g_{ij}^{M\text{-}M}} & \forall\, i,j \in \{1,..,M\} \\ \dfrac{\delta_R^{M\text{-}S} N_o^R \triangle f_R}{g_{iR}^{M\text{-}S}} & \forall\, i \in \{1,..,M\} \end{cases} \tag{6.9}$$

where N_o^j is the Gaussian noise P.S.D received at the receiver j with zero mean and variance σ^2=1e-8 $W/\sqrt{Hz}$, and $\triangle f_j$ is the receiver bandwidth. When the received power in the receiver exceeds the minimum requirement, the transmitting implant m_i can suitably reduce P_i to just meet the expected SNR threshold. The most suitable amount of transmitted power by an implant m_i to a receiver, be it either an implant or a relay, can be chosen as:

$$P_i = \frac{P_{ic}}{w_{ij}^s},\ \forall \in \{1,..,M\} + \{R\} \tag{6.10}$$

where $w_{ij}^s = \dfrac{\delta_{jc}^{M-x}}{\hat{\delta}_j^{M-x}}$, P_{ic} is the current transmit power, δ_{jc}^{M-x} is the current SNR, $\hat{\delta}_j^{M-x}$ is the expected SNR and $x \in [M, S]$.

Note that the maximum transmission power P_i^{max} is limited by the permitted level

of signal propagation through tissues as $P_i \leq P_S$. If there are multiple concurrent transmissions, then the cumulative signal at any point should also meet the safety criteria $\sum_{i=0}^{M-1} P_i \leq P_S$. Thus, for safe and energy efficient choice of transmit power, the safety weight is chosen as:

$$w_{ij}^{s} = max\left(\frac{\delta_{jc}^{M-x}}{\hat{\delta}_{j}^{M-x}}, \frac{\sum_{i=0}^{M-1} P_i}{P_S}\right), \tag{6.11}$$

$\forall i \in \{1,..,M\}$ & $\forall j \in \{1,..,M\} + \{R\}$. Using w_{ij}^{s}, the magnitude of P_i can be estimated using (6.10).

• **Phase-match weight (w_{ij}^{p}):** As seen in Fig. 6.11(c), the mismatch in phase among the signals results in destructive signal combination, and thus, reduces the net received power. To perfectly synchronize the uniformly distributed planar implant array, we first match the link-dependent phase shift of each implant obtained in (6.2) with respect to the reference position at (O). Then, using the good cross-correlation property of the Gold codes that we use later in Sec. 6.6, we extract the phase differences from the frequency offsets iteratively as $\gamma' h_{iR}^{M-S}$ and compute the overall phase lag of each implant in the form of Phase match weight as:

$$w_{ij}^{p} = \psi h_{iR}^{M-S} + \gamma' h_{iR}^{M-S} \tag{6.12}$$

• **Steering weight (w^{t}):** This weight allows steering the signal from the transmitter to the relay with the desired beam shape given in Fig. 6.3.(c)-(d). In the desired beam, along the elevation plane in Fig. 6.3.(d), the beam power is increased at ϕ=0 towards the position of the relay and in the azimuth plane in Fig. 6.3.(c), the propagation is steered away from the neighbors at θ=$0, \pi$. The corresponding steering weight is given as:

$$w_{iR}^{t} = sin(k\theta_{iR})cos(k\phi_{iR}) + sin(k\theta_{iR})sin(k\phi_{iR}) \tag{6.13}$$

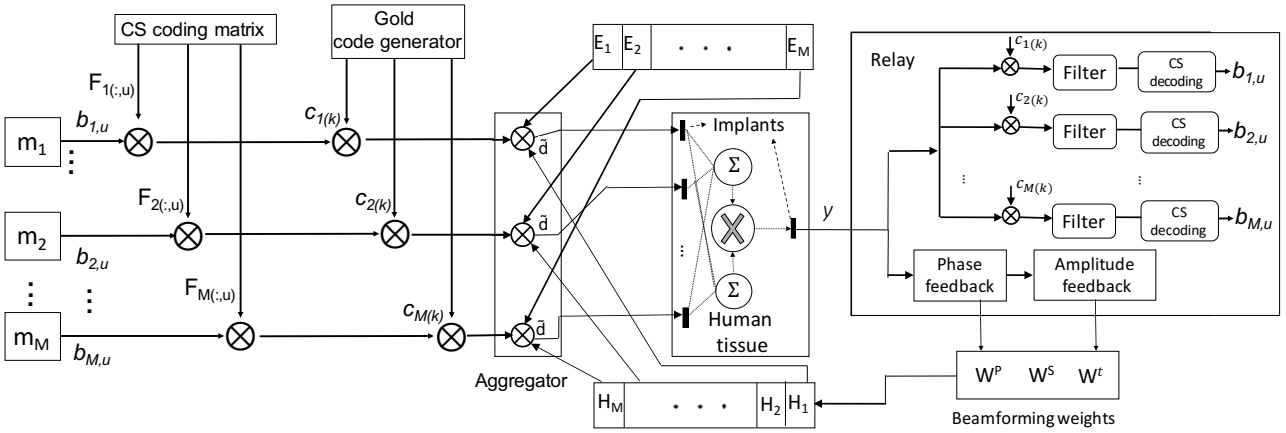

Figure 6.4: CDMA & beamforming based MAC framework for implants communication using GC-IBN

where, θ_{iR} and ϕ_{iR} are the respective relative azimuth and elevation angles, respectively, between the implant and relay (refer Fig.6.2), $k = \frac{2\pi f}{c'}$ is the wave number, c' is the propagation speed of signal through the tissue medium estimated using the permittivity of the medium as,

$$c' = c/\sqrt{\epsilon}\ m/s \tag{6.14}$$

where c is propagation speed of light in vacuum and ϵ is the permittivity of the medium. c' for muscle is around $9.5e6\ m/s$ and that of skin is around $8.3e6\ m/s$.

We adjust the array factor of the $\overrightarrow{H}$ field in (6.7) using the three weights derived above as,

$$E[AF_H]{=}\frac{1}{M}\sum_{i=0}^{M-1}\frac{1}{w_{iR}^{s}}\overrightarrow{H}_i g h_{iR}^{M\text{-}S} e^{j\omega\left(\psi_{iR}^{M\text{-}S}+\gamma_{iR}^{M\text{-}S}\right)} e^{w_{iR}^{t}-w_{iR}^{p}} \tag{6.15}$$

The average power pattern of the uniformly distributed planar array can be estimated as $E[|AF|] = |AF|(1-\frac{1}{M})+\frac{1}{M}$. We use our simulation environment to study the maximum power level in the tissue area using

$$P^{max} = max_{\{r,\theta,\phi\}} E[|AF|] \tag{6.16}$$

6.5 Hardware Implementation with Tissue Phantom

In this section we implement near-field beamforming developed in section 6.4. We describe the testbed and present the results that quantify the effects of beamforming.

6.5.1 Experimental Setup

We design a testbed using two USRP X310 software defined radios (SDRs), one each at the transmitter and receiver ends. Two distinct transmitters are installed on the same X310, since the SDR supports up to two LFTX daughter-boards. These low frequency daughterboards are set to 400 KHz center-frequency, which is within the range for galvanic coupling previously identified in [85]. Similarly, a LFRX daughterboard is used on the receiving X310. We implement near-field beamforming using the phase-match and steering weights analyzed and calculated in Sec. 6.4. The physical system layout and block diagram are given in Fig 6.5. We transmit QPSK modulated signals from two transmitters, A & B simultaneously, with limits on the transmit power to ensure it complies with the ICNIRP rules mentioned in Sec. 6.3. The SDRs are configured and programmed in MATLAB utilizing the wireless communications toolbox functions. In order to ensure that there is no ground coupling between the transmitters and the receiver, the receiver is connected to a battery source. All SDRs are given the same external clock inputs through the OctoClock, also from National Instruments, to ensure synchronization.

For the purpose of this testbed, the same data is generated and sent from the two transmitters to ensure a common bit-stream for beamforming. Each data set, after modulation, is multiplied by a phase offset to apply its beam weight and achieve constructive interference. The beam weights for each transmitter is calculated using equations 6.12 and 6.13. The weights are then summed together and applied to the

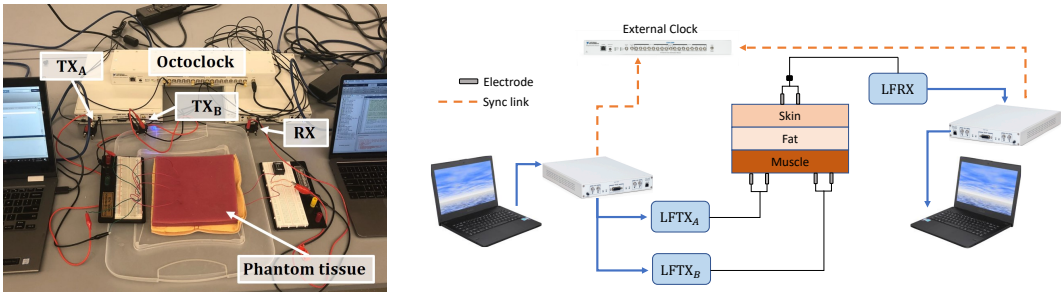

Figure 6.5: Photo and diagram of the testbed

transmitted signal as per (6.15). The phase match weight (w^p) is a sum of the phase offset induced by the channel and modeled in [85] and the frequency offset of the cross-layer path from muscle to fat to skin (M-S). Even though the entire system is connected on a common 10 MHz clock ensuring hardware frequency synchronization, we note there exists a constant frequency offset, possibly that of the cross-layer path. In our experimental setup we compensated for this effect in the receiver using a MATLAB coarse frequency compensator function. The steering weights (w^t) are calculated using the physical distances of the transmitters, from each other and from the receiver.

The transmitting electrodes are placed on the muscle layer. The beam-formed GC signal is received by the receiving electrodes that are placed on the skin layer, acting as the relay node. In the following subsection, we present the results of the received signal strength measurements and BER.

6.5.2 Experimental Results

There is an increase in received signal power when the two transmitters' weights are phase matched. As seen in Fig. 6.6, there is an increase of 3 dB in the received power when the two transmitters are in phase from the lowest received power achieved using TX A. This result matches the theoretical expected doubling in received power with two transmitters. We notice a 1 dB difference between the individual transmissions of the two TXs (A and B). This difference can be attributed in the different paths

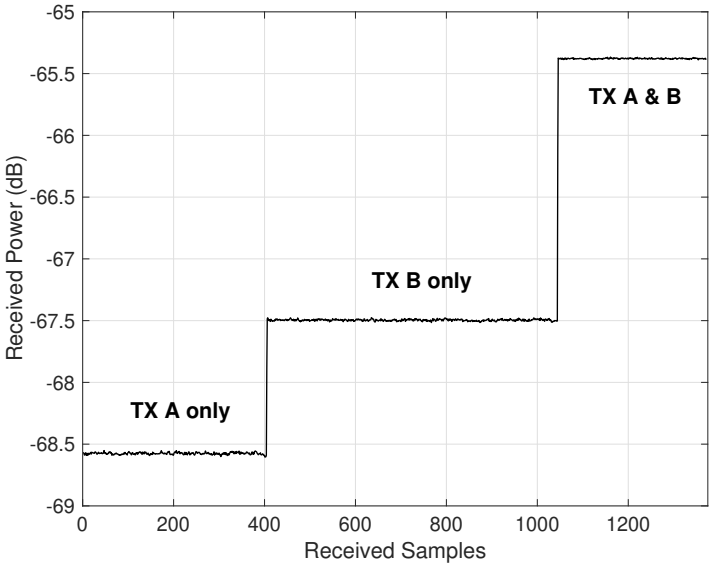

Figure 6.6: Received Signal Strength of three configurations (Tx A only, Tx B only and Tx A & B) with phase match weights

between each transmitter and the receiver pair.

The phase offset steering weights are calculated based on the position of the transmitters and receiver, thickness of tissue phantom, using (6.13). The steering weight is summed with the phase match weight and is introduced to the transmitter as a phase offset to TX B. However, during experimentation we discovered a range of phase offsets for which the highest received power did not change significantly (more than 0.4 dB). In order to investigate the effect of the phase offset on the received signal strength for a wide range of phase angles, we performed an angle sweep keeping the phase offset of TX A at 0° and varied the phase offset of TX B from 1° to 360°. As the results in Fig. 6.9 show, the maximum received power occurs at 87°, whereas for the same setup the theoretical optimal phase offset should be 62°, neglecting the frequency offset $\gamma' h_{iR}^{M-S}$ of equation (6.12). That offset is neglected because of the frequency compensation of our system. We notice that the received signal strength from 60° to 110° does not increase by more than 0.4 dB, ensuring that the constructive interference occurs for a range of approximately 50°. The destructive interference has its lowest point at 270°.

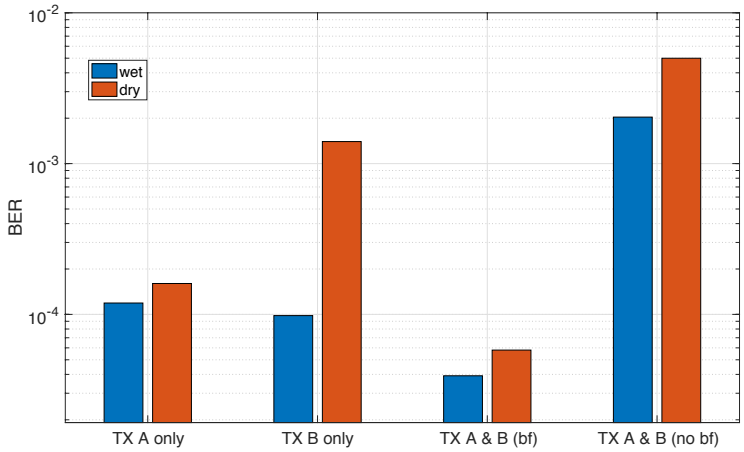

Figure 6.7: Average BER measurements for 4 configurations (Tx A only, Tx B only, Tx A and B with phase match weights, Tx A and B without phase match weights)

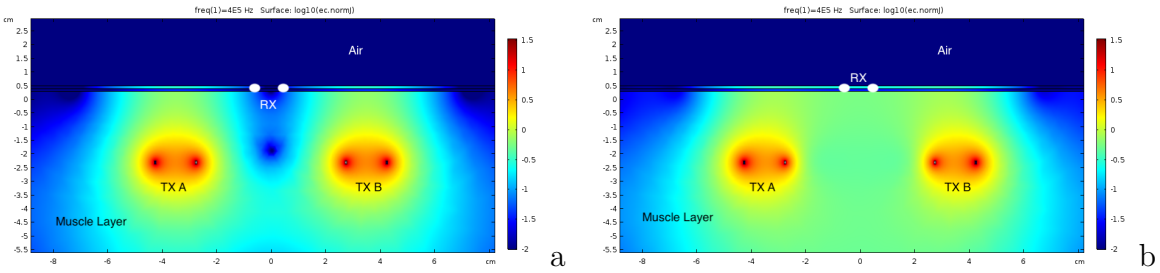

(a) Logarithmic current density without beamforming

(b) Logarithmic current density with beamforming

Figure 6.8: COMSOL® simulations for current density throughout phantom tissue

We also simulated the behavior of our setup using the finite element analysis COMSOL software, to measure current density at various points of the skin layer. As seen in Fig. 6.8, when the beamforming weights are applied to the two transmitters, there is higher current density at the receiver. These simulations prove that applying beamforming within our system effectively combines the power of several implants and increases the system efficiency.

Our testbed is designed to study intra-body communication as a whole, by providing insights on the communications front of implanted sensors transmitting measurements to a receiving on-skin relay. For this reason, the decoding capabilities of the system are of great interest. With an increase in received signal strength, and therefore SNR, the BER of the system when beamforming is enabled is lower than

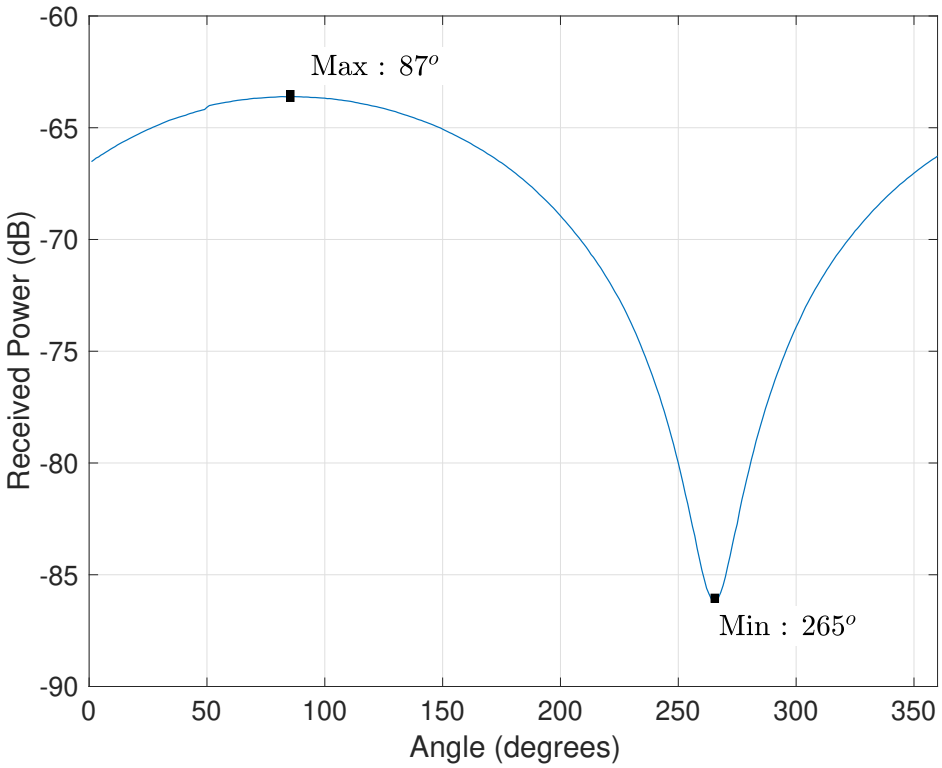

Figure 6.9: Received Signal Strength with two transmitters, changing the angle of Tx B from 0-360 degrees

that of individual transmissions. As seen in Fig. 6.7, the BER of the system when both transmitters are transmitting with beamforming falls in the order of 4e-4, compared to 2e-3 for the scenario with no beamforming. This proves that an implant network where multiple sensors transmit with matched phases resulting in constructive beamforming results in a system with better decoding capabilities. We performed experiments for both wet and dry conditions and it can be seen that the wet conditions lead to a lower BER overall since the received signal strength improves through wet tissue. The received signal strength of our system does not exceed 0.31 μW, which is below the mW range provided in [87], while we also monitor the TX power to ensure safe transmissions.

6.6 Beamforming using joint Compressive Sensing-CDMA

Implants participating in distributed beamforming fashion must transmit a common data vector to the on-skin relay. We propose a CDMA procedure to share data among the implants before initiating the beamforming process. Specifically, we develop a compressive sensing (CS) transmission technique to reduce the number of measurements to send, which further results in lowering the transmission time and energy. The beam formation and the process of end-to-end data communication is split into five stages, as described below (see Fig. 6.10):

• **Stage I. Resource assignment by the relay:** Each communication cycle starts a parameter setting beacon by the relay that allows implants to synchronize, set duty cycles for peerlevel and beamforming-based communication, use CDMA codes to partition the collision domain, and compute feedback weights for the array factor given in (11), (12) and (13) for optimal beamshaping (refer to stage.1 in Fig.10). Communication from implants are acknowledged in a successive round, enabling the implants to sleep immediately after they transmit the beam. Specifically, the parameters setting includes a synchronization message that delivers the information about two synchronization time slots. In the first time slot window the implants are allowed to send their data to a peer aggregator, while during the second time slot all the implants listen for the collected data that the aggregator is sending back to them. At the end of the second time slot, each implant sends such common data to the relay on the surface acting as distributed beamforming. Such procedure is required since we need each implant to have a common data vector prior to beamforming, thus the relay also appoints an aggregator (IDA) for the communication round. The aggregator's role is simply to collect the individual and simultaneously transmitted spreaded sequences that combine in the tissue channel, and save this as the common data vec-

tor. The aggregator is a peer-implant, and its role is rotated in every round. Note that only a coarse synchronization is required during peer communication phase as specified at Stage III: an implant can choose to transmit anytime within the allowed window. For this purpose, quasi-orthogonal CDMA Gold codes are chosen for their good performance in an asynchronous CDMA transmissions.

Specifically, a joint CS-CDMA scheme is proposed where the Gold codes are multiplied by the CS coding matrix. This way, the implants send less samples of data to further save energy while exploiting the possibility of fast simultaneous transmissions. Both the decoding and decompression of data are performed only at the on-skin relay, so that the implants do not have to perform any complex tasks.

• **Stage II. CS downsampling of data transmission:** CS theory allows to reconstruct a signal with much lower samples than its dimension, provided that signal is sparse in some basis [97] and restricted isometric property (RIP) is satisfied [31] [98]. Following this reasoning, implants may send a lower amount of sensed data reducing the energy consumption, one of the main concern in intra-body networks.

In practical applications, implants may not transmit data continuously. Hence, we assume that the sensed data is sparse, i.e., the implant activity is sporadic and i.i.d with probability $p_a \ll 1$ in the considered time window. Thus, the sensed data $\mathbf{b}_i$ of size $U \times 1$ at implant m_i may be represented as a linear measurement $\mathbf{x}_i$ of size $N \times 1$ with $N \ll U$ as

$$\mathbf{x}_i = \mathbf{F}_i \mathbf{b}_i \tag{6.17}$$

that corresponds to CS coding matrix multiplication block in the left side of Fig. 6.4, where measurement vector $\mathbf{x}_i$ is a compressed version of $\mathbf{b}_i$ obtained through the CS coding matrix $\mathbf{F}_i$, i. e., the dictionary, with

$$\mathbf{F}_i = \mathbf{Q}_i \tilde{\mathbf{F}}_i \tag{6.18}$$

where the elements of $\tilde{\mathbf{F}}_i$ are taken from Rademacher distribution and $\mathbf{Q}_i$ is the discrete Fourier transform (DFT) matrix. Note that $\mathbf{b}_i \in \mathcal{B}_a$, where $\mathcal{B}_a$ is the discrete alphabet $\mathcal{B}$ augmented to represent also the inactivity. Specifically, an inactive implant is equivalent to transmit symbol 0 while activity corresponds to data modulated according to the alphabet $\mathcal{B}$ [38].

The size of the compressed data $\mathbf{x}_i$ that implant m_i shares through the CDMA procedure is much lower than the original $\mathbf{b}_i$. Moreover, since the transmission for some health applications is sporadic and also short, we can interpret it as group sporadic transmission, which allows to develop a faster CS algorithm as detailed in Stage V.

• **Stage III. Peer communication phase:** The relay provides a time window (T_B) for all implants to combine their data using the Gold codes and transmit them simultaneously. Note that an implant can opt out of transmission in a cycle and sleep for prolonged period if its sensing cycle is longer. Also, the communication is not strictly synchronized that relieves the implants from complex scheduling and mutual phase offset computation for this first round of messaging. An implant can choose to transmit anytime between the allowed window of peer-level communication. This transmission is intentionally set to very low power given that it traverses the high-gain M-M path to the aggregator node (refer to stage.2 in Fig.6.10).The spreading factor L of the Gold code is chosen based on the number of implants. The implant ID is associated with a unique spreading code sequence $\mathbf{c}_i$ within the CDMA codebook.

For N compressed data bits $\mathbf{x}_i$ of the implant i, each bit is directly multiplied by the Gold code $\mathbf{c}_i$ with L elements to generate the spread sequence $x_{i,n}\mathbf{c}_i,\ \forall\ i \in \{1,..,M\},\ n \in \{1,..,N\}$ of size $L \times 1$ (refer to the Gold code generator multiplication in Fig. 6.4). These quasi-orthogonal Gold codes have good cross correlation properties that enable simultaneous almost non-interfering transmissions. After spreading at the sampling time instant corresponding to the index $k,\ \forall k \in \{0,..,L-1\}$, the implants transmit the spreaded sequence $x_i\mathbf{c}_i$ through the M-M path. At this stage, neither

other implants nor the aggregator performs any decoding.

At n-th bit time instant, the aggregator receives the sequence $\mathbf{d}_n$ as a vector of size $L \times 1$ from the $M-1$ implants as,

$$\mathbf{d}_n = \sum_{i=1}^{M-1} g_{iA}^{(M-M)} x_{i,n} \mathbf{c}_i + \mathbf{w} \tag{6.19}$$

where A represents the aggregator, $x_{i,n}$ is the n-th bit sent by the implant m_i after applying CS, $\mathbf{c}_i = [c_i(0), c_i(1), ..., c_i(L-1)]^T$ is the spreading code for implant m_i with $x_{i,n}\mathbf{c}_i$ expressed in antipodal form, $()^T$ denotes the transpose, and $\mathbf{w}$ is the iid additive white Gaussian noise vector with zero mean and variance σ^2 of size $L \times 1$ given by $[w(k-L+1), w(k-L+2), ..., w(k)]^T$. Since each implant transmits in a narrow band channel (400 kHz) the M-M channel can be represented as a single tap channel [85]. We assume that $g_{ij}^{(M-M)}$ is constant during a transmission cycle.

The final vector $\mathbf{d}$ of size $LN \times 1$ is given by

$$\mathbf{d} = [\mathbf{d}_1 \;\; \mathbf{d}_2 \;\; ... \;\; \mathbf{d}_n \;\; ... \;\; \mathbf{d}_N] \tag{6.20}$$

Eq. (6.17)-(6.20) summarize the joint CS-CDMA procedure for data transmission, showing that the sent data $\mathbf{d}$ is given by the original bits $\mathbf{b}_i$ for each implant m_i in (6.17) multiplied by a combination of CS coding matrix $\mathbf{F}_i$ and Gold codes $\mathbf{c}_i$.

Once the aggregator receives the overall CDMA vector containing the spread data $\mathbf{d}$, it sends back the common CDMA vector $\mathbf{d}$ representing the aggregated value to the peer implants through a single broadcast, again using the high-gain M-M path.

The spread data received back at the m_i-th implant can be expressed as

$$\tilde{\mathbf{d}}_i = g_{Ai}^{(M-M)} \mathbf{d} + \mathbf{w} \tag{6.21}$$

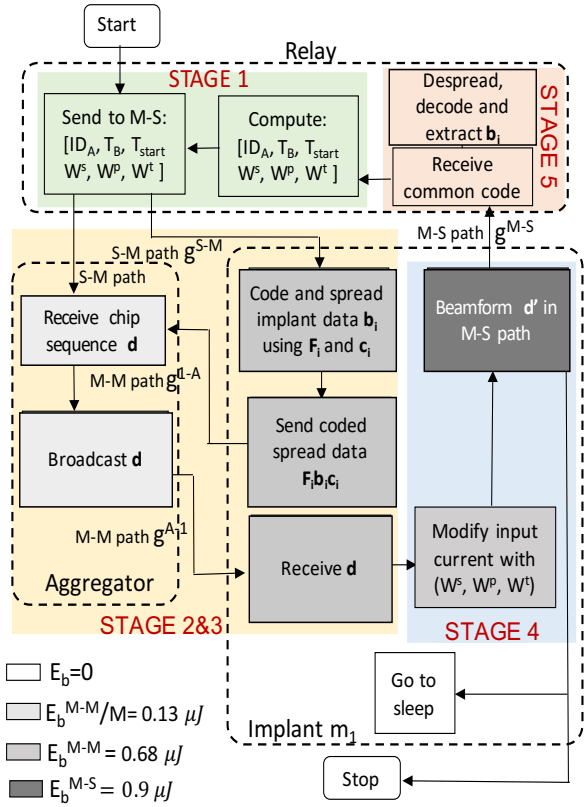

Figure 6.10: Stages showing the entire end-to-end implant to relay communication

Now, all the implants have the common CDMA vector (refer to $\tilde{\mathbf{d}}$ in Fig. 6.4), which may only slightly differ from each other depending on the channel coefficient of the M-M path from the aggregator to the specific implant according to (6.21).

- **Stage IV. M-S Beamforming phase:** In this phase, each implant acts as an independent antenna array element and attempts to form a beam sending the same overall CDMA data vector that has been shared with all the implants at the instant T_B predetermined by relay. The use of the same CDMA data during beamforming further improves the SNR and lowers the required M-S transmission power at the implants as shown in Sec.6.4. Although each implant acts as an element of a virtual antenna array sending the same information, the individual implant signals differ in amplitude and phase, as instructed by the beamforming weights. The implants tune their transmission based on the weights, such that all the transmissions from implants constructively amplify the received signal $\mathbf{y}$ at the relay and maximize the received

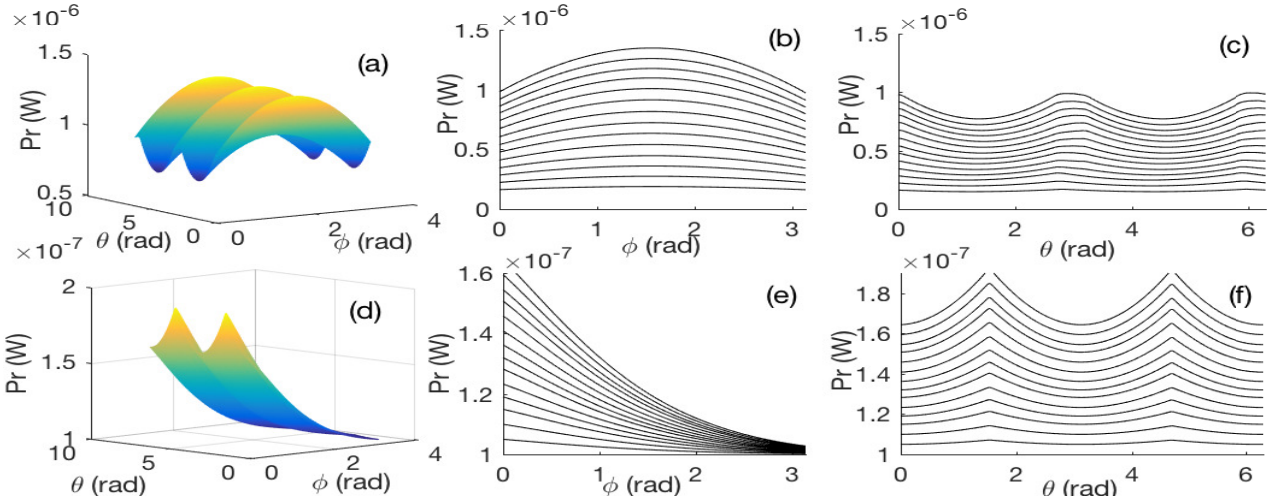

Figure 6.11: Received power before and after beamforming

power.

Thus, each implant sends the information at lower power compared to individual transmissions in the M-S channel, enabling significant energy savings.The received vector $\mathbf{y}$ at the relay (as shown in Fig. 6.4) is given by

$$\mathbf{y} = \sum_{i=0}^{M-1} S_i \tilde{\mathbf{d}}_i + \mathbf{w} \tag{6.22}$$

where $S_i = \frac{1}{w_{iR}^s M} g h_{iR}^{M\text{-}S} e^{j\omega\left(\psi_{iR}^{M\text{-}S} + \gamma_{iR}^{M\text{-}S}\right)} e^{w_{iR}^t - w_{iR}^p}$ obtained from (6.15) that accounts for both the steering coefficient of the implant m_i and the channel coefficient of the M-S path from the implant implant m_i to the relay R on surface. The implants enter into the sleep state immediately after sending the beam until the next transmission cycle (see stage.3 in Fig. 6.10).

• **Stage V. Despreading, decoding and feedback at the relay:**

Having received the common CDMA vector through the beamformed signal, the relay performs despreading and CS data reconstruction using a matrix with the same Gold codes distributed to the individual implants and the CS coding matrices. In this way, it recovers the sensed data and the associated ID of each implant, as shown in the Relay block in Fig. 6.4.

Going in more details, CS methods can be categorized broadly into accurate and stable convex relaxation iterative algorithms [33], [30], and fast but less accurate greedy algorithms [47], [48]. Since health applications require high reliability we focus on an accurate iterative solution. Specifically, as said before, in such applications the implant activity may be interpreted as group sporadic, thus we develop a group basic pursuit denoising (Group-BPDN) approach to reconstruct the sent data $\mathbf{b}_i$. The problem may be expressed as [99]

$$\min \sum_{v=1}^{V} \|\mathbf{b}_{i,v}\|_2 \text{ subject to } \|\mathbf{F}_i\mathbf{b}_i - \hat{\mathbf{x}}_i\|_2 \leq \sigma \tag{6.23}$$

where the index v refers to the group to which the data have been assigned, $\mathbf{F}_i$, $\mathbf{b}_i$, $\mathbf{x}_i$ are defined in (6.17), and σ is the noise variance. The estimate $\hat{\mathbf{x}}_i = [\hat{x}_{i,1} \ \hat{x}_{i,2} \ \ldots \ \hat{x}_{i,n} \ \ldots \ \hat{x}_{i,N}]$ of size $N \times 1$ is obtained through the CDMA despreading that uses the cross-correlation of the received signal $\mathbf{y}$ in (6.22) with the known Gold codes. Specifically, the element $\hat{x}_{i,n}$ of $\hat{\mathbf{x}}_i$ is calculated as

$$\hat{x}_{i,n} = \mathbf{y}_n^T \mathbf{c}_i \tag{6.24}$$

where $\mathbf{y}_n$ is the $L \times 1$ element of the $LN \times 1$ vector $\mathbf{y} = [\mathbf{y}_1 \ \mathbf{y}_2 \ \ldots \ \mathbf{y}_n \ \ldots \ \mathbf{y}_N]$ and $()^T$ indicates the transpose.

Note that the Group-BPDN minimizes quadratic noise by solving the convex optimization problem as a quadratic programming approach for which efficient Interior-Point (IP) methods exist [99].

In terms of transmission and propagation time, the whole transmission cycle takes

$$4\frac{L}{\eta} + 2\frac{\psi x_{iR}^{M\text{-}M} + \gamma x_{iR}^{M\text{-}M}}{360f} + 2\frac{\psi x_{iR}^{M\text{-}S} + \gamma x_{iR}^{M-S}}{360f} + 4T_R \tag{6.25}$$

seconds, where L is the frame (or chip) length and T_R is the tissue relaxation time required between transmissions to assure normal tissue temperature under abnormal blood flow rates, calculated as $T_R = \sqrt{\frac{\epsilon}{\sigma}}$, ϵ & σ being the tissue permittivity and conductivity.

Finally the relay computes the weights w_{iR}^s,w_{iR}^p and w_{iR}^t using (6.11), (6.12) and (6.13) for the successive transmission and transmits them to the implants at the predetermined interval as given in the Beamforming weights block in Fig. 6.4 and in stage.1 in Fig. 6.10.

6.7 Performance Evaluation & Results

In this section, we evaluate the energy savings achieved by the proposed CDMA based beamforming framework by (i) analyzing the proportion of energy propagating in the direction of the relay to that leaking in the undesired directions, (ii) studying the influence of the number of array elements on the implant power consumption, (iii) quantitatively measuring the improvement in implant lifetime, and (iv) comparing the energy consumption for the overall M-S path communication with/without our approach. We develop a 3-D multi-layer, heterogeneous tissue channel model in MATLAB, operating at a narrow band of 100 kHz. The tissue area has the dimension of 20×20cm, with r_{max}=20 cm. The separation between the layer of implants in muscle and the surface is 2.2 cm. The maximum safe transmit power is 1 mW.

6.7.1 Effectiveness of beamforming

The pattern of received power at the relay resulting from the sum of the signals concurrently propagating through the tissue medium without beamforming is shown in Fig. 6.11(a)-(c). Here, the propagation is oriented towards the longitudinal muscle direction (at ϕ=$\frac{\pi}{2}$, θ=$0, \pi$), where more energy flow occurs along the length of the

arm. This causes minimal flux at the surface relay (at transverse direction at ϕ=0). This pattern may also cause more interference to the potentially neighboring implants (refer Fig. 6.1(left) for the direction of neighbors). Before beamforming, the ratio of energy flow in the required direction to undesired direction is ≈ 0.53. Fig. 6.11(d)-(f) shows the received signal at relay after beamforming, where more power is steered towards the relay (at ϕ=0) and there is less power in the longitudinal direction (ϕ=$\frac{\pi}{2}$, $\theta = 0, \pi$) mitigating the interference to neighbors.

Fig. 6.11(b)-(c) shows power degradation when signals with different phases are combined together. After the phase mismatch is rectified using W^p in the beamforming process, the signals add up constructively (refer Fig. 6.11(e)-(f)) as demonstrated in Fig. 6.1(d) and improve the received power by an additional $\approx 3\%$ as shown in Table.6.2 as $Pr(W^p)$. Note that this is the received power obtained after the transmit power is reduced to sufficient level using w^s weight. We analyze the maximum induced power at every point in the given tissue area defined by θ, ϕ and r using (6.16) and verify that the cumulative received power at any point in the tissue with multiple concurrent transmissions does not exceed the restrictions posed by safety limits, confirming the tissue safety and normal thermal distributions [87]. Using the simulation environment, we further ensure that $\int_\theta \int_\phi \int_r Prdrd\phi d\theta \leq 25\ \frac{mA}{m^2}$.

Influence of number of implants: The resulting proportion of power in the re-

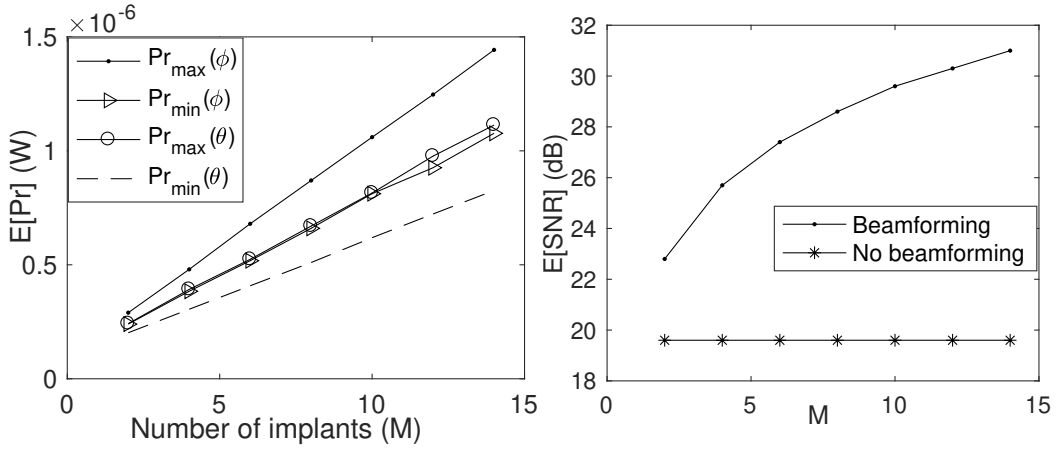

Figure 6.12: (a) Directionality (b) SNR before & after beamforming

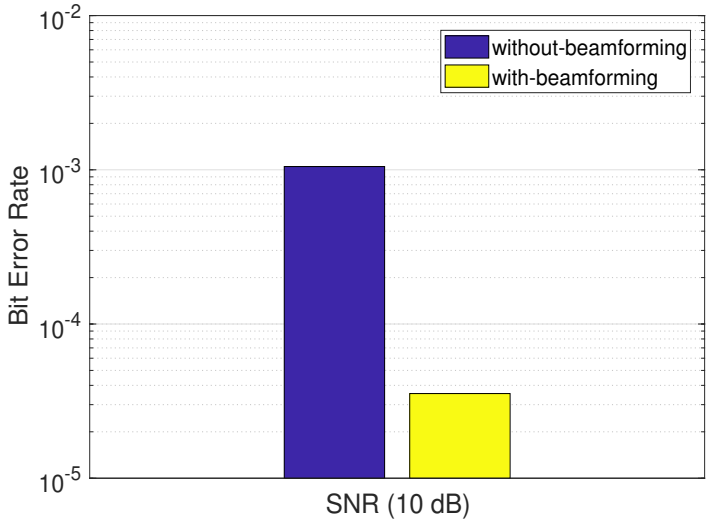

Figure 6.13: Bit error rate for CS-CDMA solution based on Group-BPDN and Gold codes with and without beamforming. Spreading sequence $L = 128$ chips, sparsity $= 40\%$, maximum delay $= 2$ chip time duration, number of implants $M = 2$, data length $U = 5000$, compressed measurements $N = 2500$.

quired to undesired direction is plotted in Fig. 6.12.(a) illustrating that more power is steered towards the relay when there are more number of implants forming the array. Thus both the critical beamforming parameters namely, the per implant power conservation and the directivity of beamforming, are improved with the number of implants or array elements (M). The actual SNR for individual transmission from each implant through M-S path is compared with the exponential increase in SNR at the receiver after beamforming with M implants in Fig. 6.12(b).

Implant lifetime: The transmission power of the implants is reduced to just meet the required SNR by applying the safe weight w^s derived in (6.11). The resulting power consumed (aPt) in each implant vs M and the corresponding improvement in implant lifetime is shown in Table.6.2. We see that the implant life dramatically extends from 10 weeks when used without beamforming, to $\approx$ 138 weeks with beamforming for the scenario with 14 implants.

6.7.2 BER & energy analysis for CS-CDMA beamforming

The proposed CS-CDMA scheme allows concurrent transmissions for the implants which reduces the total time for data transmission. The implants perform only simple tasks to send the acquired data, while the burden despreading/decoding is carried out only at on-skin relay. Moreover, the CS procedure allows to further reduce the transmission time since a much lower number of samples are sent instead of the full senses data. There is, however, an additional overhead of (i) spreading the data using the Gold codes, and (ii) (albeit high gain M-M) communication between implants to the aggregator and back. We aim to study whether this cost is offset by the energy savings achieved by beamforming.

The proposed algorithm for asynchronous CS-CDMA recovers both the activity of the implants and their data in a certain time window. The total number of sensors varies between 2 and 10. The spreading factor L for the Gold codes is set equal to 128 and the Group BPDN CS approach is used to recover data with different level of sparsity, which corresponds to the percentage of implant's activity in a certain time window.

Fig. 6.13 shows a comparison between the BER achieved by the proposed CS-CDMA solution with and without beamforming under the same parameter setting of the experimental setup in Sec. 6.5. Specifically two implants are considered and the BER improvement is due to SNR gain (2.5 dB) obtained when using beamforming.

The simulation results on Fig. 6.14a compare the achieved BER for different number of implants, describing that the system shows good performance with an increased number of implants. Fig. 6.14b illustrates the BER performance versus the maximum delay among the implant's transmissions. Each implant transmits with a random delay within the maximum one to simulate the asynchronous scheme in the peer communication phase inside the muscle. In low E_b/N_0 region the performance for different delays is comparable, while lower delays give better results when increasing

E_b/N_0.

Fig. 6.15 focuses on the choice of the dictionary matrix $\mathbf{F}_i$ in (6.18) for the proposed CS-CDMA algorithm. Indeed, the design of such matrix is one of the main concern in CS algorithms for an efficient solution. We compare the proposed $\mathbf{F}_i$ definition, based on DFT and rademacher distribution, with only DFT, and Gaussian and Bernoulli random matrix. The total amount of measurements has been fixed to 5000 and results in Fig. 6.15 prove that the proposed solution shows high performance even when sending only 50% measurements, differently from DFT, Gaussian and Bernoulli matrices.

Fig. 6.16 compares the accuracy of the proposed CS-CDMA solution, based on Group-BPDN CS approach, with a modified version of it, i.e., when employing the greedy regularized group orthogonal matching pursuit (ReGOMP) algorithm. Fig. 6.16 shows that the proposed Group-BPDN based approach outperforms the Re-GOMP solution for both values of sparsity (20% and 40%), showing high accuracy already when sending only 50% measurements. Note that for health applications the high accuracy is a stringent requirement.

Network traffic and time: With the proposed framework with L=64, the total traffic flow in a transmission cycle becomes 32 bytes, which is much lower than the existing IEEE 802.15.6 standard that requires a minimum of 13×4 bytes as frame header alone not including the data. The time required for the whole transmission cycle is estimated using (6.25) for T_R=10 μs and η=100 $kbps$ to be only 1.3 ms that is mainly dominated by the transmission time.

With and without beamforming: We next compare the energy consumption for the implant to relay communication through the M-S path with and without the beamforming. For an expected link length of 5 cm, the average M-S path-loss is 41.2 dB. The energy per bit required for a desired SNR of $\hat{\delta}$ is given using (6.9) by E_b=P_i^{min}/η. For $\hat{\delta}$=10, a noise factor (N_o) of 1e-8, data rate η of 10 $kbps$ and

bandwidth $\triangle f$ being $1e5\ Hz$, the required energy per bit (E_b) becomes 6.62 μJ. This would allow battery of capacity of 240 mAh to last for 2.89 years.

Before beamforming, the implants first broadcast their individual codewords in the M-M path. This step requires an energy of 0.68 μJ, considering the same values as assumed above for all other parameters, other than the lower path loss through M-M path (19 dB). The aggregated codeword is then transmitted from the aggregator as a broadcast to all implants that requires $\approx 0.7\mu J$. Finally, the beamforming towards the relay in undertaken in the M-S path, where each node spends about $4e\text{-}5M^{-1.03}$ times less energy than that actually required for the direct M-S path. For a scenario with 4 implants, the power consumption in each implants for the complete transmission cycle is 1.39 μJ, which is 4.7 times lower than that required for M-S communication without beamforming. The proposed framework extends the life of implant upto 13.8 years assuming every other parameter remains the same.

6.8 Conclusion

In this work, we propose and implement an energy efficient implant to surface relay communication using galvanic coupling and beamforming. The technique is strongly focused on improving energy efficiency by: sharing sensed updates among peer-implants using compressed sending CDMA through the high-gain M-M path, avoiding unpredictable data delivery conditions caused by collisions and transmission back-offs. Then, through near-field beamforming performed by the implants organized into distributed transmitter arrays, communication through the vertical tissue layers is achieved with high SNR. Our system dramatically lowers the energy required for end-to-end implant to relay communication that is 79% more energy efficient than the direct case, and extends the lifetime of implants upto 13 years, while ensuring accurate, low BER communication.

Table 6.1: Variable definitions and ranges

Variables	Definitions
M, R & m_i	Total number of nodes, Relay & Implant i
M-M, M-S, S-M	Paths: Muscle-muscle, muscle-skin, Skin-muscle
$\overrightarrow{H}$, $\overrightarrow{E}$	Instantaneous magnetic and electric fields
θ_i, ϕ_i	Azimuth and elevation angles
r_i	Distance between 2 points in spherical coordinates
AF	Array factor
g^p	Gain in path p; ge - $\overrightarrow{E}$ gain; gh - $\overrightarrow{H}$ gain
ψ, γ	Phase shift and Frequency offset
$f, w, \triangle f$	Frequency, angular frequency and bandwidth
c&c'	Speed of EM signals in vacuum and tissue
w^s, w^p, w^t	Weights for safety, phase match & steering
c_{ik} & $b_{i,n}$	k^{th} bit of Walsh code for m_i & n^{th} bit of m_i
η_m	Required data rate for m_i, $\forall i \in \{1, .., M\}$
P_i	Transmit power consumed in m_i, $\forall i \in \{1, .., M\}$
Pr^R & P^S	Received power in R & Safe transmit power
$\delta^{M\text{-}S}, \delta^{M\text{-}M}$ & σ	SNR in path M-S and M-M & Noise variance
N_o	Gaussian distributed noise P.S.D $\in (0, \sigma^2)$

Table 6.2: Power consumption for 1 bit with $E[P] = 0.5mW$

M	Pr (μW)	$Pr(W^p)$ (μW)	aPt (mW)	Life (weeks)
1	0.9	0.92	0.5	10
2	1.9	1.93	0.23	21
4	3.67	3.71	0.12	40
6	5.37	5.49	.085	59.5
10	8.94	9.11	0.05	98.8
14	12.4	12.7	0.03	137.9

Table 6.3: Conductivity and relative permittivity of three layers of phantom tissue [93]

	Conductivity[S/M]	Relative Permittivity
Skin	0.0030479	1076.3
Fat	0.024769	38.134
Muscle	0.42782	4339.3

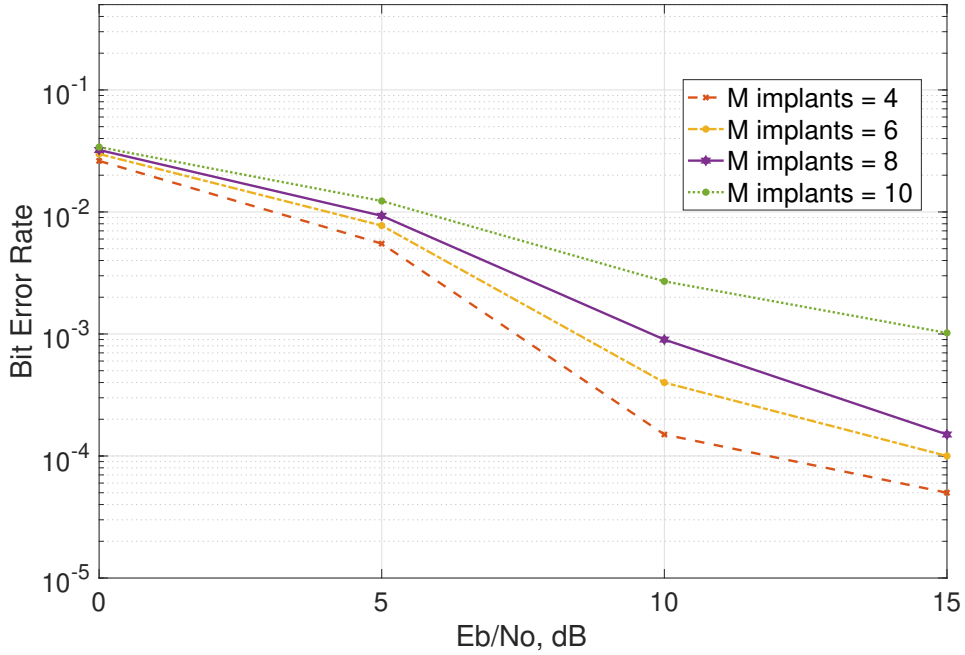

(a) BER for CS-CDMA solution based on Group-BPDN and Gold codes, maximum delay = 2 chip time duration

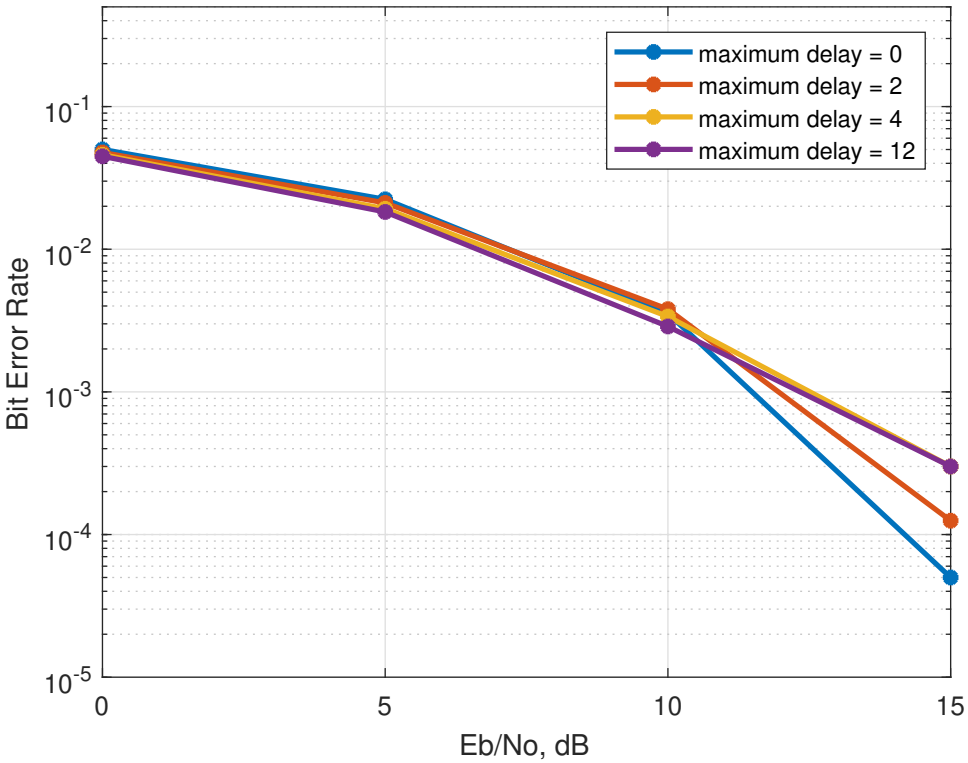

(b) BER for CS-CDMA solution varying the max. delay (# of chips) among implants' transmissions of the asynchronous scheme

Figure 6.14: BER of CS-CDMA. Spreading sequence $L = 128$ chips, sparsity = 40%, data length $U = 5000$, compressed measurements $N = 2500$

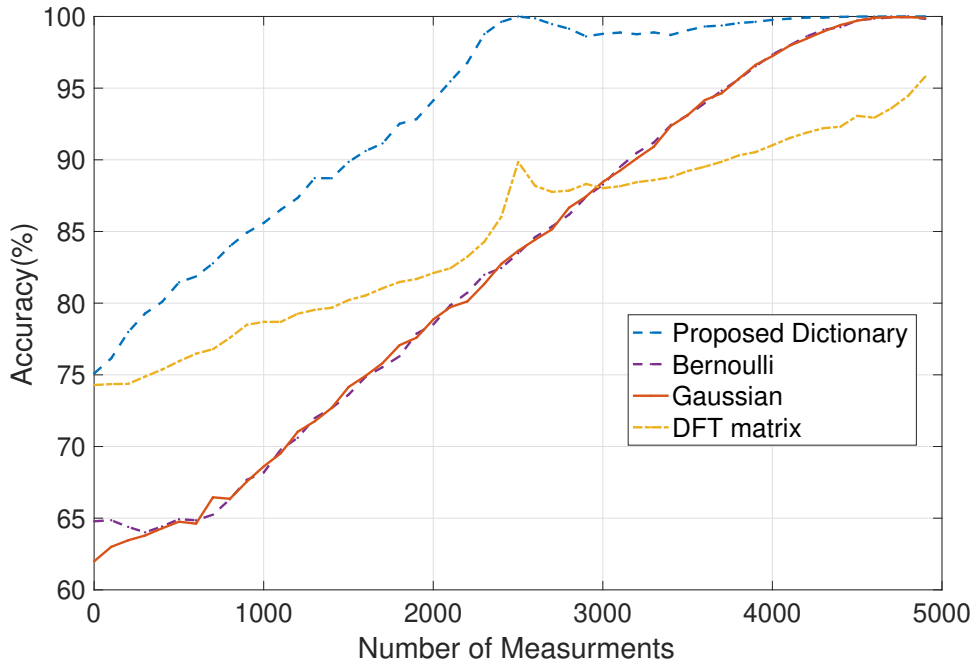

Figure 6.15: Accuracy of the proposed CS-CDMA algorithm for different CS coding matrices.

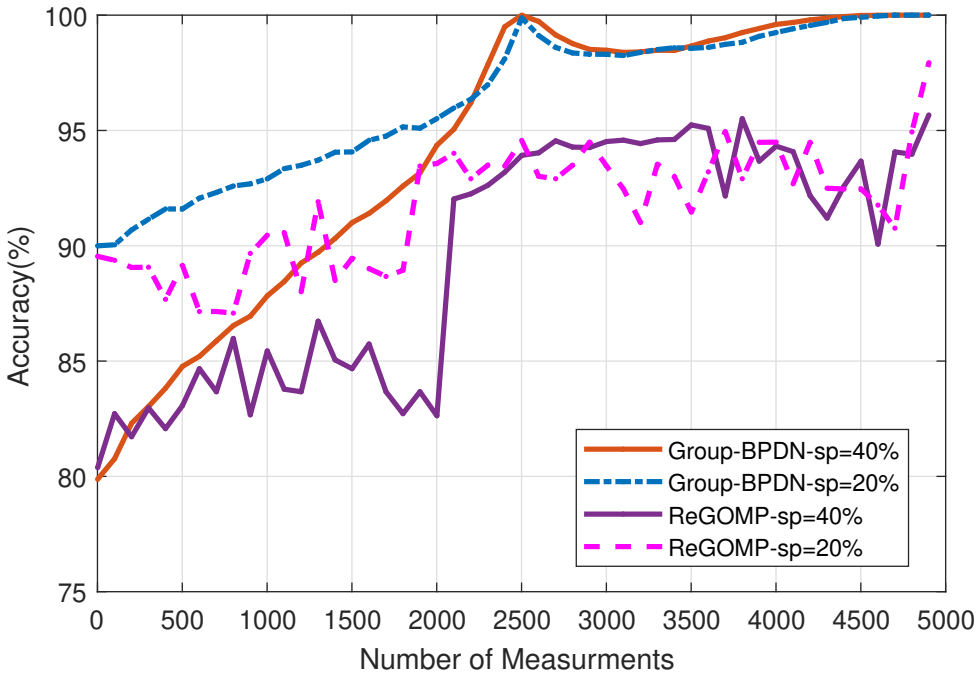

Figure 6.16: Comparison betweeen the proposed CS-CDMA scheme based on Group-BPDN and its modified version using ReGOMP. Maximum delay = 2 chip time duration, sparsity (sp) = 20% and = 40%.

7

Galvanic coupling Test-Bed for IBC links

7.1 Introduction

Implanted sensors will enable the next generation of healthcare by in-situ testing of abnormal physiological conditions, personalized medicine and proactive drug delivery. The paradigm of interconnecting the implants is known as intra-body network (IBN) and allows implants to transmit measurements to an external processing center for real time monitoring, to receive updates on drug delivery volumes, and to directly start actions by embedded actuators. All these examples require energy efficient data communication between implants through body tissues.

However, the state of the art (SoA) for intra-body communication (IBC) relies on high frequency radio (RF) signals. Short-range RF communication techniques, such

as Bluetooth, ANT, and Zigbee [100] are useless for intra-body communication as they are affected by severe attenuation within the human tissues, which are composed of 40-60% water, high power consumption, and limited battery lifetime. Moreover, emitted RF signals propagates also around the body, creating privacy risks.

Non-RF IBC techniques

Non-RF techniques that use the human body as a medium for data communication include ultrasound (US) technology, which consists of mechanical vibrations and works well in mediums with high water content such as the body [101]. The main US drawbacks are severe multi-path fading and the high delay caused by slow propagation speeds. Another alternative to RF is inductive coupling (IC) [102]: coils wrapped around anatomy are used to generate and receive magnetic energy and the efficiency of the data transfer is directly proportional to the coupling efficiency (i.e. correct resonance frequency matching between the transmitter and the receiver), which is not always easy to achieve. Capacitive coupling (CC) [100] uses electrical signals with a couple of electrodes at the transmitter and receiver, respectively. Only one of the electrodes at each side is attached to the body while the other electrode is floating (ground electrode needs only to be in proximity) and the signal is generated between the body channel transceiver by making a current loop through the external ground. Thus, unfortunately, the path loss has high variability based on environmental conditions.

We use an alternative cable-less architecture for IBNs using galvanic coupling (GC) technology for communications among implants. GC utilizes low or medium frequency (1 kHz-100MHz) and weak ($< 1mW$) electrical currents, which are modulated with data and coupled directly to the tissue [103]. Differently from SoA RF solutions, GC IBNs does not show privacy risks since the signals do not propagate outside the body, and consumes two orders of magnitude less energy than RF method [104, 105].

Related works

Existing GC efforts focused on signal strength changes in tissues [100, 106, 103] and the characterization of human tissues [104, 100, 107], which are a valuable base to explor the feasibility of communication schemes that are difficult to be performed directly on the human body.

Some works have been conducted in developing GC testbeds. For example, a test system has been designed and implemented, which considers a complex programmable logic device (CPLD) containing all the digital signal processing blocks of the transmitter, and, besides the analog units, a field-programmable gate array (FPGA) at the receiver to provide the digital demodulation and interfaces [106]. More recently, a base band transmission has been implemented in a FPGA board based on impulse radio (IR) employing a pulse position modulation (PPM) [108]. In [109] design a testbed using two USRP software defined radios (SDRs), one at the transmitter and the other at the receiver side, supporting low frequency daughterboards. Anyhow, an effective and repeatable GC platform to carry out experiments is still a challenge.

Proposed sound card based GC testbed

We here design and implement a GC testbed that is based on PC sound card and Matlab environment, hence easily replicable for the interested research community. The main advantages of the proposed testbed architecture are that: (i) such scheme requires limited equipment since only ordinary PCs and Matlab software are needed; (ii) allows high flexibility since all parameters, including carrier frequency, bandwidth and modulation order, may be varied directly in the TX/RX Matlab programs allowing a quick evaluation of the resulting effects; (iii) real time option for the receiver by including a Data Acquisition Toolbox (Daq Tbx) in Matlab that exploits the real time data logging feature of the toolbox [110], so that real time transmission and evaluation of physiological data sets are possible; (iv) BER evaluation of the experimental

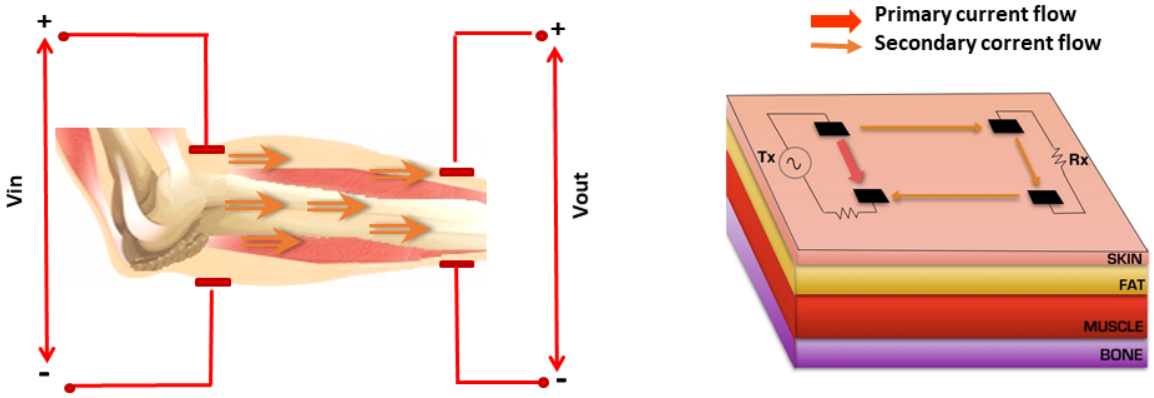

Figure 7.1: GC setup on skin surface with detail on multiple tissues

setup.

7.2 Background on GC communication technology

An alternative ultra-low power solution that uses the human body as a communication medium is GC technology. In GC, a pair of electrodes is used to directly couple a weak electric current into the human body, so that the electrical signal is applied differentially between the two electrodes of the transmitter and secondary paths of propagation are used for potential difference detection at the electrodes of the receiver [100]. Recommendetion from ICNIRP [111] suggests to limit the signal within the safe bound of 1 mA, which is easily matched from GC technology, usually injecting currents in the order of 0.5 mA [112].

Fig. 7.1 represents the conceptual illustration of GC: the transmitter is composed of a pair of electrodes with typical distance of 5 cm (on-skin case is depicted in Fig. 7.1, although the electrodes could be places in any tissue) to inject low intensity electrical currents as data signals. While the primary current flows through the two transmitter electrodes, weak secondary electrical currents carry the information to a distant pair of receiver electrodes using layered tissues conduction. Experiments prove that a weak secondary current can be detected at the receiver with a transmission range

of 20-30 cm. GC may use any type of electrode, whose usual size is approximately 10 mm [113], and consumes only 0.24 nJ per received bit compared to 106 nJ/b of Zigbee [100]. Indeed, due to its frequency range, the GC signal is restricted to the body so that GC communication is highly energy efficient, resulting in a long lifetime for battery-powered implants. The tissue heating is low due to the limited attenuation at the frequencies used, and communication is interference-free and secure from external fields. The operative frequency range of GC is a tradeoff among tissue attenuation, interference with other natural signals (e.g., ECG and EEG signals), and other impairments. Experiments show that the usable frequency range is 1kHz-100MHz [103], so that other natural signals are not impaired.

7.2.1 Channel Model for the human body

The main approaches modeling the electrical behavior of human tissues include wave numerical techniques, for instance, finite element analysis (FEA) and finite difference time domain method (FDTD) [114, 115], quasi-static approximations, [116, 117], and equivalent circuit analysis (ECA) models.

Field analysis with FEA and FDTD are accurate but expensive for the required time computation. The quasi-static approximations of field distribution are less computationally complex but only model low frequency Maxwell's equations, so that they are not valid for high frequency applications.

The ECA model gives an easy transfer function with accurate gain calculation, and is valid for a wide range of frequency. Several ECA methods focus on single tissue layer, such as [107], while a recent analytical model has been proposed that considers a three dimensional multi-layered tissue, validated through finite element simulations [104].

7.2.2 Related works on GC testbed

Some works have been conducted to develop GC testbeds with different hardware and software features, in order to validate the aforemnetioned channel models and/or prove the GC viability as IBC technology.

A low power single chip biomedical system is designed in [40], firstly exploiting GC paradigm, with a continuous phase frequency shift keying (CPFSK) modulation scheme.

The test system in [114] includes battery powered transceiver and an FPGA as interface between analog front-end and digital communication link. Two modulation schemes have been used, frequency shift keying (FSK) and binary phase shift keying (BPSK), with a 128 and 255 kbps, respectively.

In [118], the authors build up a transceiver to communicate with both on-body and implanted sensors with a frequency range in the order of tens to hundred MHz and a data rate up to 5 Mbps.

Base band transmissions are developed in a FPGA board based on impulse radio (IR) with a PPM, and the corresponding BER performance is evaluated [108].

A GC tesbed has been proposed recently based on off-the-shelf SDR platforms with low frequency daughterboards and Matlab environment, which presents BER performance for differential BPSK (DBPSK) modulation for different level of transmitted power in case of one transmitter and one receiver implant [109], and BER QPSK performance in case of two transmitters and one receiver [111].

Finally, given the heterogeneity of experimental setups and conditions, and some discrepancies observed between results in literature, some studies have been conducted to evaluate the influence of different experimental settings on GC measurements [119]. On that purpose, different experimental setups have been considered to analyze specific key issues such as load resistance, grounding, effect of cables, and type of measurement device [119].

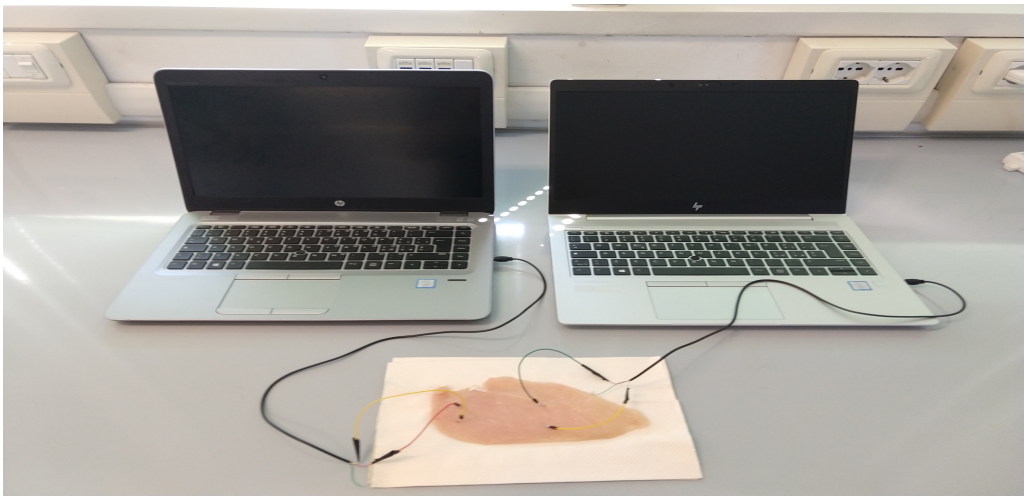

Figure 7.2: Experimental setup of the GC testbed

Anyhow, all the developed systems require specific hardware and software and show low flexibility, resulting in GC platforms difficult to replicate for carrying out experiments.

7.3 GC testbed architecture

Since the common sound cards support signals whose frequency range is included in the GC frequency range (1KHz-100MHz), we develop and implement a GC testbed for intra-body communication links employing only ordinary PCs with sound card support and Matlab software, resulting in a simple platform to emulate a single implanted sensor transmission/reception.

The developed system may be easily reproduced and is flexible since all the parameters may easily changend in the TX/RX Matlab programs, while allowing real time transmission of physiological data sets. The developed testbed manages all aspects of communication, including, among the others, bit generation, preamble insertion and raised cosine filtering.

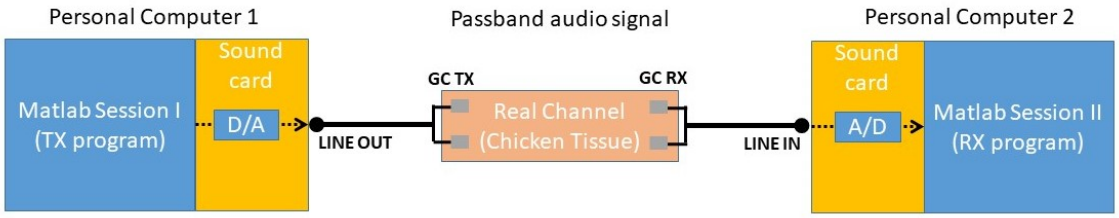

Figure 7.3: Setup of the GC audio-band testbed using two PCs

7.3.1 Blocks design of the GC system architecture

The main advantage of the proposed GC system architecture is its limited equipment requirement, consisting of two common PCs with sound card and the basic Matlab package for transmitter and receiver development, as shown in Fig. 7.2 and in the block diagram in Fig. 7.3. Bridging the channel and the two PCs, we ensure to use battery powered PCs without connection to the grid, in order to isolate the common ground return paths of the transmitter and the receiver, as required from GC technology [111].

Fig. 7.3 illustrates that only two Matlab sessions are required, one per PC, to implement the transmitter and receiver respectively, and the sound cards are used to support real signal transmission/reception in a subset frequency range of GC technology [103]. On that purpose, Fig. 7.3 shows that the transmitted data generated through Matlab are converted from digital to analog domain to be sent over the sound card of the transmitter. A cable is connected to the *LINE OUT* jack to carry the signal outside the PC. As detailed later, the cable is attached to two electrodes that represent the GC transmitter, which send the signal over the tissue through GC communication technology. At the other side, the two receiver's electrodes bring the received signal to the other PC through the cable connected to the *LINE IN* jack. The data are thus processed in the Matlab session II where the receiver program is running.

In the following, the blocks diagram of the proposed audio-band GC system are

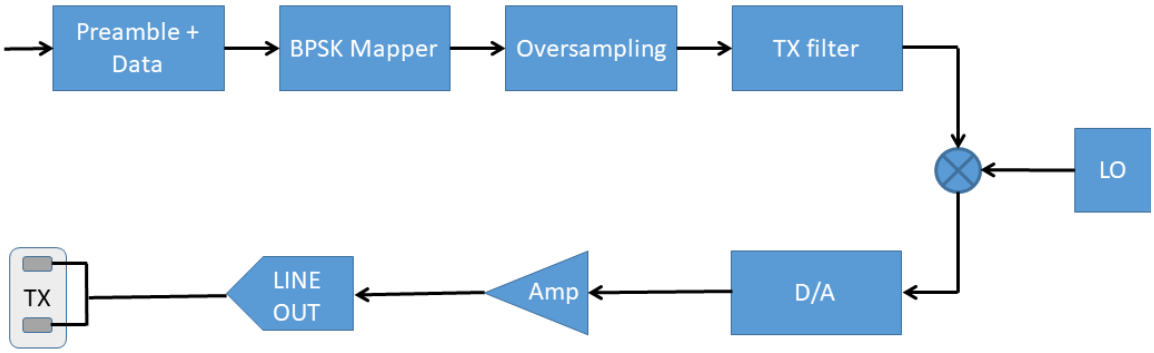

Figure 7.4: Block diagram of the GC transmitter

Table 7.1: Parameters setting

Parameter	**Value**
Carrier frequency f_c (KHz)	15
Waveform sampling frequency f_{s_a} (KHz)	48
Oversampling frequency f_s in number of samples	4
Sampling time T_s (ms)	0.16
RX oversampling frequency $f_{s_{rx}}$ in number of samples	2
roll-off of TRX filters R	0.2
delay of TRX filters D in number of samples	8
QAM modulation order$M$	2
RX Wiener filter length N_f in number of samples	11
Modulated sequence N in number of symbols	1000
Preamble length N_{pre} in number of symbols	192

described, including the functional blocks of the transmitter and the receiver, shown in Fig. 7.4 and 7.5, respectively.

7.3.2 Functional blocks of the GC transmitter

Before detailing each block of the transmitter shown in Fig. 7.4, we summarize in the following Table 7.1 the main parameters values of the system. Note that both transmitter and receiver parameters are included for completness.

Fig. 7.4 shows that after bit generation, a preamble is inserted and the data are modulated in BPSK. The sequence is oversampled by 4, as specified in Table 7.1, and passes through a squared-root-raised-cosine (SRRC) filter. The corresponding baseband samples $x(nT_s)$ are thus generated, with $n = 0, 1, ..., f_sN - 1$ and sampling

Table 7.2: Matlab audio playing statements

sObj = audioplayer(s_{tx},48000);	% To create an audioplayer object for signal Stx, using sample frequency at 48000 Hz
playblocking(sObj);	% To play from beginning till playback completes

time T_s.

The resulting sequence is then upconverted to the carrier frequency by multiplying it by the *cos* signal, which represents the local oscillator (LO) obtained via software-define radio in Matlab program. This yields an audio passband transmitted signal s_{tx}:

$$s_{tx}(nT_{s_a}) = x(nT_{s_a})\cos(2\pi f_c nT_{s_a}) \tag{7.1}$$

where $T_{s_a} = 1/f_{s_a}$ with $f_{s_a} = 48000$ Hz, whose value is chosen according to the standard sample frequency of PC sound card, and f_c is the carrier frequency. According to the parameters setting in Table 7.1, $T_s = 8\ T_{s_a}$ with a net data rate $R = 6$ kbs, in line with several biomedical applications showing sparse and low rate traffic generated by implanted sensors [105, 112]. Anyhow, the achievable data rate may be incresed by appropriately choosing the value of f_s, f_{s_a}, f_c shown in Table 7.1.

Fig. 7.4 illustrates that the obtained audible signal s_{tx} passes through the sound card's internal amplifier, which may be replaced with an external amplifier circuit using Arduino. Then, the signal is sent out to the *LINE OUT* jack by using the following simple Matlab statements in Table 7.2, which play the software-generated transmitted signal:

Through a wire, the output signal is then connected to two electrodes, that represent the GC transmitter.

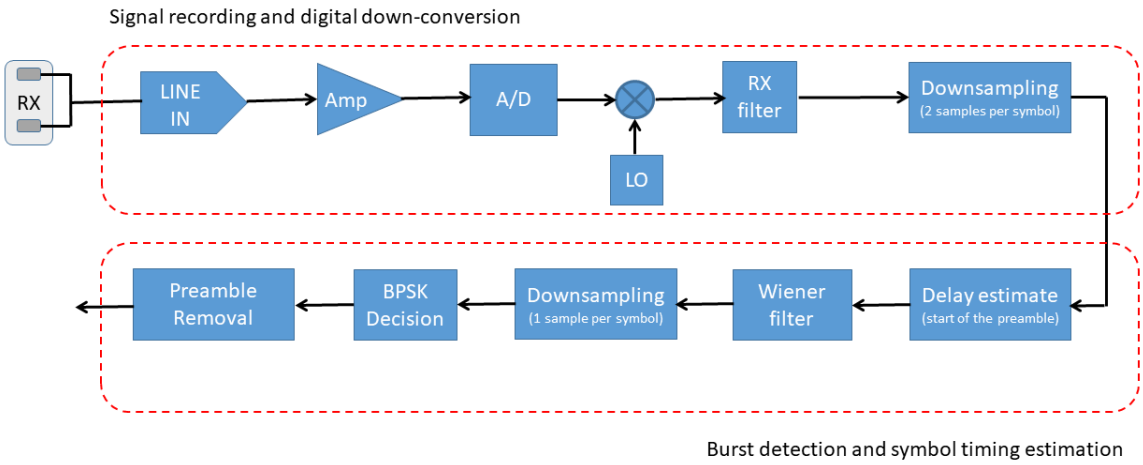

Figure 7.5: Block diagram of the GC receiver

Table 7.3: Matlab recording statements

recObj=audiorecorder(48000,16,1);	% To create a 48000 Hz, 16-bit, 1 channel recorder object;
Tsamp=1/48000;	% Sampling time;
Trecord=$N * f_s * T_{s_a}$;	% Recording time, where: N is the modulated sequence lenght, fs is the oversampling freq equal to 16;
recordblocking(recObj,Trecord+3);	% To record for length of time, Trecord+3, expressed in seconds;
s_{rx} = getaudiodata(recObj);	% To return the recorded audio data as a double array.

7.3.3 Functional blocks of the GC receiver

The main blocks of the receiver developed in Matlab are shown in Fig. 7.5 and may be split in the following two macro-blocks: (i) signal recording and digital down-conversion and (ii) burst detection and symbol timing estimation.

Signal recording and digital down-conversion

A Matlab session must to be open in the PC connected with the GC receiver for running the receiver program, which includes the following Matlab statements in Table 7.3 to record the received signal and store the data in the array s_{rx}.

As shown in Fig. 7.5, after recording the signal s_{rx} in digital format, which

passes through the sound card amplifier, a digital down-conversion is performed by multiplying the received sampled signal by $\cos(2\pi f_c n T_{s_a})$, where f_c is the carrier frequency at the receiver. The sequence then is sent to an SRRC filter, resulting in a baseband received signal $y(nT_{s_a})$ with $n = 0, 1, ..., f_s N - 1$.

The output signal is then decimated by two so that the next blocks, described below, work at two samples per symbol ($f_{s_{rx}} = 2$ as specified in Table 7.1). The obtained sampled signal may be expressed as

$$y(nT_s) = s_{tx}(nT_s)e^{j\theta} + v(nT_s) \tag{7.2}$$

where $n = 0, 1, ..., f_{s_{rx}} N - 1$, $s_{tx}(nT_s)$ is the envelope samples of the passband signal, $v(nT_s)$ is the sampled AWGN noise, θ is the random phase noise due to time delay.

Burst detection and symbol timing estimation

Being the packet composed by a preamble followed by data, the burst detection is performed by estimating the start of the preamble through a correlation method. Specifically, the transmitted preamble, known at the receiver, is cross-correlated with the receveid data so that the position of the correlation's peak gives an estimated of the preamble start position:

$$\hat{t}_p = \underset{n}{\operatorname{argmax}} \left| \sum_{k=0}^{L-1} y((n+k)T_s) p^*(kT_s) \right| \tag{7.3}$$

where $\hat{t}_p$ is the estimate of the sample index where the reference preamble p begins, N_{pre} is the preamble's length, $L = f_{s_{rx}} N_{pre}$ since the receiver is working at two samples per symbol (oversampling frequency $f_{s_{rx}} = 2$), and $n = 0, 1, ..., f_{s_{rx}} N - 1$.

Hence, the received signal is shifted in time according to the estimated start of the preamble $\hat{t}_p$ and is equalized with a Wiener filter, that also performs symbol timing

improving the delay estimate obtained with (7.3).

The coefficients $w(i)$ of the filter, with $i = 1, ..., N_f$, are calculated by using the shifted received preamble $y_p(nT_s) = y(nT_s + \hat{t}_p)$ and the known transmitted one $p(nT_s)$ with $n = 0, 1, ..., f_{s_{rx}} N_{pre} - 1$. In more details, the vector $\mathbf{w} = \left[w_1, w_2, ..., w_{N_f}\right]$ of the coefficients can be computed by minimizing the mean square error (MSE) between the transmitted and estimated preamble, defined as

$$\epsilon = E\left\{\left[p(nT_s) - \hat{p}(nT_s)\right]^2\right\} \tag{7.4}$$

Setting the following partial derivatives of the error (7.4) equal to zero

$$\frac{\partial \epsilon}{\partial w_i} = 0, \text{ for } i = 1, 2, ..., N_f \tag{7.5}$$

we can solve (7.4), (7.5) for the coefficients w_i by inverting an autocorrelation matrix of size $N_f \times N_f$, which leads to the following Wiener-Hopf equation

$$\mathbf{w} = \mathbf{R}_{y_p}^{-1} \mathbf{r}_{py_p} \tag{7.6}$$

where $\mathbf{R}_{y_p} = \{r_{y_p}(k)\}$ is the autocorrelation matrix of the received preamble y_p, whose elements are $r_{y_p}(k) = E\left\{y_p(i-k)y_p(i)\right\}$, and $\mathbf{r}_{py_p} = \{r_{py_p}(k)\}$ is the cross-correlation vector between the transmitter preamble p and the received one y_p, whose elements are defined as $r_{py_p}(k) = E\left\{p(i-k)y_{p_k}(i)\right\}$, and $i, k = 1, 2, ..., f_{s_{rx}} N_f$.

After calculating the Wiener coefficients using only the preamble, the filter is applied to all the sequence, so that its output is the estimated transmitted sequence $\hat{x}(nT_s)$, expressed as

$$\hat{x}(nT_s) = \sum_{l=0}^{N_f - 1} w(lT_s) y((n-l)T_s + \hat{t}_p) \tag{7.7}$$

After a downsampling operation at one sample per symbol, the BPSK symbol

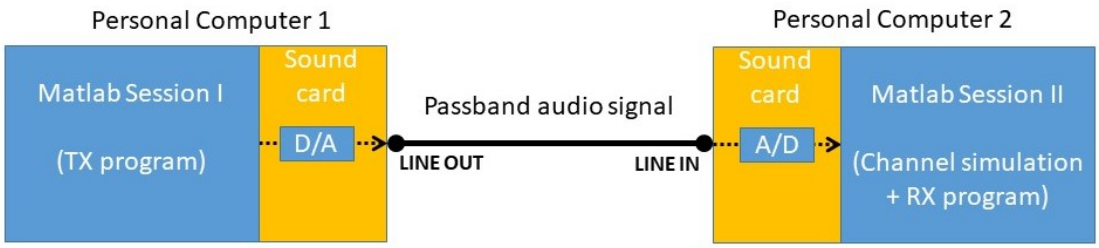

Figure 7.6: Audio-band testbed using two PCs and a wire

sequence is demapped to a bit sequence and the preamble is removed, thus completing the receiver operations. The obtained bit sequence may be hence compared to the transmitted one for BER calculation.

7.3.4 Implementation of the GC system

Before evaluating the performance of the overall system with a real tissue-based GC channel, we first test only the transmitter and the receiver, for which the configuration in Fig. 7.6 is considered. Then, an experimental setup is evaluated with real tissue for GC transmissions as in Fig. 7.3.

Fig. 7.6 derives from Fig. 7.3 by substituting the steak with a simple wire connecting the *LINE OUT* sound card's jack of the PC running the Matlab transmitter program with the *LINE IN* jack of the other PC running the receiver program.

For the final setting, shown in Fig. 7.2 and 7.3, the wire connecting *LINE IN* and *LINE OUT* jacks of the two PCs is cutted and each of its two parts are attached to the electrodes of the GC transmitter and receiver, respectively. Since the wire is composed by three electric clables, two of them are connected to the electrods on each side, while the third one remains floating. Under this configuration, the two transmitter and receiver Matlab session runs in parallel to perform the experimental evaluation detailed in the following section.

7.4 Experimental Setup and Performance Evaluation

After testing the architecture in the configuration shown in Fig. 7.6, which have confirmed the feasibility of the proposed transmitter and receiver architecture, we have conducted experiments in the final real scenario shown in Fig. 7.2 and Fig. 7.3. The parameters setting is detailed in Table 7.1, and the average BER is calculated over 100 iterations.

Note that we use really small size electrodes (in the order of 0.5 mm) while the SoA is employing 1 cm electrodes [113]. Although such choice would reduce the achievable distance between GC transmitter and receiver, in this way we test a real configuration scenario for future miniaturized implantable devices. The inter-distance between the electrodes at both the transmitter and receiver is set equal to 1 cm, while the distance between the transmitter and receiver is varied during the experiments, together with the transmit power.

Fig. 7.7 and Fig. 7.8 show the transmitted and received signal in the frequency domain, respectively, for 3 cm distance between GC transmitter and receiver. Fig. 7.7 refers to the transmitted signal before being modulated on the carrier frequency, as well as Fig. 7.8 illustrates the received signal after demodulation and filtering. The comparison between the two figures confirms that the received signal exibiths the same shape of the transmitted one, since the side lobe of the receiver signal is maintained low by the filter being its amplitude around 90 dB less than the main one.

Fig. 7.9 shows BER performance by varying the transmit power for different distance values between transmitter and receiver. As expected, BER performance decreases when increasing the distance, although the performance for 2, 4, 6 cm result to be quite similar. We are able to achieve a BER in the order of 10^{-4} with 9.5

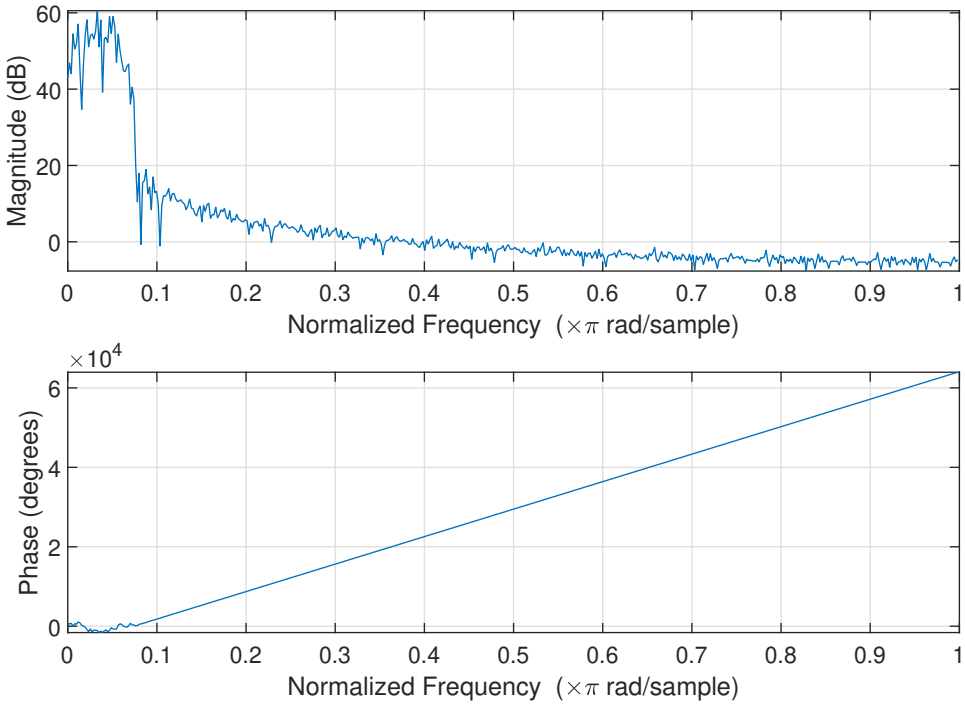

Figure 7.7: Transmitted signal in frequency domain

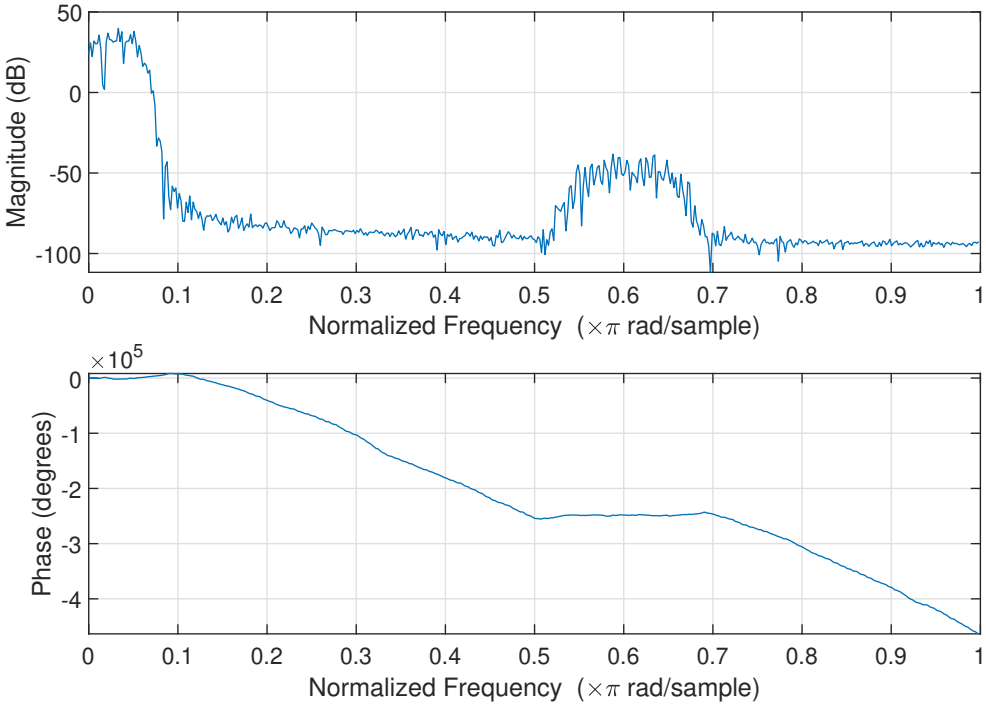

Figure 7.8: Received signal after RX filter in frequency domain

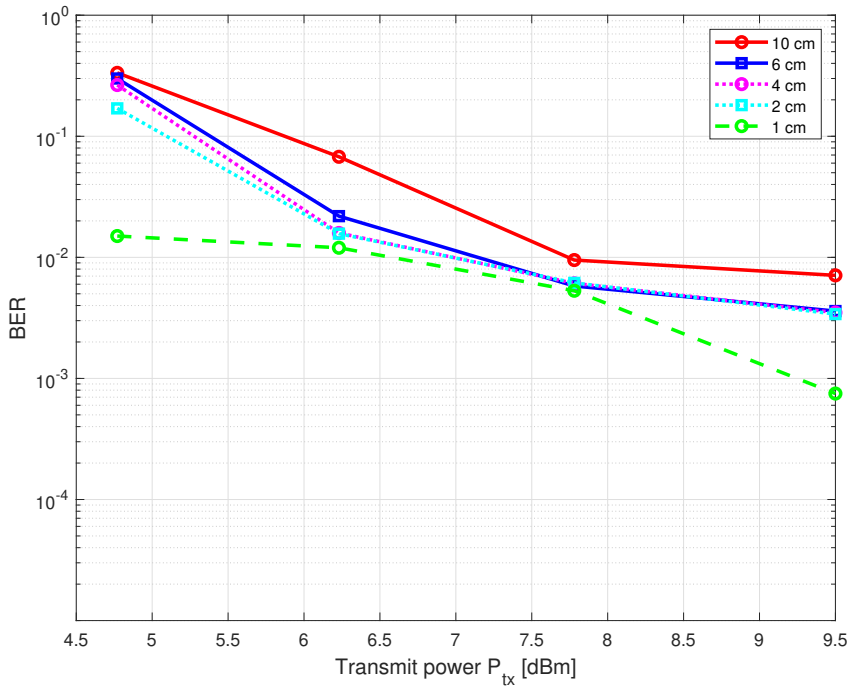

Figure 7.9: BER vs transmit power for different distances between GC transmitter and receiver

dBm transmit power for 1 cm distance, reaching $7 \cdot 10^{-3}$ for 10 cm, a valuable result considering the small electrode size of 0.5 mm and the simple receiver that is not employing any correction code. More robust receiver may be envioned based on ultra wideband (UWB) to improve the performance while mantaining simple and energy efficient receiver [71], as required by biomedical implantable devices.

7.5 Conclusions

We have proposed a sound card based GC testbed as a quick repeatable platform to carry out experiments. The detailed description of the implemented test system may support the interested researchers in replicating the testbed and thus stimulate further research in the GC field. Experimental tests on real chicken tissue as GC communication channel have been conducted to prove the feasibility of the proposed architecture.

We achieve a BER in the order of 10^{-3} with 9.5 dBm transmit power for distances in the range $2 - 10$ cm, employing an simple receiver and electrodes with really small size (0.5 cm), while the SoA is usually employing 1 cm electrodes. Ongoing works include exstensive simulation to evaulate the effect of the carrier frequency, bandwidth, audio sampling frequency, electrodes size, as well as inter-electrodes distance at both the transmitter and receiver. Moreover, we are implementing an extension of the proposed testbed with Arduino platform in order to modulate the signals on a frequency range larger than the audio signals. Future research directions will exploit compressed sensing (CS) and UWB techniques to save time and energy [111, 71], a strict requirements in intra-body networks for medical applications.

8

Phase recovery of XPIC receivers

Reduced complexity Kalman based algorithms are proposed to recover the phase of cross-polar interference cancellation (XPIC) receivers in microwave radio relay links. In particular, two completely independent radio frequency (RF) transceiver chains are considered for the two different polarizations, in order to have the maximum flexibility to connect different single carrier transceivers to dual-polarized antennas. A one-state Kalman model is proposed, which is of low complexity and thus suitable for a modern higher data rates M-ary quadrature amplitude modulation (M-QAM) receiver. Moreover, a further reduced complexity version is developed that uses a lower amount of information to recover the phase at the receiver, as well as a downsampling procedure to speed up the Kalman algorithm, and an alternative error computation that is essential to ease the Kalman implementation. It is worth noting that the three last simplifications are general and can be applied not only to a one-state Kalman model. Simulation results compare the proposed simplified Kalman solutions to typ-

ical phase-locked loop (PLL) algorithms proving their comparable performance with the benefit of lower complexity. Finally, the relationships between the Extended Kalman and the PLL approaches are investigated. The obtained relation is essential for the cross-polar phase recovery, since, as far as the authors know, there are not closed form solutions for the PLL parameter optimization in cross schemes.

8.1 Introduction

The recent spread of smart applications has led to the growth of data traffic in the last years. As a result, the development of fifth-generation (5G) communications technology is required to fulfill the increasing users' traffic requirement. On this purpose, operators and carriers are claimed to improve the user experience and, in general, the overall network performance. In this sense, there are notable market interests on the development of innovative backhaul solutions to accommodate the increased wireless traffic and the resulting higher bandwidth demand [120].

Cross polarization interference cancellation (XPIC) technology represents the enabler for dual-polarized transmissions over the same radio frequency (RF) channel, so that the link capacity is doubled by using two orthogonal polarizations channels over the same link [121].

In order to have the maximum flexibility from an installation and maintenance point of view, some XPIC architectures are based on two independent and unsynchronized transceiver paths for backhaul links, with completely independent transmitter and receiver local oscillators (LOs) [122].

Differently from multiple input multiple output (MIMO) solutions that work with a carrier-over-interference ratio (C/I) almost equal to 0 dB, XPIC operating conditions have cross polarization discrimination (XPD) around $20 - 25$ dB. Despite the fact that such XPD value could be considered almost error free for low order mod-

ulations, higher order QAM schemes still could represent a challenge [123][124], for example they highly suffer from phase noise even in line of sight (LoS) environments.

Carrier frequency and phase synchronization are also challenging for higher order M-QAM single polarization receivers, and may be accomplished by a Kalman algorithm, as described in [125][126].

In [127], we proposed a cross-polarized Kalman based phase recovery scheme for an XPIC architecture that jointly recovers the phase of both the received signal and the interfering one at the input of the cross-polar interference canceller. In particular, a four-state extended Kalman filter (EKF) algorithm for an XPIC receiver was derived, along with a modified version that exploits two simpler two-state EKFs, one for the main polarization path and the other for tracking the interference signal phase.

In this work, starting from the two-state Kalman model for a XPIC receiver [127], we focus on studying the computational complexity of such schemes in order to develop practical architectures that could be efficiently implemented in modern digital hardware for high data rate microwave backhaul links. We think that computational aspects are crucial to make the Kalman based architecture more attractive with respect to the simpler one based on two phase-locked loops (PLLs), especially from a hardware feasibility point fo view. Moreover, we think that a comprehensive study of the performance-complexity trade off is crucial in order to help the interested technical community in developing real hardware prototypes of the scheme proposed in [127].

The main contributions of the work presented in this chapter are listed in the following:

- a low complexity Kalman filter scheme is proposed for phase recovery in XPIC systems, based on two one-state EKFs. Although such solution shows a lower computational burden with respect to the scheme in [127], it provides similar or anyway acceptable performance.

- the performance of the presented scheme is also evaluated by studying the effects of the following complexity reduction algorithm implementations:
  - The computational burden needed for computing the covariance matrix inverse may be reduced. Specifically, since the phase noise variations are slow respect to the symbol timing, the covariance matrix computation update may be kept constant during several Kalman iterations without affecting the overall algorithm performance. This is equivalent to make a downsampling only inside the covariance matrix computation loop;
  - the phase-error computation is modified in order to avoid two phase counter-rotations in the Kalman state update equations. In this way the hardware design is more feasible, since phase rotation are computationally expensive;
  - complexity reduction is also achieved by considering in the phase error computation only the in-phase or in-quadrature component of the signals.
- the relation between the Extended Kalman Filter (EKF) based approach and the commonly used PLL parameters is extensively studied. While [128] probes the relation between Kalman and PLL gains, we investigate the connection between the Extended Kalman version and the PLL. This relation is important for the cross-polar phase recovery, since, as far as the authors know, while there are closed form solutions for PLL parameters in single polarization receivers, they do not exist for the cross PLL parameter optimization. Indeed, such EKF-PLL relation could be useful to optimize cross PLL parameters through EKF simulations. In particular, being the PLL implementation easier than a Kalman scheme, we envisage a final practical solution where a typical cross PLL scheme with fixed gains is replaced by a cross PLL with variable gains, which are calculated through Kalman simulation, resulting in a solution more robust to channel variations.

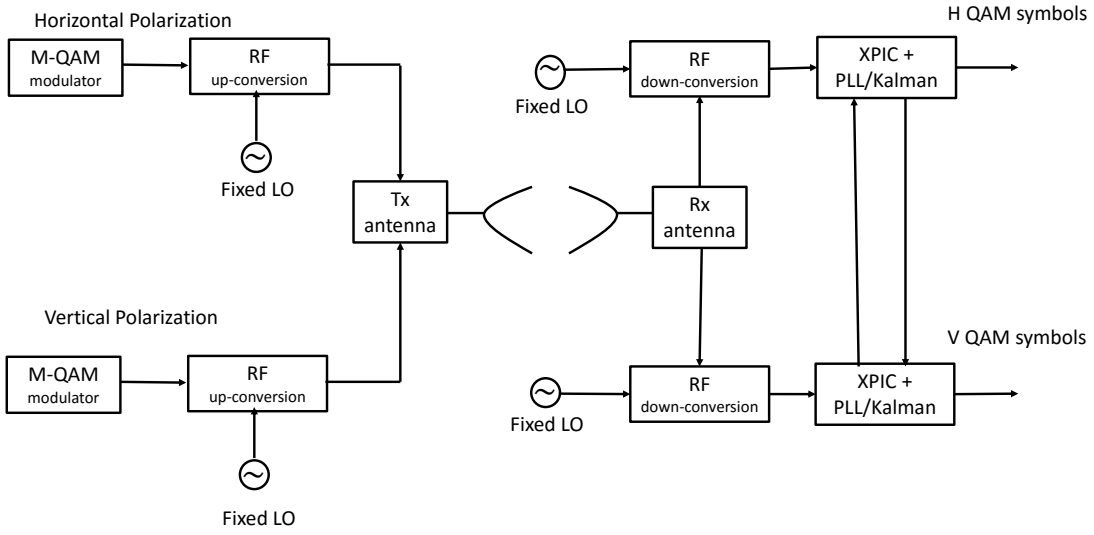

Figure 8.1: System Architecture

The research work is organized as follows: Sec. 8.2 describes the system model, Sec. 8.3 briefly reviews the EKF models described in [127], while Sec. 8.4 analyzes the proposed reduced complexity Kalman schemes and the relation between the EKF parameters and the PLL filter gains. Sec. 8.5 shows some interesting simulation results, and, finally, concluding remarks wrap up and close the work in Sec. 8.6.

8.2 System Model

We consider a backhaul link with two distinct receiver paths and unsynchronized local oscillators (LO), as in [122], [127]. Fig. 8.1 depicts the considered XPIC architecture, highlighting the two distinct receiver paths, with unsynchronized local oscillators (LO) for a backhaul link [122]. Since our focus is a typical microwave backhaul application, we model the channel with only AWGN without multipath fading as in [127].

Let us consider the signal $r_0(n)$, received at one polarization path:

$$r_0(n) = t_0(n)e^{j\theta(n)} + gt_1(n)e^{j\phi(n)} + w(n) \tag{8.1}$$

where $t_0(n)$ is the n^{th} complex QAM transmitted symbol of the main polarization component with phase $\theta(n)$, g is the cross-polar attenuation factor, $t_1(n)$ is the n^{th} complex QAM symbol transmitted on the interference path with phase $\phi(n)$, and $w(n)$ represents the additive white Gaussian noise (AWGN) at the receiver.

The aim of both the Kalman and PLL algorithms is to estimate the phases $\theta(n)$ and $\phi(n)$, along with the corresponding frequencies $\dot{\theta}(n)$ and $\dot{\phi}(n)$, by using the input of the main polarization slicer:

$$u_0(n) = \left(r_0(n) - gt_1(n)e^{-j\hat{\phi}(n)}\right) e^{-j\hat{\theta}(n)} \tag{8.2}$$

where $\hat{\phi}(n)$ and $\hat{\theta}(n)$ represent the estimated phases of the main and cross polar signals at the receiver. The cross-polar attenuation factor g is assumed to be known, since, in high-order M-QAM receivers for microwave backhaul links, a linear filter interference canceller/equalizer is able to converge in presence of both baseband phase and frequency errors, providing a good initial guess for the PLL or the Kalman algorithms. Usually, during the acquisition phase, the adaptive linear filter works in a blind mode, typically by a constant modulus algorithm (CMA), and switches to a minimum mean square error (MMSE) algorithm once the normal operating condition is reached. Once the equalizer switches to MMSE, all the others recovery algorithms, like the Kalman phase recovery one, start using the decisions at the output of the slicer. In the following Sec. 8.3, we give a short outline of the phase recovery using the two-state Kalman models [127], and then, in Sec. 8.4, we describe the proposed solutions, which include (i) a one-state Kalman model, (ii) a further simplified one-state version that uses a lower amount of information to recover the phase, and (iii) a downsampling of the covariance matrix computations to speed up the Kalman

algorithm. All the proposed schemes aims to reduce the complexity of a Kalman based solution in a smart way in order to not degrade the performance. An alternative error computation that can decrease the computational load of Kalman implementation is also included, as well as some interesting relations between the Kalman and PLL parameters, useful for cross PLL parameters optimization, which is still missing.

8.3 XPIC Phase Recovery Based on Kalman Filtering

Since our purpose is to estimate the phase and the frequency of the signals in an XPIC scheme, such variables are considered in the Kalman state vectors. We also define the observation vectors and the error to be minimized through the Kalman approach in order to obtain the estimates of the signal frequency and phase discrete values.

Specifically, we consider a two-state XPIC Kalman algorithm for the main path and another one for the cross polar interference, so that the two-state vectors of the main and cross polar signals are expressed [127]:

$$\mathbf{x}_0(n) = \begin{bmatrix} \theta(n) \\ \dot{\theta}(n) \end{bmatrix} \tag{8.3}$$

$$\mathbf{x}_1(n) = \begin{bmatrix} \phi(n) \\ \dot{\phi}(n) \end{bmatrix} \tag{8.4}$$

The state evolution of the linearized Kalman filter results:

$$\mathbf{x}_0(n) = \begin{bmatrix} \theta(n) \\ \dot{\theta}(n) \end{bmatrix} = \mathbf{F} \begin{bmatrix} \theta(n-1) \\ \dot{\theta}(n-1) \end{bmatrix} \tag{8.5}$$

and

$$\mathbf{x}_1(n) = \begin{bmatrix} \phi(n) \\ \dot{\phi}(n) \end{bmatrix} = \mathbf{F} \begin{bmatrix} \phi(n-1) \\ \dot{\phi}(n-1) \end{bmatrix} \tag{8.6}$$

where the transition matrix $\mathbf{F}$ is defined as

$$\mathbf{F} = \begin{bmatrix} 1 & 1 \\ 0 & 1 \end{bmatrix} \tag{8.7}$$

The transition matrix definition $\mathbf{F}$ takes into account the fact that the residual carrier frequency offset at the PLL/Kalman input is usually lower than the initial one at the modem input, since a first stage coarse frequency detector is able to make it smaller. Moreover, the frequency offset time variations are anyway slower compared to the phase noise random fluctuations.

While the cross polar observation vectors for the main and cross polarization signal, $\mathbf{r}_0(n)$ and $\mathbf{r}_1(n)$ respectively, are defined as

$$\begin{aligned} \mathbf{r}_0(n) &= \mathbf{h}_0(\mathbf{x}_0(n)) + \mathbf{w}_0(n) \\ \mathbf{r}_1(n) &= \mathbf{h}_1(\mathbf{x}_1(n)) + \mathbf{w}_1(n) \end{aligned} \tag{8.8}$$

where

$$\mathbf{r}_0(n) = \begin{bmatrix} Re(\tilde{r}_0(n)) \\ Im(\tilde{r}_0(n)) \end{bmatrix}, \ \mathbf{r}_1(n) = \begin{bmatrix} Re(gt_1(n)) \\ Im(gt_1(n)) \end{bmatrix} \tag{8.9}$$

and $\mathbf{h}_0(\mathbf{x}_0(n)) \doteq \mathbf{h}_0(n)$ and $\mathbf{h}_1(\mathbf{x}_1(n)) \doteq \mathbf{h}_1(n)$ are the observer vectors, defined as

$$\mathbf{h}_0(n) = \begin{bmatrix} Re(\hat{t}_0(n)e^{j\theta(n)}) \\ Im(\hat{t}_0(n)e^{j\theta(n)}) \end{bmatrix}, \ \mathbf{h}_1(n) = \begin{bmatrix} Re(g\hat{t}_1(n)e^{j\phi(n)}) \\ Im(g\hat{t}_1(n)e^{j\phi(n)}) \end{bmatrix} \tag{8.10}$$

$\hat{t}_0(n) = \hat{a}(n) + j\hat{b}(n)$ is the output of the symbol slicer, $\tilde{r}_0(n) = r_0(n) - g\hat{t}_1(n)e^{-j\phi(n)}$, and:

$$g\hat{t}_1(n)e^{j\phi(n)} = r_0(n) - \hat{t}_0(n)e^{j\theta(n)} = \hat{c}(n) + j\hat{d}(n) \tag{8.11}$$

While $\mathbf{w}_0(n)$ and $\mathbf{w}_1(n)$ are the observation noise on the main and interference path, respectively. The EKF algorithms minimize the two distinct correspondent error vectors $\mathbf{e}_0(n)$ and $\mathbf{e}_1(n)$ defined as

$$\begin{aligned} \mathbf{e}_0(n) &= \mathbf{r}_0(n) - \mathbf{h}_0(n) \\ \mathbf{e}_1(n) &= \mathbf{r}_1(n) - \mathbf{h}_1(n) \end{aligned} \tag{8.12}$$

The complete derivation of the EKF iterative equations may be found in section III of [127].

8.4 Proposed Reduced Complexity Kalman Algorithms

8.4.1 One-State Kalman Model

In this section, a simplified one-state Kalman model is developed for an XPIC scheme where only the phase of the signal is considered as state parameter, while the frequency is processed as an external input, obtaining a substantial complexity reduction. The proposed one-state model is derived starting from the two-state Kalman model [127], in a way similar to the single-polarization scheme in [126].

The one-state model can be represented as

$$\begin{aligned} x_0(n) &= \theta(n) + \dot{\theta}(n) + v_0(n) \\ x_1(n) &= \phi(n) + \dot{\phi}(n) + v_1(n) \end{aligned} \tag{8.13}$$

where $v_0(n), v_1(n)$ represent the state noise signals. In the following we use the outputs of the hard decision $\hat{t}_0(n) = \hat{a}(n) + j\hat{b}(n)$ and $g\hat{t}_1(n) = \hat{c}(n) + j\hat{d}(n)$ to estimate the frequency $\dot{\theta}(n)$ and $\dot{\phi}(n)$. Note that the symbol $\hat{c}(n) + j\hat{d}(n)$ is always obtained from the slicer decisions of the main polarization component signal as follows:

$$\hat{c}(n) + j\hat{d}(n) = r_0(n) - \hat{t}_0(n)e^{j\hat{\theta}(n)} \tag{8.14}$$

which implies that the main path does not requires any feedback from the cross polar component, so that the two links work independently in a reciprocal blind manner.

The frequencies are computed by means of two first order loops:

$$\begin{aligned} \hat{\dot{\theta}}(n) &= \hat{\dot{\theta}}(n-1) + K_{\theta i} Im\left\{u_0(n)(\hat{a}(n) + j\hat{b}(n))^*\right\} \\ \hat{\dot{\phi}}(n) &= \hat{\dot{\phi}}(n-1) + K_{\phi i} Im\left\{u_1(n)(\hat{c}(n) + j\hat{d}(n))^*\right\} \end{aligned} \tag{8.15}$$

where

$$u_0(n) = (r_0(n) - gt_1(n)e^{-j\hat{\phi}(n)})e^{-j\hat{\theta}(n)} = \tilde{r}_0(n)e^{-j\hat{\theta}(n)} \tag{8.16}$$

represents the phase corrected estimation of the main polarization received symbol, and $u_1(n) = -gt_1(n)e^{-j\hat{\phi}(n)}$ is the phase corrected estimation of the cross polar interference signal, according to (8.2). $K_{\theta i}$, $K_{\phi i}$ are the integral gains which control the convergence rate of the frequency estimation algorithm and correspond to the integral loop parameter of a second-order PLL. $Im\{.\}$ is the imaginary part of its argument,

while the symbol * represents the complex conjugate.

Equation (8.15) is equivalent to a first-order PLL, so it has a lower performance compared to the complete two-state Kalman model described in Sec. 8.3. Anyway, the complexity reduction makes its implementation simpler than a two-state Kalman scheme and comparable with a more common second-order PLL solution.

The state equations for the one-state Kalman filter approach are given as follows in (8.17), (8.18):

$$\begin{aligned} \hat{\theta}(n|n) &= \hat{\theta}(n|n-1) + \mathbf{K}_\theta \left(\mathbf{r}_0(n) - \mathbf{h}_0(n)\right) \\ \hat{\phi}(n|n) &= \hat{\phi}(n|n-1) + \mathbf{K}_\phi \left(\mathbf{r}_1(n) - \mathbf{h}_1(n)\right) \end{aligned} \tag{8.17}$$

$$\begin{aligned} \hat{\theta}(n+1|n) &= \hat{\theta}(n|n) + \hat{\dot{\theta}}(n) \\ \hat{\phi}(n+1|n) &= \hat{\phi}(n|n) + \hat{\dot{\phi}}(n) \end{aligned} \tag{8.18}$$

where $\mathbf{K}_\theta(n)$, $\mathbf{K}_\phi(n)$ are the Kalman gains, while the errors are defined according to the equations (8.12).

The one-state EKF may be derived according to

$$\begin{aligned} \mathbf{H}_0(n) &= \frac{\delta \mathbf{h}_0}{\delta x_0}|_{x_0=\hat{\theta}(n|n-1)} = \\ &= \begin{bmatrix} -\hat{a}(n)\sin(\hat{\theta}(n|n-1)) - \hat{b}(n)\cos(\hat{\theta}(n|n-1)) \\ -\hat{b}(n)\sin(\hat{\theta}(n|n-1)) + \hat{a}(n)\cos(\hat{\theta}(n|n-1)) \end{bmatrix} \end{aligned} \tag{8.19}$$

$$\mathbf{H}_1(n) = \frac{\delta \mathbf{h}_1}{\delta x_1}|_{x_1=\hat{\phi}(n|n-1)} =$$

$$= \begin{bmatrix} -\hat{c}(n)\sin(\hat{\phi}(n|n-1)) - \hat{d}(n)\cos(\hat{\phi}(n|n-1)) \\ -\hat{d}(n)\sin(\hat{\phi}(n|n-1)) + \hat{c}(n)\cos(\hat{\phi}(n|n-1)) \end{bmatrix} \tag{8.20}$$

One-State Model with Reduced Observations

Following the same approach in [126], it is possible to further reduce the implementation complexity by only considering the in-phase or the in-quadrature component in the two-dimensional equations (8.12,8.17,8.19,8.20).

8.4.2 Alternative Error Detection Computation

In the following we formulate a new way of computing the minimized error in (8.17), as an alternative to the model proposed in [127], which provides the following main advantages:

- it saves a phase counter-rotation in (8.17) as shown in (8.21), which is usually hardware expensive;
- the one-state Kalman error is the same residual phase error used to drive the frequency estimations in (8.15) which can be computed once for both the algorithms at each symbol time, thus saving computational operations.

The Kalman errors in (8.17) corresponds to

$$\begin{aligned} e_0(n) &= \tilde{r}_0(n) - \hat{t}_0(n)e^{j\hat{\theta}(n)} \\ e_1(n) &= gt_1(n) - g\hat{t}_1(n)e^{j\hat{\phi}(n)} \end{aligned} \tag{8.21}$$

In the following, we consider only the new error computation $\epsilon_0(n)$ corresponding to the main polarization error $e_0(n)$, since the same procedure can be replicated for $e_1(n)$.

The new computed error $\epsilon_0(n)$ is equal to the difference between the phases of the input and output of the symbol slicer as expressed in (8.22).

$$\epsilon_0(n) = t_0(n)e^{-j\hat{\theta}(n)}(e^{j\theta(n)} - e^{j\hat{\theta}(n)}) \tag{8.22}$$

If we only consider the phase noise contribution at the output of the interference canceler, the input of the main polarization slicer $u_0(n)$ in (2) can be recomputed as follows

$$u_0(n) = \tilde{r}_0(n)e^{-j\hat{\theta}(n)} = t_0(n)e^{j(\theta(n)-\hat{\theta}(n))} \tag{8.23}$$

Defining $s_0(n)$ as in the following

$$\begin{aligned} s_0(n) &= \epsilon_0^*(n)u_0(n) = \\ &= |t_0(n)|^2 e^{-j\hat{\theta}(n)}(e^{-j\theta(n)} - e^{-j\hat{\theta}(n)})e^{j(\theta(n)-\hat{\theta}(n))} = \\ &= |t_0(n)|^2 \left(-2j\sin\left(\tfrac{\Delta\theta}{2}\right)\right) e^{\frac{\Delta\theta(n)}{2}} \end{aligned} \tag{8.24}$$

where $\Delta\theta(n) = \theta(n) - \hat{\theta}(n)$ represents the difference between the true phase and the estimated one, i.e. the phase error at the output of the slicer. $\Delta\theta(n)$ may be computed, as usual in digital PLL, as in (8.17).

Being $Im\left[u_0(n)\right] = -2\cos(\frac{\Delta\theta(n)}{2})\sin(\frac{\Delta\theta(n)}{2}) = -2\sin\left(\frac{\Delta\theta}{2}\right)$, $\mathbf{H}_0(n)$ may be computed as $\dfrac{\delta(u_0(n))}{\delta\theta}$ so that

$$\mathbf{H}_0(n) = \begin{bmatrix} -\hat{a}(n)\sin(\Delta\theta(n)) - \hat{b}(n)\cos(\Delta\theta(n)) \\ -\hat{b}(n)\sin(\Delta\theta(n)) + \hat{a}(n)\cos(\Delta\theta(n)) \end{bmatrix} \tag{8.25}$$

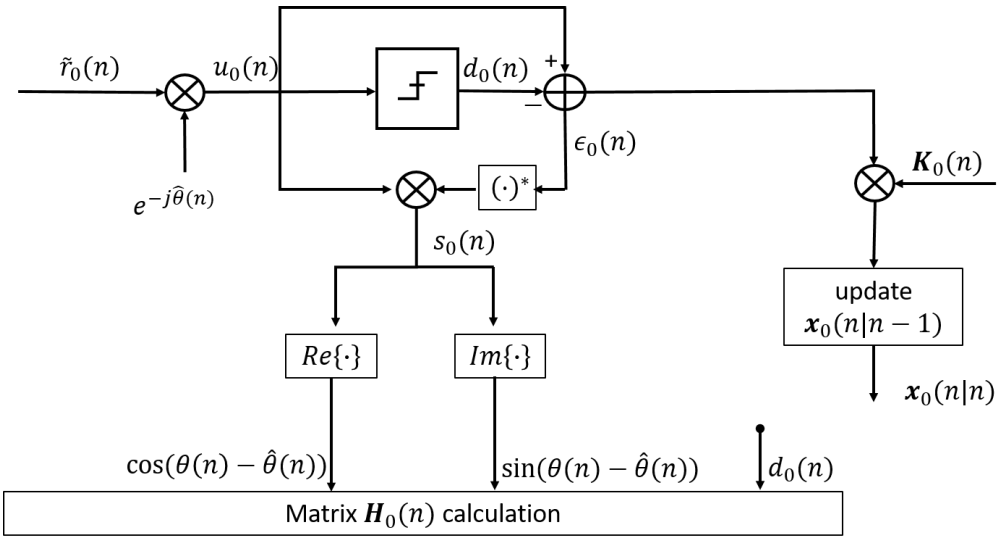

Figure 8.2: Kalman model with the alternative error detection

Similarly, it is possible to compute $\mathbf{H}_1(n)$ as follows

$$\mathbf{H}_1(n) = \begin{bmatrix} -\hat{c}(n)\sin(\Delta\phi(n)) - \hat{d}(n)\cos(\Delta\phi(n)) \\ -\hat{d}(n)\sin(\Delta\phi(n)) + \hat{c}(n)\cos(\Delta\phi(n)) \end{bmatrix} \tag{8.26}$$

As final remark, such alternative error detection computation has the benefit to avoid the hardware cost of a phase counter-rotation in (8.21).

Fig. 8.2 summarizes the steps described above.

8.4.3 EKF Algorithm with covariance matrix loop downsampling

Since the implementation of a Kalman filter for phase and frequency recovery is computationally expensive from an hardware point of view, we also consider a simplified approach where the covariance matrix computation loop is downsampled in time in order to speed up the algorithm and reduce its complexity.

Simulation results have shown that it is possible to keep almost the same performance by increasing the downsampling factor up to 64, for all the presented results.

8.4.4 Relation between the Extended Kalman approach and a digital PLL

In this section we analyze the relation between the Extended Kalman and PLL parameters, which is of more importance for the estimation of the PLL interference phase, since it is not possible to use a closed form solution in order to estimate them in a cross scheme. Indeed, it is possible to derive closed form solutions for PLL parameters optimization only for single-carrier architectures.

While [128] expresses the relation between Kalman filter and proportional-integral PLL, following a similar structures, we derive the relation (8.27) between the Extended Kalman version and PLL. Since we refer to an XPIC scheme, the equation considers both the main and cross polar component:

$$\begin{aligned} \begin{bmatrix} \alpha_{0p} \\ \alpha_{0i} \end{bmatrix} &= E[\mathbf{K}_0 \mathbf{H}_0] \\ \begin{bmatrix} \alpha_{1p} \\ \alpha_{1i} \end{bmatrix} &= E[\mathbf{K}_1 \mathbf{H}_1] \end{aligned} \tag{8.27}$$

where α_{0p} and α_{0i} are the proportional-integral PLL gains for the main component, α_{1p} and α_{1i} the cross polar component gains.

$\mathbf{K}_0$ and $\mathbf{K}_1$ are the Kalman gain matrices of the main and cross polar component, respectively. Finally, $\mathbf{H}_0$ and $\mathbf{H}_1$, calculated as in (8.25)-(8.26), are the contributions that account for the linearization of the EKF.

The calculation of the expected value converges in a few tens of symbols.

The reliability of the proposed method has been validated on the main path by using the closed form PLL equations, and by simulations for the cross-polar phase recovery path.

8.5 Simulation Results

8.5.1 Simulation Environment

For comparison purpose, we have considered the same simulation environment of [127]:

- a 1024-QAM modulation for both the main signal and the cross polar interferer;
- symbol rate equal to 25 MHz;
- phase noise parameters for both polarizations: -67 dBc/Hz at 10 KHz, -96 dBc/Hz at 100 KHz;
- the loop gains of the two PLLs, and the integral ones of the proposed scheme are set by using equations (8.27): $K_{\theta i} = \alpha_{0i}$, $K_{\phi i} = \alpha_{1i}$;
- periodical transmission of known constellation corner symbol pilots every 55 transmitted symbols.

As in [127], the phase noise parameters and the E_b/N_0 are used to compute the covariances of the noise signals $v_0(n)$, $v_1(n)$, $\mathbf{w}_0(n)$ and $\mathbf{w}_1(n)$.

8.5.2 BER Performance Evaluation

The bit error rate (BER) of the proposed reduced complexity Kalman based solutions are compared with both the two-state Kalman model and the second-order PLL one: the parameters of the second-order PLL and the Kalman algorithms are optimized for $Eb/N0 = 26$ dB and $XPD = 15$ dB.

Fig. 8.3,8.4 show that, despite their lower complexity, the developed one-state Kalman models show similar or even better performance than the typical PLL architecture. However, as expected, the two-state Kalman solution outperforms the

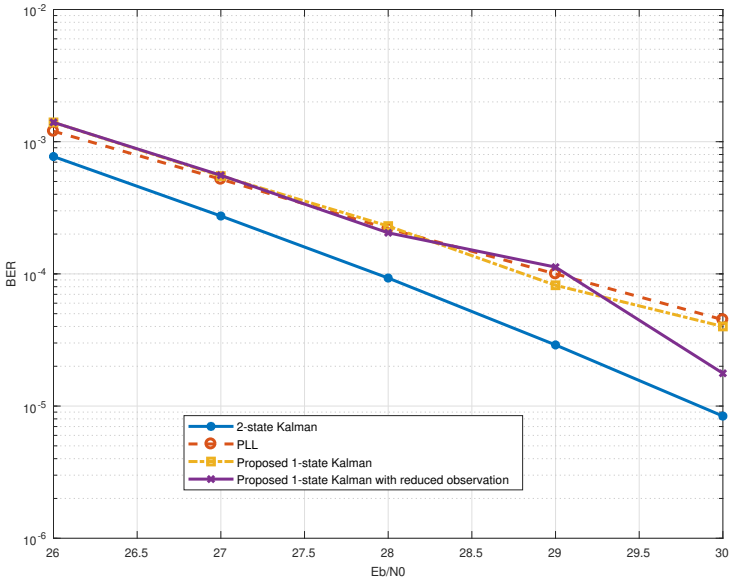

Figure 8.3: BER evaluation: 1024 QAM and XPD=15 dB. The parameters of all the algorithms are optimized for $XPD = 15$ dB, $E_b/N_0 = 26$ dB.

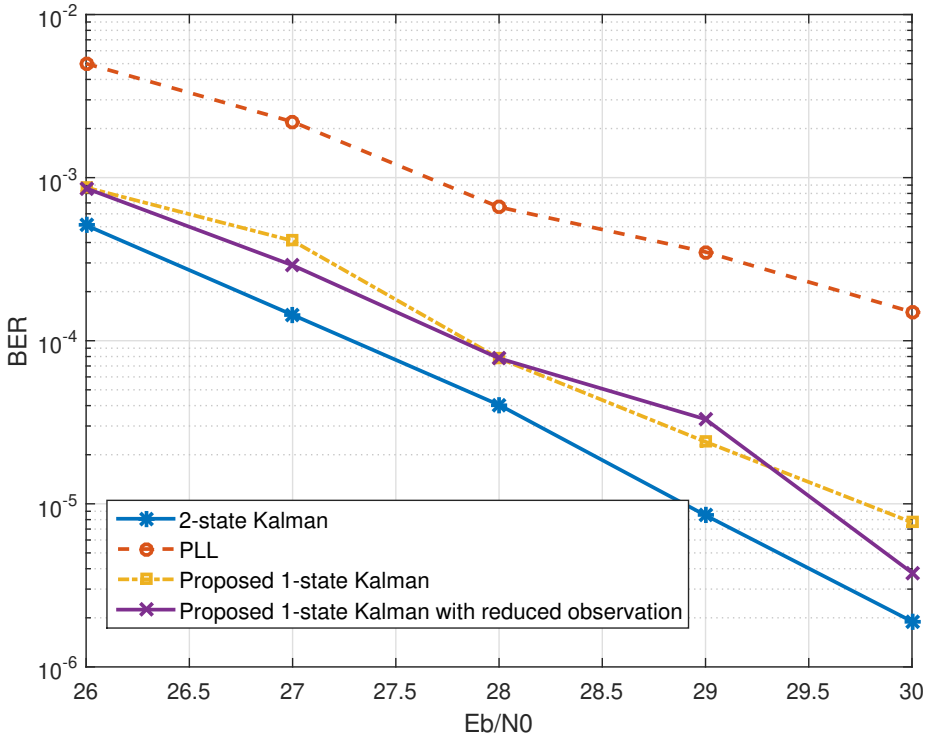

Figure 8.4: BER evaluation: 1024 QAM and $XPD = 25$ dB, while the parameters of all the algorithms are optimized for $XPD = 15$ dB, $E_b/N_0 = 26$ dB.

one-state algorithms, at the cost of higher complexity. Going in more details, Fig. 8.3 illustrates the BER when the gains of both Kalman and PLL solutions are optimized for known value of the interference parameter $XPD = 15$ dB, i. e. it is assumed no mismatch between such parameter estimation and its real value. Under this condition, the proposed one-state Kalman solutions perform slightly better than the common second-order PLL. Moreover, as shown in Fig. 8.4, the proposed algorithms are less sensitive to carrier-to-interference variations. Indeed, when the real XPD value is different from the one used to optimize the algorithm parameters as in Fig. 8.4, both the proposed one-state Kalman versions perform much better than the commonly used second-order PLL scheme.

8.5.3 Computational Complexity Evaluation

Table 8.1 illustrates the different matrix dimensions of the Kalman based solutions to show a computational complexity comparison.

Table 8.1: Computational complexity comparison in terms of matrix dimensions in Kalman based solutions.

Matrix	2-state Kalman	1-state Kalman	1-state Kalman with reduced observation
$\mathbf{H}$	2x2	1x2	1x1
$\mathbf{K}$	2x2	2x1	1x1
$\mathbf{Q}_v$	2x2	1x1	1x1
$\mathbf{Q}_w$	2x2	1x1	1x1
$\mathbf{R}$	2x2	2x2	1x1
$\mathbf{F}$	2x2	1x1	1x1

Furthermore, Fig. 8.5-8.7 compare the complexity of Kalman based solutions showing the computational times needed to calculate the Kalman gains $\mathbf{K}$, the covariance matrix $\mathbf{R}$, and the innovation covariance inverse $\mathbf{S}^{-1}$, respectively. Indeed, the computation of such variables represents the most expensive operation for EKF algorithms, due to the Jacobian matrices of equations (8.25-8.26). Fig. 8.5-8.7 con-

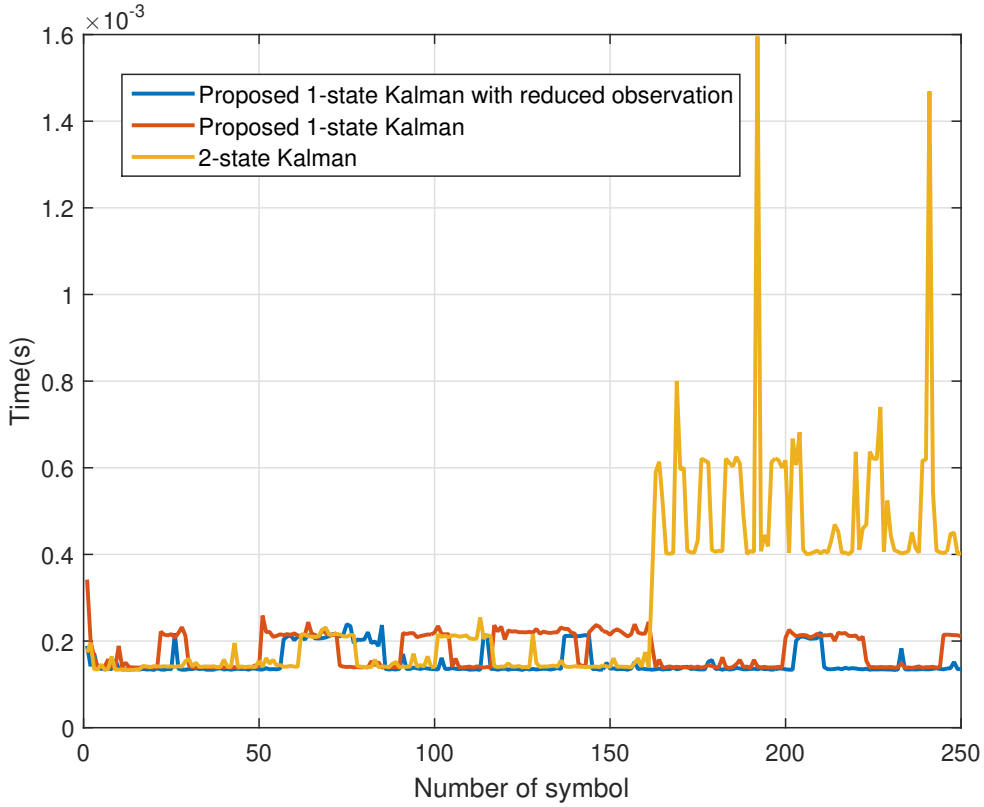

Figure 8.5: Simulation time comparison for the Kalman gains **K** calculation: 2-state Kalman, 1-state Kalman and 1-state Kalman with reduced observation.

firm that both the proposed one-state Kalman model and its one-state version with reduced observation require less computation time compared to the two-state scheme. In particular, the one-state scheme with reduced observation demands the minimum computation time since all the Kalman parameters become scalars. As shown in Fig. 8.3-8.4 such advantage of the proposed one-state model solutions is achieved at the cost of lower performance compared to the two-state Kalman approach. However, their performance are comparable and even better of the commonly used second-order PLL scheme.

8.5.4 Performance Evaluation of the downsampling covariance matrix

As reported in the previous Sec. 8.4.3, hardware complexity can be further reduced by not updating the covariance matrix $\mathbf{R}(n)$ at each step without degrading the

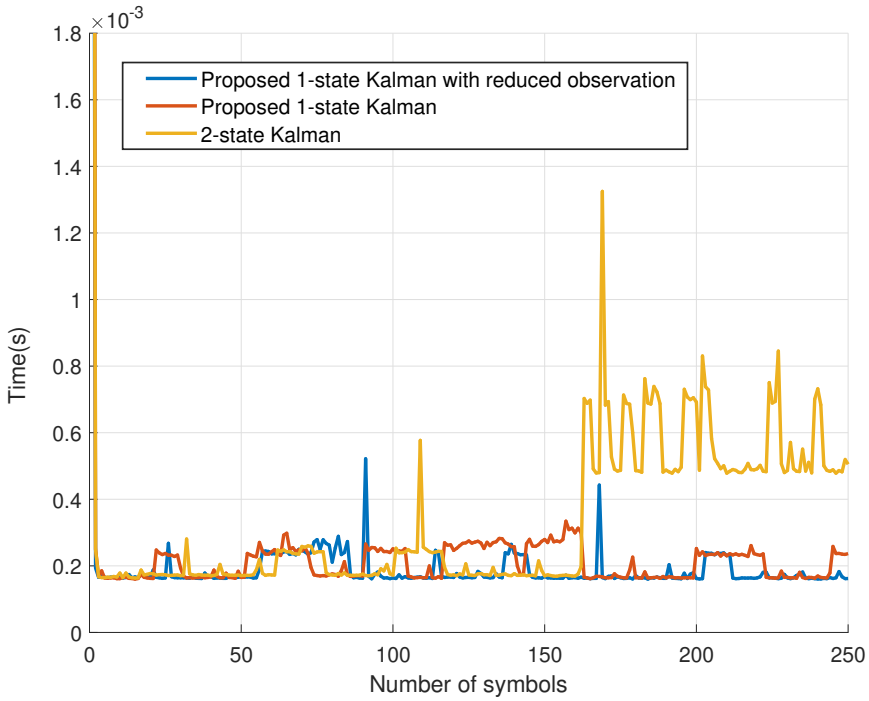

Figure 8.6: Simulation time comparison for the innovation covariance matrix inverse $\boldsymbol{S}^{-1}$ calculation: 2-state Kalman, 1-state Kalman and 1-state Kalman with reduced observation.

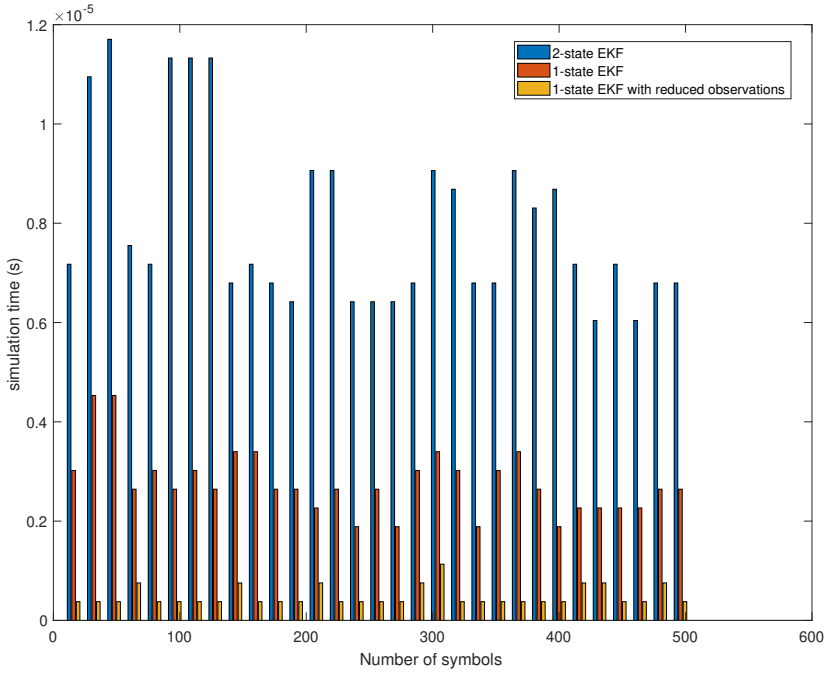

Figure 8.7: Simulation time comparison for the Error Covariance matrix $\mathbf{R}$ calculation (Measurement update equation): 2-state Kalman, 1-state Kalman and 1-state Kalman with reduced observation.

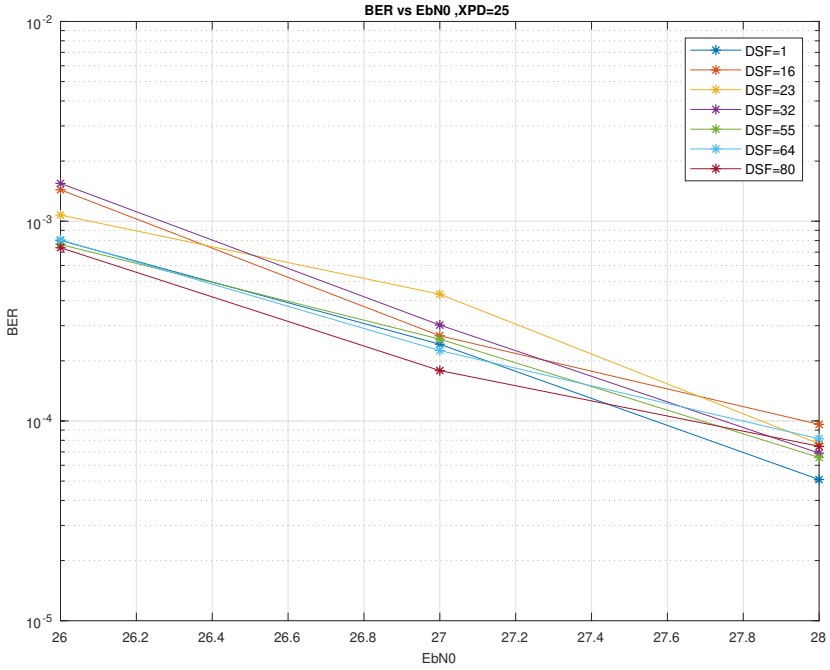

Figure 8.8: BER for 1-state Kalman with different DSF, pilot interval=56, $XPD = 25$ dB.

performance as shown in the following. Fig. 8.8 illustrates the BER performance of the proposed one-state Kalman for different downsampling factors (DSFs), showing that the algorithm works well also for high DSF values.

Being the concept of downsampling applicable also to other algorithms, in Fig. 8.9-8.15, a comprehensive analysis has been performed for the two-state Kalman model with different DSFs, pilot intervals. Fig. 8.9 shows the BER performance for different DSFs, with a pilot separation distance equal to 56, while the pilot separation is 64 in Fig. 8.10.

As expected, comparing Fig. 8.9 and 8.10, the best results are obtained with a lower pilot separation distance equal to 56 symbols as in Fig. 8.9. Anyway, in both figures the scheme still show good performance till the highest value $DSF = 80$.

Fig. 8.11 illustrates BER performance for higher DSF values showing that a DSF greater than 80 produces some unstable behavior in the system, so that, under

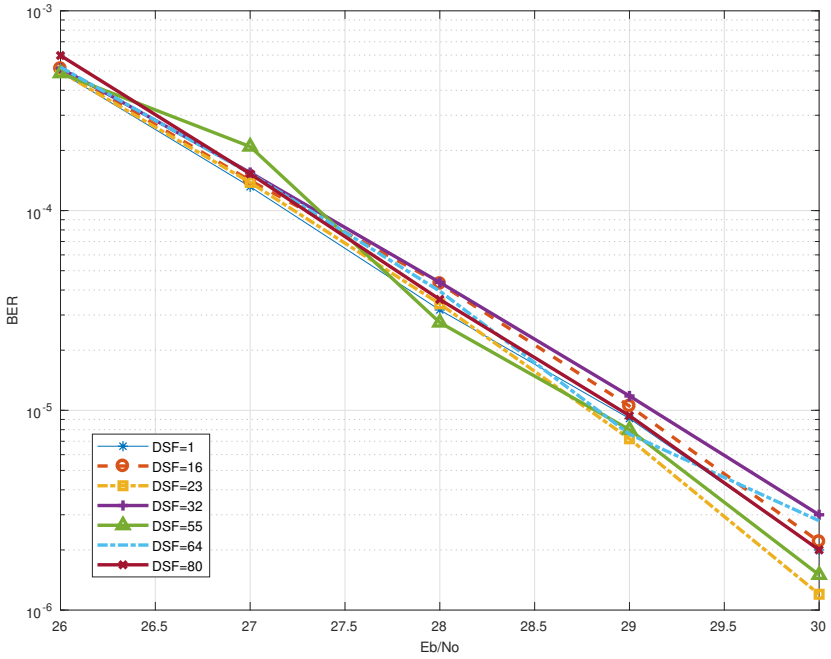

Figure 8.9: BER for 2-state Kalman with different DSF, Pilot interval=56, $XPD = 25$ dB.

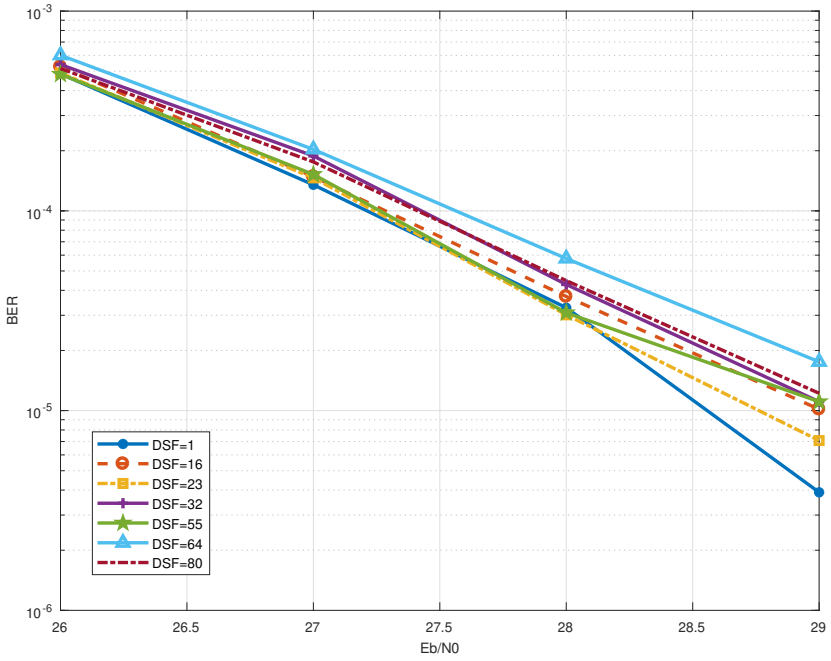

Figure 8.10: BER for 2-state Kalman with different DSF, Pilot interval=64, $XPD = 25$ dB.

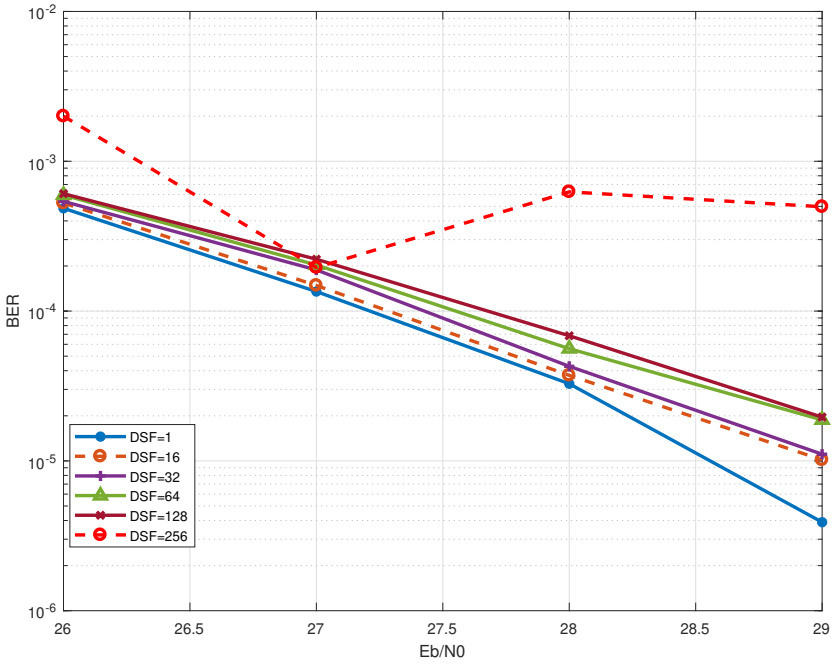

Figure 8.11: BER for 2-state Kalman with different DSF, pilot interval= 56, $XPD =$ 25 dB.

this channel condition, $DSF = 80$ could be considered as a performance upper limit.

Finally in the following Fig. 8.12-8.15, we show BER performance when changing the modulation order. Instead of using a 1024-QAM scheme as in all the previous results, Fig. 8.12-8.15 consider 64-QAM and 256-QAM for both $XPD = 15$ dB and $XPD = 25$ dB, showing more stable performance compared to the 1024 order when increasing the downsampling factor.

8.6 Conclusion

In this work we have considered a cross-polarized communications system based on two independent transceiver chains, in order to have the maximum flexibility from an installation and maintenance point of view, to connect different single carrier transceivers to dual-polarized antennas. A new solution has been proposed to recover

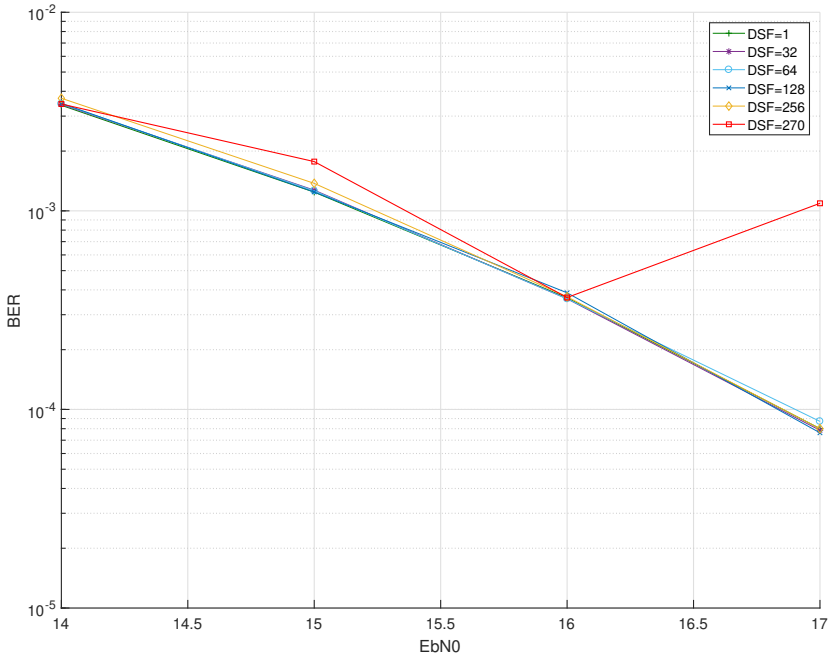

Figure 8.12: BER for 2-state Kalman with different DSF. 64-QAM, $XPD = 15$ dB, pilot interval=56.

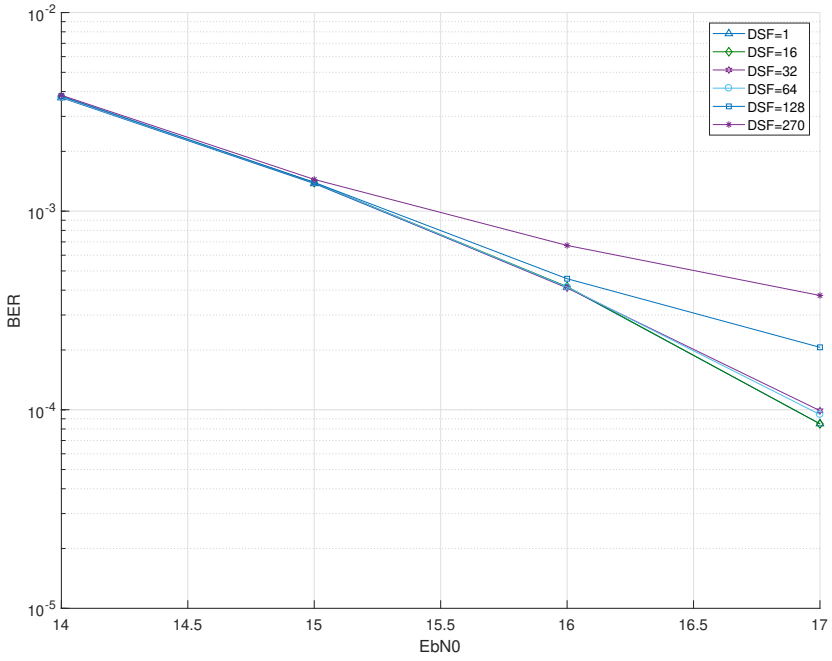

Figure 8.13: BER for 2-state Kalman with different DSF. 64-QAM, $XPD = 25$ dB, pilot interval=56.

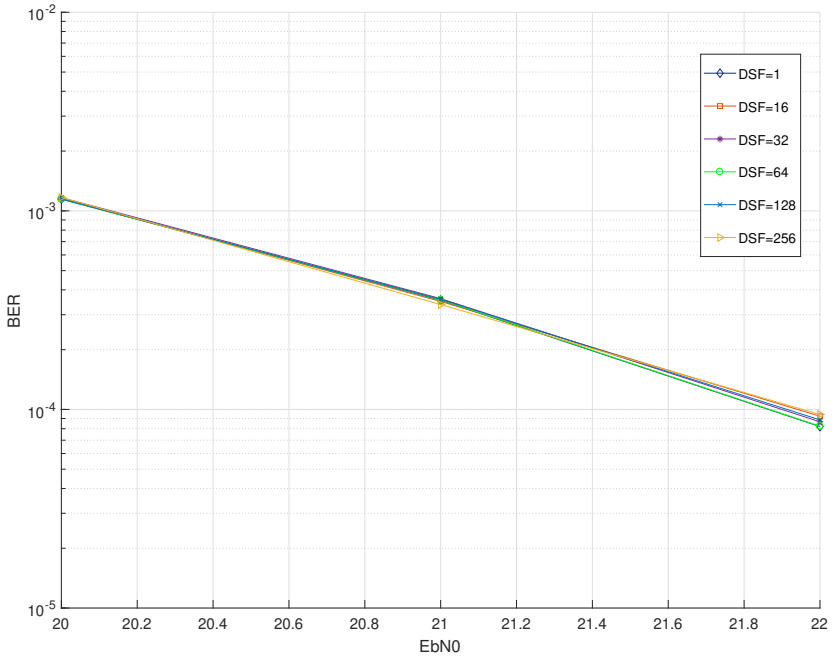

Figure 8.14: BER for 2-state Kalman with different DSF. 256-QAM, $XPD = 15$ dB, pilot interval=56.

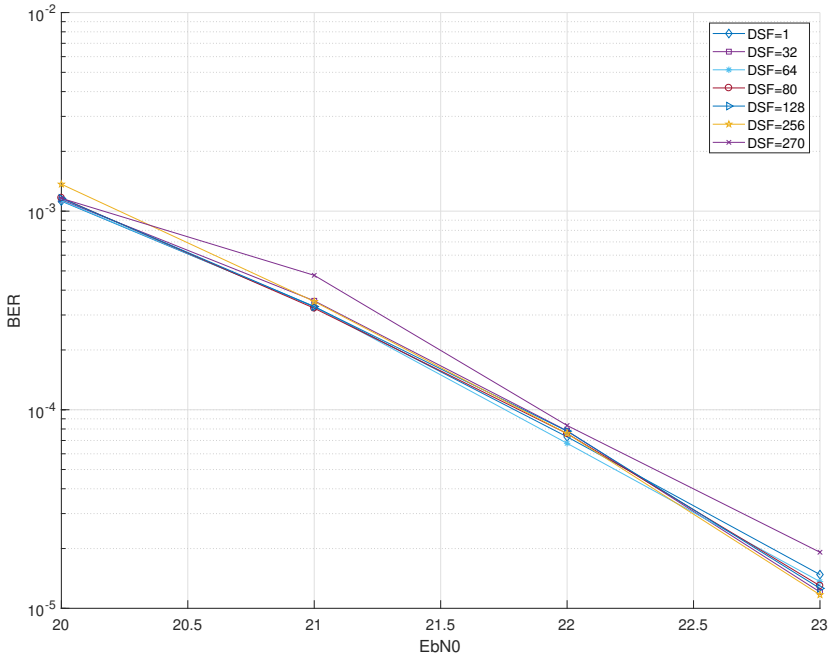

Figure 8.15: BER for 2-state Kalman with different DSF. 256-QAM, $XPD = 25$ dB, pilot interval=56.

the phase of the two horizontal and vertical signals on the cross-polar radio links by exploiting a reduced complexity one-state Kalman filter. Moreover, an alternative error detection computation and the covariance matrix loop downsampling have been proposed. Simulations results prove the effectiveness of the proposed reduced complexity Kalman based solutions, whose main benefit is to directly adapt its parameters according to new channel noise and interference conditions showing better performance of the commonly used second-order PLL scheme. Indeed, the commonly used PLL solution needs to optimize and re-set its parameters each time. On this purpose, we have also developed a relation between the EKF filter and PLL scheme envisioning a solution where a Kalman based algorithm optimizes off-line the PLL parameters for the cross-polar interference canceler. Since the proposed complexity reduction schemes may be applied not onlyto the EKF, but also to the other types of Kalman algorithms, such as the unscented filter [129], as future works we are going to address other Kalman architectures as well as hardware experimental results.

References

[1] A. Liu and V. K. N. Lau, "Exploiting base station caching in mimo cellular networks: Opportunistic cooperation for video streaming," *IEEE Transactions on Signal Processing*, vol. 63, no. 1, pp. 57–69, 2015.

[2] W. Li, G. Chen, E. Blasch, and R. Lynch, "Cognitive mimo sonar based robust target detection for harbor and maritime surveillance applications," in *2009 IEEE Aerospace conference*, IEEE, 2009, pp. 1–9.

[3] S. Banou, M. Swaminathan, G. R. Muns, D. Duong, F. Kulsoom, P. Savazzi, A. Vizziello, and K. R. Chowdhury, "Beamforming galvanic coupling signals for iomt implant-to-relay communication," *IEEE Sensors Journal*, pp. 1–1, 2018.

[4] E. Björnson, E. Jorswieck, *et al.*, "Optimal resource allocation in coordinated multi-cell systems," *Foundations and Trends® in Communications and Information Theory*, vol. 9, no. 2–3, pp. 113–381, 2013.

[5] X. Gao, "Doctoral thesis: Massive mimo in real propagation environments," Defence details Date: 2016-02-18 , Lund University, Faculty of Engineering LTH, Lund., PhD thesis, Department of Electrical and Information Technology, Jan. 2016, ISBN: 978-91-7623-646-8.

[6] C. R. Berger, Z. Wang, J. Huang, and S. Zhou, "Application of compressive sensing to sparse channel estimation," *IEEE Communications Magazine*, vol. 48, no. 11, pp. 164–174, 2010.

[7] X. Rao and V. K. N. Lau, "Distributed compressive csit estimation and feedback for fdd multi-user massive mimo systems," *IEEE Transactions on Signal Processing*, vol. 62, no. 12, pp. 3261–3271, 2014.

[8] Y. Zhou, M. Herdin, A. M. Sayeed, and E. Bonek, "Experimental study of mimo channel statistics and capacity via virtual channel representation," 2006.

[9] S. Higuchi and C.-J. Ahn, "Reduced complexity and latency for a massive mimo system using a parallel detection algorithm," *ICT Express*, vol. 3, no. 3, pp. 119 –123, 2017.

[10] E. G. Larsson, O. Edfors, F. Tufvesson, and T. L. Marzetta, "Massive mimo for next generation wireless systems," *IEEE Communications Magazine*, vol. 52, no. 2, pp. 186–195, Feb. 2014.

[11] T. L. Marzetta, "Noncooperative cellular wireless with unlimited numbers of base station antennas," *IEEE Transactions on Wireless Communications*, vol. 9, no. 11, pp. 3590–3600, 2010.

[12] F. Rusek, D. Persson, B. K. Lau, E. G. Larsson, T. L. Marzetta, O. Edfors, and F. Tufvesson, "Scaling up mimo: Opportunities and challenges with very large arrays," *IEEE Signal Processing Magazine*, vol. 30, no. 1, pp. 40–60, 2013.

[13] P. W. C. Chan, E. S. Lo, R. R. Wang, E. K. S. Au, V. K. N. Lau, R. S. Cheng, W. H. Mow, R. D. Murch, and K. B. Letaief, "The evolution path of 4g networks: Fdd or tdd?" *IEEE Communications Magazine*, vol. 44, no. 12, pp. 42–50, 2006.

[14] Y. Ding and B. D. Rao, "Dictionary learning-based sparse channel representation and estimation for fdd massive mimo systems," *IEEE Transactions on Wireless Communications*, vol. 17, no. 8, pp. 5437–5451, 2018.

[15] A. K. Teshome, B. Kibret, and D. T. H. Lai, "Galvanically coupled intrabody communications for medical implants: A unified analytic model," *IEEE Transactions on Antennas and Propagation*, vol. 64, no. 7, pp. 2989–3002, 2016.

[16] S. Banou, M. Swaminathan, G. Reus Muns, D. Duong, F. Kulsoom, P. Savazzi, A. Vizziello, and K. R. Chowdhury, "Beamforming galvanic coupling signals for iomt implant-to-relay communication," *IEEE Sensors Journal*, vol. 19, no. 19, pp. 8487–8501, 2019.

[17] F. Kulsoom, A. Vizziello, H. N. Chaudhry, and P. Savazzi, "Pilot reduction techniques for sparse channel estimation in massive mimo systems," in *2018 14th Annual Conference on Wireless On-demand Network Systems and Services (WONS)*, 2018, pp. 111–116.

[18] A. Vizziello, P. Savazzi, F. Kulsoom, G. Magenes, and P. Gamba, "A novel galvanic coupling testbed based on pc sound card for intra-body communication links," in *Body Area Networks: Smart IoT and Big Data for Intelligent Health Management*, L. Mucchi, M. Hämäläinen, S. Jayousi, and S. Morosi, Eds., Cham: Springer International Publishing, 2019, pp. 135–149, ISBN: 978-3-030-34833-5.

[19] F. Kulsoom, A. Vizziello, R. Borra, and P. Savazzi, "Reduced complexity kalman filtering for phase recovery in xpic systems," *Physical Communication*, vol. 29, pp. 112 –119, 2018.

[20] A. Grami, "Chapter 12 - wireless communications," in *Introduction to Digital Communications*, A. Grami, Ed., Boston: Academic Press, 2016, pp. 493 –527, ISBN: 978-0-12-407682-2.

[21] M. Debbah and R. R. Muller, "Mimo channel modeling and the principle of maximum entropy," *IEEE Transactions on Information Theory*, vol. 51, no. 5, pp. 1667–1690, 2005.

[22] A. G. Burr, "Capacity bounds and estimates for the finite scatterers mimo wireless channel," *IEEE Journal on Selected Areas in Communications*, vol. 21, no. 5, pp. 812–818, 2003.

[23] A. M. Sayeed, "Deconstructing multiantenna fading channels," *IEEE Transactions on Signal Processing*, vol. 50, no. 10, pp. 2563–2579, 2002.

[24] G. T. 25.996, "Universal mobile telecommunications system (umts); spatial channel model for multiple input multiple output (mimo) simulations (3gpp tr 25.996 version 11.0.0 release 11) intellectual property rights."

[25] `http://www.lx.it.pt/cost273`.

[26] V. Erceg, K. V. S. Hari, M. S. Smith, D. S. Baum, K. P. Sheikh, C. Tappenden, J. M. Costa, C. Bushue, A. Sarajedini, and R. Schwartz, *"channel models for fixed wireless applications"*, Contribution IEEE 802.16.3c-01/29r4 and IEEE 802.16 Broadband Wireless Access Working Group.

[27] L. S. V. Erceg, A. M. P. Kyritsi, D. S. Baum, A. Y. Gorokhov, C. Oestges, Q. Li, K. Yu, N. Tal, B. D. Dijkstra, C. L. A. Jagannatham, V. J. Rhodes, J. Medbo, D. Michelson, and M. Webster.

[28] N. Fatema, G. Hua, Y. Xiang, D. Peng, and I. Natgunanathan, "Massive mimo linear precoding: A survey," *IEEE Systems Journal*, vol. 12, no. 4, pp. 3920–3931, 2018.

[29] A. Kammoun, A. Müller, E. Björnson, and M. Debbah, "Linear precoding based on polynomial expansion: Large-scale multi-cell mimo systems," *IEEE Journal of Selected Topics in Signal Processing*, vol. 8, no. 5, pp. 861–875, 2014.

[30] E. J. Candes and M. B. Wakin, "An introduction to compressive sampling," *IEEE Signal Processing Magazine*, vol. 25, no. 2, pp. 21–30, 2008.

[31] E. J. Candes and T. Tao, "Decoding by linear programming," *IEEE Transactions on Information Theory*, vol. 51, no. 12, pp. 4203–4215, 2005.

[32] M. Rudelson and R. Vershynin, "Sparse reconstruction by convex relaxation: Fourier and gaussian measurements," in *2006 40th Annual Conference on Information Sciences and Systems*, 2006, pp. 207–212.

[33] D. L. Donoho, "Compressed sensing," *IEEE Transactions on Information Theory*, vol. 52, no. 4, pp. 1289–1306, Apr. 2006.

[34] M. D. T. Blumensath, "Iterative hard thresholding for compressed sensing," 265–274 Anal. 27 (3), 2009.

[35] T. Blumensath, "Accelerated iterative hard thresholding," *Signal Processing*, vol. 92, no. 3, pp. 752 –756, 2012.

[36] S. Foucart, "Hard thresholding pursuit: An algorithm for compressive sensing," 2543–2563 Volume 49 Issue 6, Nov. 2011.

[37] W. Huang, Y. Huang, W. Xu, and L. Yang, "Beam-blocked channel estimation for fdd massive mimo with compressed feedback," *IEEE Access*, vol. 5, pp. 11 791–11 804, 2017.

[38] H. Schepker and A. Dekorsy, "Compressive sensing multi-user detection with block-wise orthogonal least squares," in *2012 IEEE 75th Vehicular Technology Conference: VTC2012-Spring*, Yokohama, Japan, 2012.

[39] Z. Zhou, X. Chen, D. Guo, and M. L. Honig, "Sparse channel estimation for massive mimo with 1-bit feedback per dimension," in *2017 IEEE Wireless Communications and Networking Conference (WCNC)*, 2017, pp. 1–6.

[40] Y. Barbotin, A. Hormati, S. Rangan, and M. Vetterli, "Estimation of sparse mimo channels with common support," *IEEE Transactions on Communications*, vol. 60, no. 12, pp. 3705–3716, 2012.

[41] E. G. Larsson, O. Edfors, F. Tufvesson, and T. L. Marzetta, "Massive mimo for next generation wireless systems," *IEEE Communications Magazine*, vol. 52, no. 2, pp. 186–195, Feb. 2014.

[42] F. Rusek, D. Persson, B. K. Lau, E. G. Larsson, T. L. Marzetta, O. Edfors, and F. Tufvesson, "Scaling up mimo: Opportunities and challenges with very large arrays," *IEEE Signal Processing Magazine*, vol. 30, no. 1, pp. 40–60, Jan. 2013.

[43] O. E. Ayach, S. Rajagopal, S. Abu-Surra, Z. Pi, and R. W. Heath, "Spatially sparse precoding in millimeter wave mimo systems," *IEEE Transactions on Wireless Communications*, vol. 13, no. 3, pp. 1499–1513, Mar. 2014.

[44] X. Rao and V. K. N. Lau, "Distributed compressive csit estimation and feedback for fdd multi-user massive mimo systems," *IEEE Transactions on Signal Processing*, vol. 62, no. 12, pp. 3261–3271, Jun. 2014.

[45] Y. Ding and B. D. Rao, "Compressed downlink channel estimation based on dictionary learning in fdd massive mimo systems," in *2015 IEEE Global Communications Conference (GLOBECOM)*, Dec. 2015, pp. 1–6.

[46] A. N. Uwaechia and N. M. Mahyuddin, "A review on sparse channel estimation in ofdm system using compressed sensing," *IETE Technical Review*, vol. 34, no. 5, pp. 514–531, 2017.

[47] M. Masood and T. Y. Al-Naffouri, "Sparse reconstruction using distribution agnostic bayesian matching pursuit," *IEEE Transactions on Signal Processing*, vol. 61, no. 21, pp. 5298–5309, 2013.

[48] W. Dai and O. Milenkovic, "Subspace pursuit for compressive sensing signal reconstruction," *IEEE Transactions on Information Theory*, vol. 55, no. 5, pp. 2230–2249, May 2009.

[49] D. L. Donoho, Y. Tsaig, I. Drori, and J. L. Starck, "Sparse solution of underdetermined systems of linear equations by stagewise orthogonal matching pursuit," *IEEE Transactions on Information Theory*, vol. 58, no. 2, pp. 1094–1121, Feb. 2012.

[50] J. T. D. Needell, "Cosamp: Iterative signal recovery from incomplete and inaccurate samples," 301–321 Anal. 26 (3), 2009.

[51] J. Wang, S. Kwon, and B. Shim, "Generalized orthogonal matching pursuit," *IEEE Transactions on Signal Processing*, vol. 60, no. 12, pp. 6202–6216, Dec. 2012.

[52] F. Salahdine, N. Kaabouch, and H. E. Ghazi, "A survey on compressive sensing techniques for cognitive radio networks," *Physical Communication*, vol. 20, pp. 61 –73, 2016.

[53] R. Jani and Y. Sharma, "A review on spectrum sensing for cognitive radio networks," in *Int. J. Adv. Eng. Res. Dev. 1 (5)*, 2014, pp. 5–8.

[54] R. V. N. Deanna J. Tropp, "Greedy signal recovery review," in *IEEE Conf. Signals Syst. Computers*, 2008.

[55] J. W. Choi, B. Shim, and S. H. Chang, "Downlink pilot reduction for massive mimo systems via compressed sensing," *IEEE Communications Letters*, vol. 19, no. 11, pp. 1889–1892, Nov. 2015.

[56] G. Coluccia, C. Ravazzi, and E. Magli", *"Compressed Sensing for Distributed Systems"*. published in Springer, Singapore, 2015, "chapter 2".

[57] Y. Xu, G. Yue, and S. Mao, "User grouping for massive mimo in fdd systems: New design methods and analysis," *IEEE Access*, vol. 2, pp. 947–959, 2014.

[58] M. Duarte, S Sarvotham, M B Wakin, D. Baron, and R G Baraniuk, "Joint sparsity models for distributed compressed sensing," *Online Proceedings of the Workshop on Signal Processing with Adaptive Sparse Structured Representations (SPARS)*, Jan. 2005.

[59] D. Baron, M. F. Duarte, M. B. Wakin, S. Sarvotham, and R. G. Baraniuk, "Distributed compressive sensing," *arXiv preprint arXiv:0901.3403*, 2009.

[60] Z. Gao, L. Dai, Z. Wang, and S. Chen, "Spatially common sparsity based adaptive channel estimation and feedback for fdd massive mimo," *IEEE Transactions on Signal Processing*, vol. 63, no. 23, pp. 6169–6183, 2015.

[61] K. S. Hassan, M. Kurras, and L. Thiele, "Performance of distributed compressive sensing channel feedback in multi-user massive mimo," in *2015 IEEE 11th International Conference on Wireless and Mobile Computing, Networking and Communications (WiMob)*, 2015, pp. 430–436.

[62] J. Choi, D. J. Love, and U. Madhow, "Limited feedback in massive mimo systems: Exploiting channel correlations via noncoherent trellis-coded quantization," in *2013 47th Annual Conference on Information Sciences and Systems (CISS)*, 2013, pp. 1–6.

[63] T. Inoue and R. W. Heath, "Geodesic prediction for limited feedback multiuser mimo systems in temporally correlated channels," in *2009 IEEE Radio and Wireless Symposium*, 2009, pp. 167–170.

[64] A. A. Esswie, M. El-Absi, O. A. Dobre, S. Ikki, and T. Kaiser, "Spatial channel estimation-based FDD-MIMO interference alignment systems," *IEEE Wireless Communications Letters*, vol. 6, no. 2, pp. 254–257, 2017.

[65] A. N. Uwaechia and N. M. Mahyuddin, "A review on sparse channel estimation in ofdm system using compressed sensing," *IETE Technical Review*, vol. 34, no. 5, pp. 514–531, 2017.

[66] A. Vizziello, I. F. Akyildiz, R. Agusti, L. Favalli, and P. Savazzi, "Cognitive radio resource management exploiting heterogeneous primary users," in *2011 IEEE Global Telecommunications Conference - GLOBECOM 2011*, 2011, pp. 1–5.

[67] A. Vizziello, I. F. Akyildiz, R. Agustí, L. Favalli, and P. Savazzi, "Characterization and exploitation of heterogeneous ofdm primary users in cognitive radio networks," *Wireless Networks*, vol. 19, no. 6, pp. 1073–1085, 2013.

[68] W. Y. B. O. D. Y. Mohydeen A Chargé P, "Spatially correlated sparse mimo channel path delay estimation in scattering environments based on signal subspace tracking," *Sensors (Basel)*, vol. 18(5):1451, 2018.

[69] R. Zhang, C. C. Chai, and Y. Liang, "Joint beamforming and power control for multiantenna relay broadcast channel with qos constraints," *IEEE Transactions on Signal Processing*, vol. 57, no. 2, pp. 726–737, 2009.

[70] J. Dai, A. Liu, and V. K. N. Lau, "Joint channel estimation and user grouping for massive mimo systems," *IEEE Transactions on Signal Processing*, vol. 67, no. 3, pp. 622–637, 2019.

[71] R. Alesii, P. D. Marco, F. Santucci, P. Savazzi, R. Valentini, and A. Vizziello, "Multi-reader multi-tag architecture for uwb/uhf radio frequency identification systems," in *2015 International EURASIP Workshop on RFID Technology (EURFID)*, 2015, pp. 28–35.

[72] S. Foucart and H. Rauhut, "A mathematical introduction to compressive sensing," *Bull. Am. Math*, vol. 54, pp. 151–165, 2017.

[73] Y. Ding and B. D. Rao, "Compressed downlink channel estimation based on dictionary learning in fdd massive mimo systems," in *2015 IEEE Global Communications Conference (GLOBECOM)*, 2015, pp. 1–6.

[74] J. Huang, T. Zhang, and D. Metaxas, "Learning with Structured Sparsity," *arXiv e-prints*, arXiv:0903.3002, arXiv:0903.3002, 2009. arXiv: `0903.3002 [stat.ME]`.

[75] L. Bottou and N. Murata, "Stochastic approximations and efficient learning," *The Handbook of Brain Theory and Neural Networks, Second edition,. The MIT Press, Cambridge, MA*, 2002.

[76] A. F. Molisch, A. Kuchar, J. Laurila, K. Hugl, and R. Schmalenberger, "Geometry-based directional model for mobile radio channels - principles and implementation," *European Transactions on Telecommunications*, vol. 14, pp. 351–359, 2003.

[77] W. Shen, L. Dai, Y. Shi, B. Shim, and Z. Wang, "Joint channel training and feedback for fdd massive mimo systems," *IEEE Transactions on Vehicular Technology*, vol. 65, no. 10, pp. 8762–8767, 2016.

[78] J. A. Tropp, A. C. Gilbert, and M. J.Strauss, "Algorithms for simultaneous sparse approximation. part i: Greedy pursuit," *Signal Processing*, vol. 86, no. 3, pp. 572 –588, 2006, Sparse Approximations in Signal and Image Processing.

[79] J. Liang, Y. Liu, W. Zhang, Y. Xu, X. Gan, and X. Wang, "Joint compressive sensing in wideband cognitive networks," in *2010 IEEE Wireless Communication and Networking Conference*, 2010, pp. 1–5.

[80] W. Xu, Z. Li, Y. Tian, Y. Wang, and J. Lin, "Perturbation analysis of simultaneous orthogonal matching pursuit," *Signal Processing*, vol. 116, pp. 91 –100, 2015.

[81] Y. C. Pati, R. Rezaiifar, and P. S. Krishnaprasad, "Orthogonal matching pursuit: Recursive function approximation with applications to wavelet decomposition," in *Proceedings of 27th Asilomar Conference on Signals, Systems and Computers*, 1993, 40–44 vol.1.

[82] S. Sparrer and R. F. H. Fischer, "Soft-feedback omp for the recovery of discrete-valued sparse signals," in *2015 23rd European Signal Processing Conference (EUSIPCO)*, 2015, pp. 1461–1465.

[83] L. Jacques, J. N. Laska, P. T. Boufounos, and R. G. Baraniuk, "Robust 1-bit compressive sensing via binary stable embeddings of sparse vectors," *IEEE Transactions on Information Theory*, vol. 59, no. 4, pp. 2082–2102, 2013.

[84] E. Strickland, "Cyborgs go for gold," *IEEE Spectrum*, vol. 53, no. 1, pp. 30–33, 2016.

[85] M. Swaminathan, F. S. Cabrera, J. S. Pujol, U. Muncuk, G. Schirner, and K. R. Chowdhury, "Multi-path model and sensitivity analysis for galvanic coupled intra-body communication through layered tissue," *IEEE transactions on biomedical circuits and systems*, vol. 10, no. 2, pp. 339–351, 2016.

[86] K. Hoyt, B. Castaneda, and K. Parker, "5c-6 muscle tissue characterization using quantitative sonoelastography: Preliminary results," in *IEEE Ultrasonics Symposium*, 2007, pp. 365–368.

[87] P. Vecchia, R. Matthes, G. Ziegelberger, J. Lin, R. Saunders, and A. Swerdlow, "Exposure to high frequency electromagnetic fields, biological effects and health consequences (100 khz-300 ghz)," *International Commission on Non-Ionizing Radiation Protection*, 2009.

[88] I. S. Association *et al.*, *802.15. 6-2012 ieee standards for local and metropolitan area networks–part 15.6: Wireless body area networks*.

[89] C. Van Phan, Y. Park, H. Choi, J. Cho, and J. G. Kim, "An energy-efficient transmission strategy for wireless sensor networks," *Consumer Electronics, IEEE Transactions on*, vol. 56, no. 2, pp. 597–605, 2010.

[90] J.-Y. et al., "A mt-cdma based wireless body area network for ubiquitous healthcare monitoring," in *IEEE Biomedical Circuits and Systems Conference*, 2006, pp. 98–101.

[91] J. D. et al., "Energy-efficient distributed beamforming in uwb based implant body area networks," in *IEEE Vehicular Technology Conference (VTC)*, 2015, pp. 1–5.

[92] J. F. Alfaro, "A multi axial bioimplantable mems array bone stress sensor," PhD thesis, Citeseer, 2007.

[93] F. R. Andreuccetti D. and C. Petrucci, *An internet resource for the calculation of the dielectric properties of body tissues in the frequency range 10 hz - 100 ghz.*

[94] P. Strojnik and P. H. Peckham, "Implantable stimulators for neuromuscular control," *The Biomedical Engineering Handbook, 2nd edn. CRC Press LLC, Boca Raton*, 2000.

[95] M. Swaminathan, U. Muncuk, and K. R. Chowdhury, "Topology optimization for galvanic coupled wireless intra-body communication," in *IEEE INFOCOM 2016*, 2016, pp. 1–9.

[96] S. M. Mikki and Y. M. M. Antar, "A theory of antenna electromagnetic near field—part i," *IEEE Transactions on Antennas and Propagation*, vol. 59, no. 12, pp. 4691–4705, 2011.

[97] M. A. Davenport, P. T. Boufounos, M. B. Wakin, and R. G. Baraniuk, "Signal processing with compressive measurements," *IEEE Journal of Selected Topics in Signal Processing*, vol. 4, no. 2, pp. 445–460, 2010.

[98] A. Vizziello and P. Savazzi, "Efficient rfid tag identification exploiting hybrid uhf-uwb tags and compressive sensing," *IEEE Sensors Journal*, vol. 16, no. 12, pp. 4932–4939, 2016.

[99] E. van den Berg and M. P. Friedlander, "Probing the pareto frontier for basis pursuit solutions," *SIAM Journal on Scientific Computing*, vol. 31, no. 2, pp. 890–912, 2008.

[100] M. Seyedi, B. Kibret, D. T. H. Lai, and M. Faulkner, "A survey on intrabody communications for body area network applications," *IEEE Transactions on Biomedical Engineering*, vol. 60, no. 8, pp. 2067–2079, 2013.

[101] L. Galluccio, T. Melodia, S. Palazzo, and G. E. Santagati, "Challenges and implications of using ultrasonic communications in intra-body area networks," in *2012 9th Annual Conference on Wireless On-Demand Network Systems and Services (WONS)*, 2012, pp. 182–189.

[102] J. Park and P. P. Mercier, "Magnetic human body communication," in *2015 37th Annual International Conference of the IEEE Engineering in Medicine and Biology Society (EMBC)*, 2015, pp. 1841–1844.

[103] M. A. Callejón, J. Reina-Tosina, D. Naranjo-Hernández, and L. M. Roa, "Galvanic coupling transmission in intrabody communication: A finite element approach," *IEEE Transactions on Biomedical Engineering*, vol. 61, no. 3, pp. 775–783, 2014.

[104] M. Swaminathan, F. S. Cabrera, J. S. Pujol, U. Muncuk, G. Schirner, and K. R. Chowdhury, "Multi-path model and sensitivity analysis for galvanic coupled intra-body communication through layered tissue," *IEEE Transactions on Biomedical Circuits and Systems*, vol. 10, no. 2, pp. 339–351, 2016.

[105] M. Swaminathan, A. Vizziello, D. Duong, P. Savazzi, and K. R. Chowdhury, "Beamforming in the body: Energy-efficient and collision-free communication for implants," in *IEEE INFOCOM 2017 - IEEE Conference on Computer Communications*, 2017, pp. 1–9.

[106] M. S. Wegmueller, S. Huclova, J. Froehlich, M. Oberle, N. Felber, N. Kuster, and W. Fichtner, "Galvanic coupling enabling wireless implant communications," *IEEE Transactions on Instrumentation and Measurement*, vol. 58, no. 8, pp. 2618–2625, 2009.

[107] M. S. Wegmueller, M. Oberle, N. Felber, N. Kuster, and W. Fichtner, "Signal transmission by galvanic coupling through the human body," *IEEE Transactions on Instrumentation and Measurement*, vol. 59, no. 4, pp. 963–969, 2010.

[108] M. H. H. Seyedi and D. T. H. Lai, "A novel intrabody communication transceiver for biomedical applications," 2017.

[109] W. J. Tomlinson, K. R. Chowdhury, and C. Yu, "Galvanic coupling intra-body communication link for real-time channel assessment," in *2016 IEEE Conference on Computer Communications Workshops (INFOCOM WKSHPS)*, 2016, pp. 968–969.

[110] J. Hwang, "Innovative communication design lab based on pc sound card and matlab: A software-defined-radio ofdm modem example," in *2003 IEEE International Conference on Acoustics, Speech, and Signal Processing, 2003. Proceedings. (ICASSP '03).*, vol. 3, 2003, pp. III–761.

[111] S. Banou, M. Swaminathan, G. R. Muns, D. Duong, F. Kulsoom, P. Savazzi, A. Vizziello, and K. R. Chowdhury, "Beamforming galvanic coupling signals for iomt implant-to-relay communication," *IEEE Sensors Journal*, pp. 1–1, 2019.

[112] W. J. Tomlinson, S. Banou, C. Yu, M. Stojanovic, and K. R. Chowdhury, "Comprehensive survey of galvanic coupling and alternative intra-body communication technologies," *IEEE Communications Surveys Tutorials*, vol. 21, no. 2, pp. 1145–1164, 2019.

[113] M. Li, Y. Song, W. Li, G. Wang, T. Bu, Y. Zhao, and Q. Hao, "The modeling and simulation of the galvanic coupling intra-body communication via handshake channel," *Sensors*, vol. 17, no. 4, 2017.

[114] M. S. Wegmueller, A. Kuhn, J. Froehlich, M. Oberle, N. Felber, N. Kuster, and W. Fichtner, "An attempt to model the human body as a communication channel," *IEEE Transactions on Biomedical Engineering*, vol. 54, no. 10, pp. 1851–1857, 2007.

[115] Y. Song, K. Zhang, Q. Hao, L. Hu, J. Wang, and F. Shang, "A finite-element simulation of galvanic coupling intra-body communication based on the whole human body," *Sensors*, vol. 12, no. 10, pp. 13 567–13 582, 2012.

[116] S. H. Pun, Y. M. Gao, P. Mak, M. I. Vai, and M. Du, "Quasi-static modeling of human limb for intra-body communications with experiments," *IEEE Transactions on Information Technology in Biomedicine*, vol. 15, no. 6, pp. 870–876, 2011.

[117] X. M. Chen, P. U. Mak, S. H. Pun, Y. M. Gao, M. I. Vai, and M. Du, "Signal transmission through human muscle for implantable medical devices using galvanic intra-body communication technique," in *2012 Annual International Conference of the IEEE Engineering in Medicine and Biology Society*, 2012, pp. 1651–1654.

[118] N. Cho, J. Bae, and H. Yoo, "A 10.8 mw body channel communication/mics dual-band transceiver for a unified body sensor network controller," *IEEE Journal of Solid-State Circuits*, vol. 44, no. 12, pp. 3459–3468, 2009.

[119] M. A. Callejón, J. Reina-Tosina, D. Naranjo-Hernández, and L. M. Roa, "Measurement issues in galvanic intrabody communication: Influence of experimen-

tal setup," *IEEE Transactions on Biomedical Engineering*, vol. 62, no. 11, pp. 2724–2732, 2015.

[120] X. Ge, H. Cheng, M. Guizani, and T. Han, "5g wireless backhaul networks: Challenges and research advances," *IEEE Network*, vol. 28, no. 6, pp. 6–11, 2014.

[121] P. Noel and M. Klemes, "Doubling the through-put of a digital microwave radio system by the implementation of a cross-polarization interference cancellation algorithm," in *2012 IEEE Radio and Wireless Symposium*, 2012, pp. 363–366.

[122] L. Rossi, N. Calia, M. Nava, C. Salvaneschi, P. Agabio, B. Cornaglia, and A. Ratia, "2xstm-1 frequency reuse system with xpic," in *8th Eur. Conf. Fixed Wireless Netw. Technol. (ECRR'07)*, 2007, pp. 3–5.

[123] P. Noel, M. Prokoptsov, M. Klemes, H. Tai, A. Dufour, and K. Morris, "The design, development and implementation of a cross-polarization interference cancellation system for point-to-point digital microwave radio systems," in *2011 24th Canadian Conference on Electrical and Computer Engineering(CCECE)*, 2011, pp. 001 365–001 369.

[124] H. Proença and N. B. Carvalho, "Cross-polarization interference cancelation (xpic) performance in presence of non-linear effects," in *2010 Workshop on Integrated Nonlinear Microwave and Millimeter-Wave Circuits*, 2010, pp. 93–96.

[125] A. Câmpeanu and J. Gál, "Kalman filter carrier synchronization algorithm," in *2012 10th International Symposium on Electronics and Telecommunications*, 2012, pp. 203–208.

[126] W. T. Lin and D. C. Chang, "Adaptive carrier synchronization using decision-aided kalman filtering algorithms," *IEEE Transactions on Consumer Electronics*, vol. 53, no. 4, pp. 1260–1267, 2007.

[127] A. Vizziello, P. Savazzi, and R. Borra, "Joint phase recovery for xpic system exploiting adaptive kalman filtering," *IEEE Communications Letters*, vol. 20, no. 5, pp. 922–925, 2016.

[128] A. Patapoutian, "On phase-locked loops and kalman filters," *IEEE Transactions on Communications*, vol. 47, no. 5, pp. 670–672, 1999.

[129] E. A. Wan and R. V. D. Merwe, "The unscented kalman filter for nonlinear estimation," in *Proceedings of the IEEE 2000 Adaptive Systems for Signal Processing, Communications, and Control Symposium (Cat. No.00EX373)*, 2000, pp. 153–158.